Investigation of the detection process in nanowire superconducting single photon detectors

Investigation of the detection process in nanowire superconducting single photon detectors

PROEFSCHRIFT

ter verkrijging van de graad van doctor aan de Technische Universiteit Eindhoven, op gezag van de rector magnificus, prof.dr.ir. F.P.T. Baaijens, voor een commissie aangewezen door het College voor Promoties, in het openbaar te verdedigen op woensdag 2 december 2015 om 16.00 uur

door

Rosalinda Gaudio

geboren te Telese Terme, Italië

Dit proefschrift is goedgekeurd door de promotoren en de samenstelling van de promotiecommissie is als volgt:

voorzitter:	prof.dr. H.J.H. Clercx
1e promotor:	prof.dr. A. Fiore
copromotor:	dr. M.J.A. de Dood (Leiden University)
leden:	prof.dr. R.H. Hadfield (University of Glasgow)
	dr. H. Zbinden (Université de Gèneve)
	dr. R.W. van der Heijden
	prof.dr. K.A.H. van Leeuwen

Het onderzoek of ontwerp dat in dit proefschrift wordt beschreven is uitgevoerd in overeenstemming met de TU/e Gedragscode Wetenschapsbeoefening.

To my grandmother Addolorata

Table of contents

Table of contents

Abstract

This research work aimed at investigating the properties of superconducting single photon detectors (SSPDs) based on superconducting nanowires, a key technology for single-photon measurements and applications in the near-infrared. An SSPD typically consists of a long ($\sim$100μm) and narrow (100nm) wire patterned in a meander shape from a thin (5nm) superconducting film most commonly made of NbN, NbTiN or TaN. If the detector is kept below its critical temperature and is biased with a bias current slightly lower than the critical current it can detect the absorption of one or more photons. Despite the important technological progress achieved in the last decade, the microscopic working mechanism of the SSPD is still unclear and the fabrication yield is low.

During this PhD project these open issues have been addressed with the introduction of a simple detector, a short wire SSPD. Opposite to the meander SSPD, this short wire has a well defined active area and its multiphoton response is much more evident. This last property revealed to be crucial for the understanding of the detection mechanism in SSPDs.

The physical origin of the low yield has been addressed with the fabrication and characterization of NbN short wires with lengths ranging from 100nm to 15μm. The fabrication was carried out in our Nanolab@TU/e cleanroom facility and involved the use of techniques such as thin film sputtering deposition, optical lithography, electron beam lithography and reactive ion etching. Each fabrication step has been monitored with ellipsometric spectroscopy, atomic force microscopy and scanning electron microscopy. The electrical and optical characterization of such devices at low temperatures ($\sim$4K) showed that the NbN superconducting film is strongly inhomogeneous and the typical length scale of the inhomogeneity is $\leq$100nm.

These experimental results are endorsed by a simple microscopic model which considers the wire as made of short sections and associates to each section a critical current value according to a Gaussian probability distribution. In addition, the fabrication and characterization of similar SSPDs obtained from a commercial superconducting films deposited on a different substrate proved that the inhomogeneity is not typical of our NbN films only.

The NbN short-wire detectors were also used to improve the understanding of the detection mechanism in SSPDs. In collaboration with the Quantum Optics group in Leiden University, quantum detector tomography (QDT) experiments were carried out that allowed us to quantitatively characterize the multiphoton response of the detector. For each energy impinging on the detector, the probability that the detection is triggered by one, two or more photons was measured. In this way we could relate the impinging energy with the bias current needed to obtain a detection event with a given probability. Since the relation between these two quantities depends on the dominant detection mechanism, the experimental results allowed us to establish that the diffusion of the quasi-particles created by photon absorption plays a key role in the detection process.

Studying the short-wires SSPDs by means of QDT also allowed us to disclose another important aspect of the detection: the dimension of the area where superconductivity is perturbed after the photon absorption. The systematic study of the multiphoton detection in NbN nanowires of different lengths, revealed that the minimum distance between the absorption spots of two photons for which they can contribute to a two-photon detection process is ~20nm which provides a length scale for the dimension of the photocreated quasi-particle cloud.

The expertise acquired was then employed to address a new key question for the SSPD community, namely the physical origin of the different characteristics of SSPDs fabricated from NbN and WSi films. We investigated the detection mechanisms in short WSi wires by means of QDT. The fabrication process was modified and optimized to pattern a 250nm wide and 250nm long nanowire from the WSi thin film. The detector was characterized at 1.6K and its response to 11 different incoming wavelengths was analysed with the QDT technique. The experimental results reveal that, for the inspected energy range, the WSi detector behaviour follows that of NbN SSPDs.

Chapter 1

Introduction

1.1 Single photon detectors

The opportunity of realizing quantum information (QI) applications [1–4] is driving the interest for single photon detectors (SPDs). Quantum information science aims at manipulating, communicating and measuring information encoded in quantum objects as, for example, a single photon. For this aim, the development of detectors capable of detecting a single photon becomes crucial. After the proposal of a cryptography method based on quantum bits [5], the interest in this science and in applications such as quantum key distribution (QKD) [6] started growing. An indication of the interest triggered by QI can be found in the exponentially increasing number of peer-reviewed scientific papers published in the last thirty years [2]. Although the realization of QKD is probably the major driver for SPD research, several other important applications can be enabled by the development of sensitive, reliable and fast single photon detectors. Among those it is worth mentioning the characterization of quantum emitters [7], deep space optical communication (DSOC) [8, 9], light detection and ranging (LIDAR) [10] and integrated circuit testing [11].

The main figures of merit characterizing an SPD are the spectral range, the dead time, the dark count rate, the system detection efficiency, the timing jitter and the photon number resolution capability.

- The spectral range is the interval of wavelengths to which the detector is sensitive.

- The dead time is the time interval that the detector needs to reset and be able to detect the next photon.

- A dark count is a detection event not triggered by the absorption of a photon in the wavelength range of interest. The dark count rate (DCR) is the number of such *false* detection events recorded in one second.

- The system detection efficiency (SDE) is the efficiency with which a photon triggers a detection event. The SDE is given by the ratio of counts caused by photon absorption and the number of photons sent toward the detector. The counts caused by photon absorption are calculated from the difference between the photon count rate (PCR), that is the rate of detection events recorded when light is impinging on the detector, and the DCR.

- The timing jitter is the variation in the time span between the photon absorption and the appearance of a voltage pulse at the output, which sets the timing resolution.

- The photon number resolution (PNR) capability is the ability of a detector to distinguish how many photons are simultaneously absorbed.

In the ideal case, a perfect single photon detector provides a unitary detection efficiency and a jitter, dead time and DCR that are equal to zero.

In the rest of the chapter we are going to examine four of the most important single photon detector types. We will then focus our attention on the superconducting single-photon detectors and their performance. Some of the device open issues will be considered and the theoretical models describing the detection mechanism will be presented.

1.1.1 Photomultiplier tube

The photomultiplier tube (PMT) was the first reported device able to detect single-photons [1, 2]. A PMT consist of a vacuum chamber containing an anode, several dynodes and a photocathode made of a low work function material (figure 1.1). When a photon strikes the photocathode it extracts an electron that is accelerated toward the first dynode and provokes emission of secondary electrons upon impact. The consecutive impact of the latter on other dynodes multiplies the number of electrons that will eventually fall on the anode. Due to the avalanche-like mechanism, the electron flow to the anode results in a measurable current. The choice for the photocathode material not only determines the spectral range to which the PMT is sensitive, but can also make the PMT sensitive to the photon number. Indeed, if the photocathode is chosen such that the energy carried by two photons is required to eject the primary photon, the PMT can be used as a two-photon detector. The detection efficiency of a typical PMT is $\sim 40\%$ at λ=500nm, but only $\sim 2\%$ at the wavelength interesting for telecommunication applications, λ=1550nm. Although these devices have many promising features, which are summarized in table 1.1, it is important to underline that PMTs rely on
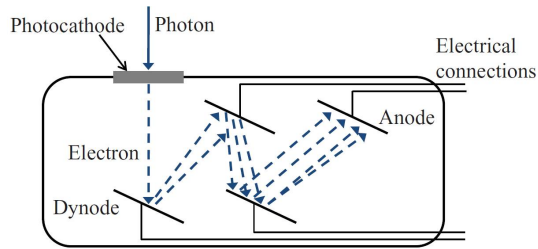
Figure 1.1 Schematics of a photomultiplier tube (from reference [2]).

the vacuum technology and, therefore, their scalability, reliability and lifetime is limited and the cost is relatively high.

1.1.2 Single-photon avalanche diode

The single-photon avalanche diode (SPAD) is an avalanche photodiode (APD) running in the so-called "Geiger" mode. In this mode, a reverse bias voltage larger than the breakdown voltage is applied to the diode. When a photon is absorbed, an electron-hole pair is created. The electric field is such to accelerate the electron and generate an avalanche of electrons through impact ionization with lattice atoms. In this condition, the flow of electrons results in a macroscopic and self-sustaining current that indicates the absorption of a single-photon.
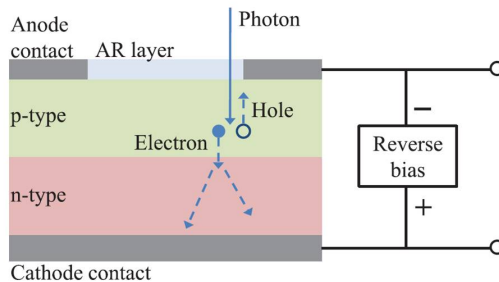
Figure 1.2 Schematics of a SPAD (from reference [2]). The p-n junction is biased with reverse voltage bias and, when a photon crosses the anti-reflection (AR) coating and is absorbed in the diode, the avalanche-like process starts.

In order to give the detector the possibility to reset, the external circuit is designed to quench the avalanche process. In the SPADs case, the choice of the semiconductor material

determines the spectral sensitivity. For example, since the InGaAs energy gap is of 0.75eV, InGaAs SPADs have a spectral cut-off for absorption at λ=1652nm. Compared to a PMT, an InGaAs SPAD provides higher DE at λ=1550nm and lower dark count rate (see table 1.1).

1.1.3   Transition edge sensor

A transition edge sensor (TES) consists of a thin superconducting film deposited on an insulating substrate. The substrate is kept at a base temperature T_b and is weakly linked to the superconducting film. The value of T_b is chosen in such a way to maintain the film at its transition between the superconducting and the normal state, where the film resistance strongly depends on temperature. In this condition, the absorption of a photon causes a small variation in the film temperature which corresponds in a measurable change of film resistance.
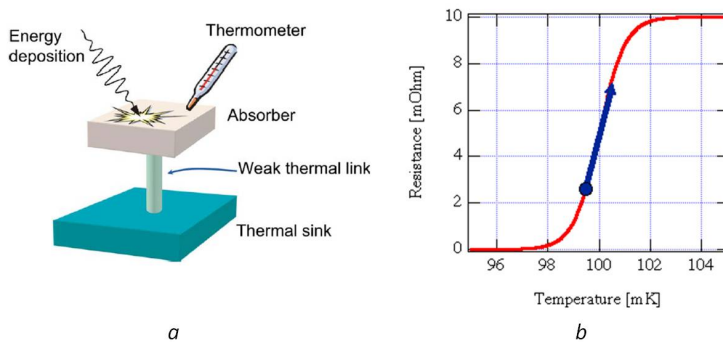
Figure 1.3 Panel *a*: schematic of a TES (from reference [12]). The absorber, a thin superconducting film, is connected via a weak link to the substrate that acts as a thermal sink. The absorption of a photon causes a temperature change that can be measured via the film resistance variation as shown in panel *b* (from reference [13]).

While the weak thermal link prevents the electrons to quickly cool down via the substrate, a negative electro-thermal feedback allows the device to reset for a new photo-detection. The TES has photon number resolving capabilities due to its working principle. Indeed, the absorption of more than one photon results in a consistently higher change in film resistance. The spectral sensitivity can be tuned with the choice of the anti-reflection coating deposited on the thin film or with the use of a cavity designed for certain wavelengths.
Despite the high sensitivity, the PNR capabilities and the low dark count rate, the TES is

characterized by long dead time and large jitter with respect to the SPAD and PMT (see table 1.1). In addition the operational temperature should be as low as 100mK.

1.1.4 Superconducting single-photon detector

The superconducting single-photon detector (SSPD) [1–3, 14] consists of a narrow (w=30-100nm) wire patterned from a thin ($\sim$5nm) superconducting film. When such a wire is kept well below its critical temperature T_c and biased just below its critical current I_c the absorption of a photon can be registered. Indeed, in a very schematic picture, if a photon is absorbed (figure 1.4, panel a), the energy transferred to the wire introduces a perturbation in the supercurrent flow that can lead to the transition from superconducting (SC) to normal (N) state. A normal section with resistance R_n appears which results in a voltage drop ΔV across the wire (figure 1.4, panel b).
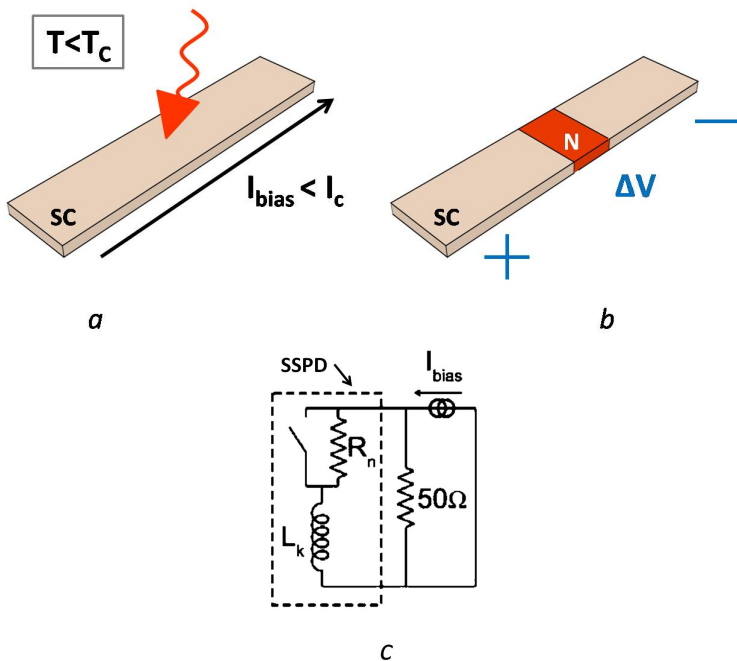
Figure 1.4 Sketch of a SSPD section. The wire patterned from a thin superconducting film (beige stripe) is kept at $T < T_c$ and biased with I_b slightly lower than its I_c. Panel a: a photon is absorbed and perturbs the superconducting state. Panel b: the perturbation can lead to the formation of a resistive barrier (red section) that causes a voltage drop ΔV across the wire. Panel c: schematics of an SSPD equivalent circuit taken from [15].

An SSPD and its readout circuit can be sketched as in panel c of figure 1.4 [15]. The SSPD is considered as a switch in parallel with a high resistor (R_n) and connected in series to a kinetic inductance L_k (dashed rectangle in panel c). When the SSPD is in the superconducting state, the switch is closed and the supercurrent flows through it without encountering any resistance. As soon as the transition to the normal state takes place, the switch opens and the current, which keeps on flowing through the device, encounters the resistance R_n. Due to Joule heating, the dimension of the normal section tends to increase. This process is counteracted by the electrothermal feedback [16]. Since R_n is much higher than the load resistance (50Ω), the current will be diverted toward the branch parallel to the SSPD giving rise to a measurable voltage pulse. In this way, the current through the SSPD decreases with a time constant $\tau_{fall} = L_k/[50\Omega + R_n]$ so that the device can cool down and recover for the next detection event. Once the SSPD is again superconducting, the current will recover with a time constant $\tau_e = L_k/50\Omega$. This previous model shows that maximum number of counts per time unit is limited by the time constant τ_e and therefore by the kinetic inductance [15, 16]. The reduction of L_k can improve the maximum count rate but has a drawback. Indeed, if the L_k is too small, the current in the SSPD will recover well before the device can cool down completely. In this case, where the electrical recovery is faster than the thermal one, the device latches or, in other words, its resistive section cannot leave the normal state. The main difference with a TES is that the photon energy is employed to heat the electron system of the SSPD, rather than the phonon one, which enables a faster response. The SSPDs offer single-photon sensitivity from visible to mid-infrared wavelengths, low dark counts, low jitter and short dead time (see table 1.1) and they can be designed to be photon number resolving [17]. Due to their favorable performance, the SSPDs constitute a promising technology for applications in quantum communication information. We focus on SSPD devices in this thesis.

SPD	T(K)	Spectral sensitivity	Max. efficiency (%)	DCR (Hz)	FWHM jitter (ns)	Max. CR (MHz)	Active area
PMT [18]	200-300	VIS-NIR	40@500nm 2@1550nm	100-2×10^5	0.3	10	$\sim 10^3$mm^2
Si-SPAD [19]	300	VIS	50@550nm	1	<0.05	12	$\sim$500µm^2
InGaAs-SPAD[20]	233	near-IR	12-15 @1550nm	10-40	<0.1	130 [*]	$\sim$500µm^2
TES [21]	0.1	IR	90 @1556nm	1	100	0.1	625µm^2
SSPDs[22]	<2	VIS-midIR	93 @1550nm	<10	0.1	25	$\sim$200µm^2

Table 1.1 The main features of the most representative SPDs are listed. [*] The InGaAs-SPADs can reach 1.5GHz count rate if sinusoidally-gated [23]. However, this configuration is not suitable for all applications.

1.2   SSPD: challenges and achieved performance

Since the first demonstration of a NbN based SSPD in 2001 [14] the SSPD field developed
and matured. In a period of almost 15 years numerous issues have been addressed and solved
and the understanding of the SSPD has been improved to the point that SSPDs are now a
commercially available product.

In this section we are going to examine a selection of challenges and issues related to the
SSPD performance. Although some of these obstacles have been understood and overcome
through technological developments, some others still remain obscure and constitute a
challenge.

1.2.1   Improving the system detection efficiency

The SSPD system detection efficiency (SDE) depends on the coupling efficiency ($\eta_{coupling}$),
the absorption efficiency (η_{ABS}) and the internal efficiency ($\eta_{internal}$). The $\eta_{coupling}$ indicates
how good the coupling between the detector and the incoming light is. The η_{ABS} denotes the
efficiency with which an impinging photon is actually absorbed in the detector. Finally the
$\eta_{internal}$ addresses the efficiency with which an absorbed photon results in a detection event.
Since the SDE depends on these three efficiencies, it can be expressed as

$$SDE = \eta_{coupling} \times DDE = \eta_{coupling} \times \eta_{ABS} \times \eta_{internal} \qquad (1.1)$$

where the DDE is the device detection efficiency, the efficiency with which a photon imping-
ing on the device triggers a detection which is equal to the product of η_{ABS} and $\eta_{internal}$. The
expression 1.1 underlines that the highest SDE can be achieved only if these three efficiencies
are maximized simultaneously.

In order to improve the system detection efficiency, one of the first obstacles to overcome
is coupling a beam spot onto a 100nm wide nanowire efficiently. For this reason, right
after the demonstration of a micro-bridge NbN SSPD [14] the detector was patterned in a
meandering shape in order to improve the $\eta_{coupling}$. These meander SSPDs are designed to
cover an area as large as 10μm×10μm [24, 25] or 20μm×20μm [26]. In addition, as reported
in [4, 22], the coupling efficiency can be further improved with an assembly that provides
optical self-alignment between a fibre and a meander SSPD with a precision of ∼3μm.

The enhancement of the photon absorption efficiency can be achieved with the integration
of the SSPD in an optical cavity [3, 27]. To date, this solution offers a NbN based SSPD
with the highest device detection efficiency (57% at λ=1550nm) and a WSi based SSPD
with DDE close to unity [22]. Among the numerous techniques developed to improve the

η_{ABS} [3, 4], it is worth mentioning the integration of the detector with a wavelength specific distributed Bragg mirror [28], an optical waveguide [29] and a photonic crystal [30].

The $\eta_{internal}$ of an SSPD depends on several factors. Among those, the wire width, the film thickness, the wavelength of the impinging photons and the choice of superconducting thin film were shown to be relevant. The $\eta_{internal}$ can be improved with wires of width $\sim$30nm [31], by using shorter wavelength photons or by reducing the superconducting film thickness [32]. The reduction of wire width, as well as the reduction of film thickness, decreases the wire volume where the energy of the absorbed photon is deposited. Therefore, given a fixed photon wavelength, the narrower (or thinner) wire will be more responsive than a wider (or thicker) wire because the perturbation of superconductivity that follows a photon absorption has more probability of resulting in a detection event. For the same reason and for a fixed wire dimension, $\eta_{internal}$ can be increased by employing photons of shorter wavelengths since, a higher energy will be deposited in the same wire volume.

Material	NbN	TaN	WSi
Δ (meV)	2.3	1.3	0.53

Table 1.2 Experimental values of the superconducting gap for NbN, TaN and WSi thin films from reference [33].

Despite the technological efforts focused on improving the $\eta_{internal}$ of SSPDs based on nitrides superconducting films like NbN, TaN, NbTiN, so far no experimental work has ever reported an internal efficiency close to unity. In addition, for such materials the SDE appears to reach its highest value only when the bias current approaches I_c [26, 27] and, since the $\eta_{coupling}$ as well as the η_{ABS} do not depend on I_b, this effect should be attributed to $\eta_{internal}$. Recently the exploration of new superconducting materials with lower superconducting gap (Δ) revealed that there is still room for $\eta_{internal}$ improvement. In 2011 [34] the use of amorphous WSi [35] superconducting thin film for SSPD fabrication showed an internal efficiency close to unity and in 2013 an SDE of 93% was reached by improving the coupling with light and the absorption efficiency [22]. Since then, despite the low temperatures required to operate these devices [22, 36], several other amorphous materials like MoGe [37] and MoSi [38] have been considered and, together with WSi, they constitute a very promising option for realization of efficient SSPDs. The higher internal efficiency provided by SSPDs patterned from those amorphous superconductors can be related to their low superconducting gap. Indeed, if we compare NbN based and WSi based SSPDs that have equal dimensions and are illuminated by photons of the same wavelength, we could expect that the photon

absorption would cause a more severe perturbation of the superconducting state in the latter device, because of the lower gap. Therefore, a detection event in WSi based SSPDs would be triggered with higher probability than in the NbN case. However, to date not much is known about the exact detection process in SSPD patterned from amorphous materials [33, 39].

1.2.2 The dark counts issue

The dark count rate (DCR) of an SSPD is crucial for the device performance because it increases exponentially as I_b approaches I_c [40]. A dark count can be distinguished into intrinsic and extrinsic. The extrinsic DCR is caused by the absorption of infrared photons and those can be reduced by introducing cold filters. The cause for the intrinsic DCR is, instead, still object of debate.

Since the superconducting films involved in the fabrication of SSPDs are typically type-II superconductors, it is reasonable to suppose that the origin of the dark count pertains to vortices. A vortex in a current carrying superconducting nanowire would be dragged across the width of the wire under the influence of the Lorentz force and, thus, it would dissipate energy raising the probability for a random detection event. The vortex entrance in the nanowire could be caused by the unbinding of vortex-antivortex pairs (VAPs) [40] or by the lowering of the barrier potential for vortex entry [41]. Even though recent theoretical calculation [42] revealed that the second mechanism is the most favourable and it takes place already for $I_b \sim I_c/3$, so far no experimental evidence could distinguish between the two scenarios [43].

However, a reduction of DCR was achieved also through several theoretical and technological improvements. For example, a deeper understanding of the current crowding [44] combined with the employment of new optimized designs which minimize the current crowding [45, 46] revealed that the choice of detector geometry influences the dark count rate. In addition, also a better system design can lead to a reduced DCR as reported in [47]. In this work, the authors obtained a DCR reduction of almost three orders of magnitude by introducing a cold bandpass filter which allowed only the interesting wavelength to reach the detector. Finally, also tuning the thin film deposition parameters showed to play a role in the decrease of DCR [48].

1.2.3 The SSPD fabrication yield

The fabrication yield of NbN based SSPDs is low since nominally identical devices present different I_c values and offer different detection efficiencies [27]. This effects constitute an obstacle not only for the realization of efficient detectors, but also for the development of

detector arrays. Indeed, in the latter case the fabrication of several SSPDs that provide the same electrical and optical response is a crucial requirement.

It has been reported that the increase in meander active area, which is usually pursued to improve the coupling efficiency, leads to suppression of critical current [49]. Such reduction in I_c has been attributed to the presence of isolated point-like defects with reduced critical current, named constrictions [50]. In the case in which the SSPD presents a constriction, its final I_c will be limited to the I_c value of the constriction. In addition, only that point-like defect will respond to incoming light efficiently since it will be the only one in the wire to be biased close to the wire I_c. Such constriction presenting an higher efficiency has been *observed* in a device with very low DDE through device mapping [51]. However, so far no experimental evidence provided clear information on the density of such defects in high DDE SSPDs and their physical origin is still object of debate.

It is important to underline that the SSPDs patterned from amorphous superconducting films are more robust to constrictions and patterning defects due to their saturated detection efficiency [34]. Therefore, a higher fabrication yield can be achieved and the realization large SSPD arrays of good quality appears feasible with amorphous superconducting film [52].

1.3 SSPD detection mechanism

The demonstration of single-photon detection with superconducting nanowires [14] triggered not only technological interest but also curiosity for the unknown microscopic mechanisms leading to a detection event. Since 2001, several scenarios have been proposed and their predictions have been experimentally tested. Despite the theoretical effort, the mechanism governing the detection process in SSPDs is still subject of debate.

The following paragraphs present the main models which describe the detection phase taking place between the photon absorption and the formation of a resistive belt across the entire width of the wire (the subsequent electro-thermal dynamics is well understood [15, 16]). As we will see, the proposed scenarios mainly differ for the relation between the energy of the impinging photon (E_φ) and the bias current required to trigger a detection event (I_b^{th}) [53]. In all models, the absorption of a photon carrying the energy E_φ results in the breaking of a Cooper pair and the consequent promotion in energy of an electron. The excited electron will thermalize through generation of a large number of excited quasi-particles.

1.3.1 Normal-core hot spot model

The first proposed scenario is the normal-core hot spot model [53, 54]. According to this model, when the density of quasi-particles is high enough, a normally conducting disc, or

hot spot, appears in the current-carrying superconducting nanowire (see panel a in figure 1.5). The supercurrent is then diverted toward the sidewalks where the bias current density j_b can reach the critical value j_c. If the condition $j_b \geq j_c$ is satisfied, also the sidewalks will experience the transition from superconducting to normal state. At this point a resistive barrier appears across the entire width of the nanowire which then quickly expands due to Joule heating. According to the previous scenario, for given wire width w and bias current I_b^{th}, the occurrence of the resistive barrier depends on the diameter D of the hot spot. Indeed, the formation of a bigger hot spot increases the chance for j_b^{th} to reach j_c, since the same supercurrent is forced to flow through narrower sidewalks with total width (w-D). Recalling that the area of the hot spot is directly proportional to E_φ and, thus D $\propto \sqrt{E_\varphi}$, we can write the relation between E_φ and the I_b^{th} needed to trigger a detection event as

$$I_b^{th} = I_c \left(1 - \kappa \sqrt{E_\varphi}\right) \tag{1.2}$$

where I_c is the measured critical current and κ is a factor that depends on the material and the device [53]. A direct consequence of this first model is that the detection will not take place if, for a fixed I_b, the hot spot dimension is too small. In other words, the detection efficiency is expected to decrease sharply for impinging photons of longer wavelengths. However, such spectral cut-off in the detection efficiency has not been observed, but rather a slow decrease is reported in several experimental results [53, 55]. In addition, if the same geometrical argument considered in the model is used to predict the hot spot dimension from the experimental data, an area smaller or comparable to the superconductor coherence length ξ is found [55] ($\xi \sim 4$nm in NbN [33]). This implies that the hot spot, whose dimension is similar to ξ, does not constitute an obstacle for the supercurrent.

1.3.2 Diffusion-based hot spot model

The discrepancies between experimental results and the normal-core hot spot model encouraged the formulation of a refined model: the diffusion-based hot spot model [55]. The fundamental novelty introduced by this model regards the requirement for a transition to the normal state. Indeed, according to the diffusion-based model the appearance of a detection event does not require the formation of any resistive hot spot. The refined model focuses on the number of Cooper pairs present in a wire section of length equal to ξ, the ξ-slab. After the photon absorption, the quasi-particles, instead of remaining concentrated in a small area, as assumed by the normal-core hot spot model, diffuse over a length comparable to the wire width. The number of Cooper pairs in the ξ-slab is decreased, therefore the superconductivity is weakened but not destroyed. Since the ξ-slab is still superconducting, the remaining

Cooper pairs will accelerate in order to carry the same supercurrent that the nanowire was carrying before the absorption (see panel *b* in figure 1.5). When the superconducting carriers reach the critical velocity, the wire section experiences the transition to the normal state and gives rise to a voltage pulse in the read-out circuit.
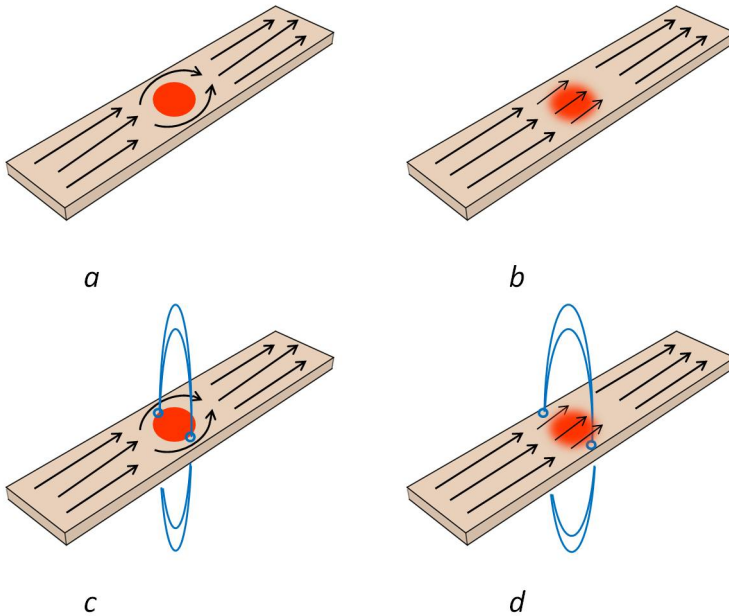
Figure 1.5 Panel *a*: Schematics of the normal-core hot spot model. The red disc in the current carrying superconducting nanowire represents the normal conductive disc formed after photon absorption. As indicated by the curved arrows, the supercurrent is diverted to the sidewalks. Panel *b*: Schematics of the diffusion-based hot spot model. The shaded red area represents the wire section with decreased number of Cooper pairs. The thin arrows indicate that even though in the shaded red area the superconductivity is weaker, the transition to the normal state did not take place yet. Panel *c* and *d*: The normal-core and the diffusion-based hot spot models respectively are modified to include the role of vortices. The two blue open circles represent a pair of vortex and anti-vortex that nucleate at the resistive hot spot (*c*) or at the edges of the wire where superconductivity is weakened (*d*).

In the refined model the chance for a detection event at a fixed bias current I_b depends on the number of Cooper pairs that are broken after the photon absorption. Since, the depletion of Cooper pair density is directly proportional to the energy E_φ of the impinging photon, the

relation between E_φ and I_b^{th} is linear and can be written in the form

$$I_b^{th} = I_c \left(1 - \frac{E_\varphi}{E_0} \right) \tag{1.3}$$

where E_0 is an energy scale that can be made explicit as shown in the references [53, 55].

The diffusion-based hot spot model, provides an improved expression for the cut-off wavelength ($\lambda_{cut-off}$) [53], i.e. the maximum wavelength for efficient detection. However, it still fails in describing the slow decrease of detection efficiency which is experimentally observed when photons of longer wavelengths impinge on the detector [53, 56].

1.3.3   The role of vortices in the detection mechanism

A possible cause of the slow roll-off for the detection efficiency observed for increasing wavelengths was first put forward by Semenov and coauthors in 2008 [56]. In their work, the authors explain the slow roll-off assuming that the detection events is vortex-assisted. When a photon with wavelength beyond $\lambda_{cut-off}$ is absorbed, the perturbation of the superconducting state is not enough to trigger a detection event but can enhance the probability for thermal activation of a vortex-antivortex pair (VAP) unbinding. Then, under the effect of the Lorentz force, the vortex and antivortex are dragged toward opposite wire edges. During their motion, the vortex and antivortex dissipate energy giving rise to a detection event [53, 56].

The VAP unbinding is not the only mechanism proposed to explain the slow roll-off in the detection efficiency. More recent theoretical studies put forward the possibility that the vortices can hop from one site to the other [32] or that vortices can enter the superconducting wire if the potential barrier for vortex entry is lowered [41]. According to recent calculations [42], the second scenario appears to be the most favourable one with respect to the VAP unbinding and the vortex hopping.

It is important to mention that, according to these latest works [41, 42], the vortex entry takes place also at bias currents close to I_c. More precisely, from the calculations the potential barrier for vortex entry appears to be completely suppressed for an $I_b \sim 80\%$ of the I_c. This theoretical result would explain the reason why the measured I_c is always lower than the theoretical value (the depairing current I_c^{dep}) even in short wires patterned from high quality superconducting films.

The important role of vortices has been taken in account in recently formulated models where the effect of vortices is integrated with the normal-core hot spot model (figure 1.5 panel c) and the diffusion-based hot spot model (figure 1.5 panel d) [33, 39].

Despite this relatively large body of theoretical and experimental work, at the beginning of this thesis no clear consensus had been reached on the detection mechanism and particularly on the role of quasi-particle diffusion and vortices. This was largely due to the fact that accessing a wide range of optical energies to explore the energy-current relation is experimentally very challenging. Additionally, the large meanders typically employed in previous investigations are prone to inhomogeneities and present characteristics which vary widely from device to device.

1.4   Scope of the thesis

In this thesis, two outstanding open issues in the field of SSPDs are addressed: the origin of inhomogeneous critical current in NbN nanowires and the microscopic detection process which leads to a detection event. Our approach is based on two key choices: 1) the use of very short wires (or nanodetectors) which provide straightforward information on the device and the use of modified quantum detector tomography to access a wide range of optical energies.

The nanofabrication process followed to realize the nanodetectors is reported in Chapter 2 together with the experimental methods implemented to investigate the devices performance. Chapter 3 describes the systematic study carried out on a series of short NbN wires to investigate the cause of the low fabrication yield in NbN based SSPDs. The experimental results reported in this chapter reveal the inhomogeneous nature of the NbN SSPDs at the nanoscale.

Chapter 4 introduces the modified quantum detector tomography protocol and reports the main results obtained by applying such protocol to NbN bow-tie and short wire detector. The investigation reveals the dominant detection mechanism in NbN SSPDs and provides an estimation of the hot spot dimension.

In Chapter 5 the detection mechanism of WSi based SSPDs is investigated by means of quantum detector tomography. The experimental results reveal that the detection mechanism, in the examined energy range, is similar to that of NbN based detectors.

Finally, Chapter 6 summarizes the main results and concludes the thesis.

Chapter 2

Experimental methods

In this chapter I will describe the fabrication process implemented for the device realization and the experimental set-ups used for tests and experiments.

2.1 Fabrication process

The fabrication flow, which I followed to realize NbN based nanodetectors, consists of five processing steps: the NbN film deposition, the optical lithography step, the metal evaporation for contact pads, the electron-beam lithography step and the NbN etching. The WSi based nanowires and those patterned from $NbN/SiO_2/Si$, that will be examined in chapter 5 and 3 respectively, were realized by following the same procedure except for the film deposition and the electron-beam lithography step. The changes that were introduced in the latter step are reported in the related paragraph. The fabrication steps described in those paragraphs are performed in the NanoLab@TU/e cleanroom facility with the only exception of WSi thin film deposition, which is performed in the National Institute of Standard and Technology (NIST, Boulder CO, USA) and the deposition of NbN on SiO_2/Si which is performed by SCONTEL (Moscow, Russia) [57].

2.1.1 NbN film deposition

In the first fabrication step, the NbN thin film is deposited on a GaAs(001) at $\sim400^oC$ through sputtering of a Nb target in N_2 and Ar atmosphere. The deposition takes place in the AJA Intern., INC., ATC 1500-F system. The AJA sputtering system is provided with a pair of halogen lamps, four chimneys containing Nb, Au, Ti and Cr targets and the supplies for

N_2 and Ar gasses [1].

Before each NbN deposition campaign, the sample holder and the sputtering chamber are conditioned to avoid particle desorption during the NbN deposition. The sample holder is cleaned, baked and a thin layer (50nm) of Ti is deposited on its surface. The chamber conditioning is performed to lower the base pressure until it drops below $7.5 \ 10^{-9}$ Torr. Such conditioning consists of an additional Ti or Ti/Au deposition.

The GaAs chips are produced by cleaving a GaAs wafer. The chips are cleaned with acetone and isopropanol in an ultrasonic bath and are mounted on the sample holder with melted Indium The main reason for the choice of In mounting is related to the geometry of the sputtering chamber. The halogen lamps, which are placed at the top of the chamber, heat up the back of the sample holder which is clamped immediately below. The GaAs chips are upside down on the front side of the holder and they face the chimneys which are located at the bottom of the chamber. In this configuration, the Indium mounting ensures a good and uniform thermal contact between the holder and the GaAs substrates. Moreover, during the
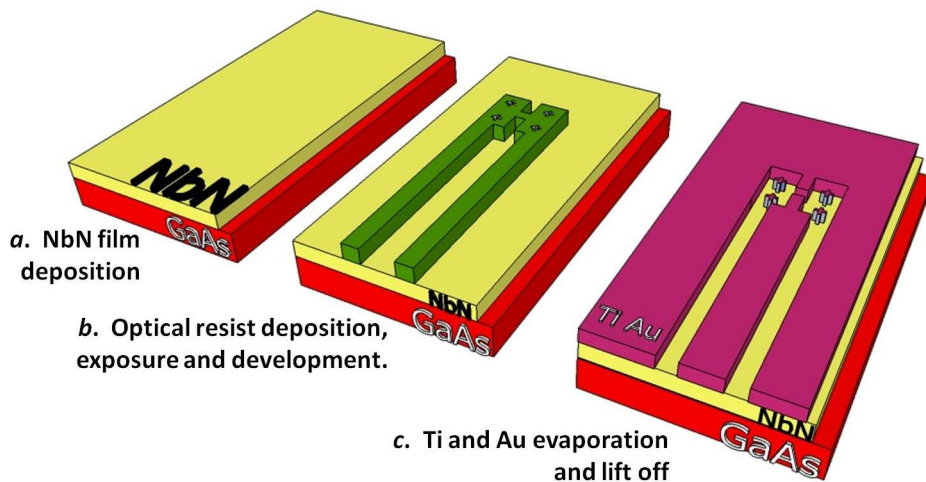
Figure 2.1 Sketch of the first three stages of the nanowire detector fabrication. The three panels show how the contact pads (pink layer) are defined on the NbN thin film (yellow layer). The layer thicknesses are not to scale.

deposition, when the base temperature is higher than the Indium melting point (156.6^oC),

---

[1]A more detailed description of the AJA sputtering system can be found in the PhD thesis of Dr. D. Sahin. "Waveguide Single-Photon and Photon Number-Resolving Detectors", Eindhoven University of Technology 2014.

the thin layer of liquid In ensures the adhesion of the GaAs chip to the holder due to surface tension.

The holder carrying the GaAs chips is then inserted in the sputtering machine via a loading chamber and is clamped, upside down, right below the halogen lamps. At this point the NbN deposition can take place. In order to ensure a uniform deposition, the holder is put in rotation and the distance between the holder and the chimneys as well as the inclination angle of the NbN target is set to an optimum value. The deposition process starts with raising the base deposition temperature T_{dep}. Once the desired value of T_{dep} is reached and it is stable, an optimum flow Φ of N_2 and Ar is let into the chamber, the Nb chimney is supplied with a fixed current I_{target} to create the necessary voltage between its bottom and top parts to ignite the plasma. The Ar plasma in the chimney sputters Nb atoms from the target, those react with the N_2 gas and land on the GaAs substrates where they contribute to form the NbN thin film.

The deposition of an optimal NbN thin film (figure 2.1, panel a) is performed with the following deposition parameters: $T_{dep} \sim 400^oC$, I_{target}=250mA, Φ_{N_2}=1.4sccm (standard cubic centimetre per minute), Φ_{Ar}=12sccm and the holder rotation is set to 50rpm (rotations per minute). Finally, according to the deposition conditions, a NbN film of thickness $\sim$5nm is obtained with a deposition time of $\sim$100s.

2.1.2 Optical lithography and metal evaporation

In the phase following the NbN film deposition (figure 2.1, panel a) the contact pads are defined by means of optical lithography and metal evaporation (figure 2.1, panels b and c). In order to define the contact pads, the negative resist MaN440 from Micro Resist Tech. is spun onto the NbN film for 30sec at 5000rpm with the Karl Süss RC8 spinner. After a baking of 5min at 95°C, the sample is ready to be exposed at the UV light with the Mask Aligner 6 (MA6) that performs optical lithography in proximity mode. The MA6 covers the sample with a pre-loaded optical mask which contains the design of the contact pads. To ensure that no particles are present between the mask and the sample and to avoid the degradation of the photoresist, the MA6 brings the mask close to the sample and separates them by vacuum. The sample is then exposed to the UV light for a time interval of 50-100 seconds depending on the UV lamp intensity. Following the exposure, the photoresist is developed with MaD332-s for 2minutes and 30 seconds (figure 2.1, panel b).After the photoresist development, the sample is introduced in the electron-beam evaporator FC2000 to deposit, first, 14nm of Ti and then 140nm of Au. The deposited metal covers the entire sample surface and fills in the empty areas between the photoresist structures. In the lift-off phase, when the sample is kept in acetone vapour for 1 hour and 30 minutes, the photoresist dissolves allowing the lifting off

of the metal. In order to ensure the complete removal of the metal in the areas outside the contact pads, the samples are kept in acetone, in the ultrasonic bath for 30 seconds, cleaned with isopropanol and blown-dry with N_2 flow.
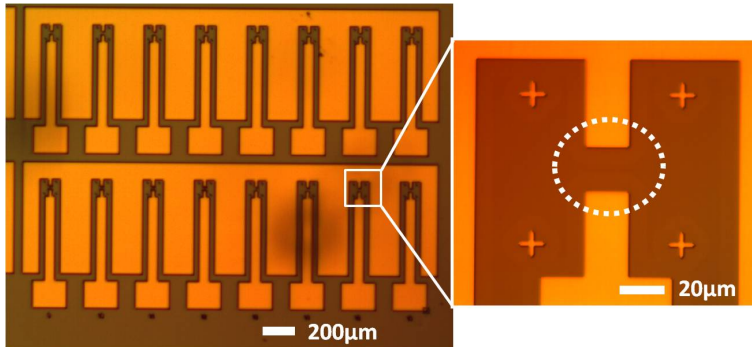
Figure 2.2 Optical microscope images of the sample after the lift-off step. The yellow structures are the gold contact pads which lay on the NbN film (grey background). *Inset*: Magnification of the writing field containing the area (dotted circle) where the nanowire detector will be exposed. The four crosses are aligning marks.

The metal that remains after this lift-off defines the contact pads (figure 2.1, panel *c*). The images in figure 2.2 are acquired from an optical microscope and show the sample with the contact pads right after the lift-off.

2.1.3   Electron-beam lithography and reactive-ion etching

The nanowire detectors are defined through electron-beam lithography (EBL) and reactive-ion etching. In the first part of this phase, the sample with contact pads is covered with a negative electron-beam resist, the HSQ (hydrogen silsesquioxane) XR-1541-6 from DOW CORNING. The sample is spun with the CONVAC ST 146 spinner for 1 minute at 2000rpm and is then baked for 2 minutes at 150^oC and 2 minutes at 220^oC (figure 2.3 panel d). The sample is now ready to be loaded into the EBL writer. But before that, a thin layer of Au ($\sim$7.5nm) is evaporated on the sample edge in order to avoid the resist charging during the EBL beam focusing. The gold layer deposition is performed with the Edwards Auto 306 evaporator.

Once the sample is loaded into the EBL writer Raith 150 II, the electron-beam focusing, the manual and automatic mark alignments are performed to align the design to be exposed with the existing contact pads. The four crosses, which are defined together with the contact pads and are shown in the inset of figure 2.2, determine the location where the nanowire should be written.
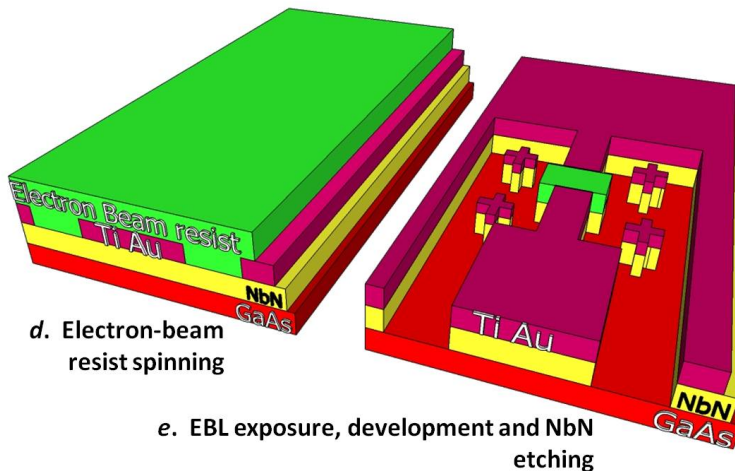
Figure 2.3 Sketch of the last two phases of the fabrication process: the EBL resist spinning (d) and the EBL exposure, development and etching (e). The nanodetector is located at the center of the square delimited by the four alignment marks. The layer thicknesses are not in scale.

The EBL design, which is drawn beforehand with the Raith software, is defined according to the desired geometry of the detectors, the thin superconducting film and the substrate

material. The detector design is not defined only by the nanowire geometry, but also by the additional inductance which is introduced to avoid detector latching [15, 58]. For the detectors examined in this thesis, such inductance is provided with the addition of an extra meander (panel *a* of figure 2.4). The sample material, instead, influences the electronic dose (C/cm^2) that the EBL should deposit in order to successfully expose the HSQ resist and, thus, correctly write the design. For example, the WSi devices examined in chapter 5 were obtained with a dose that was lower than that needed for the NbN detectors examined in chapters 3 and 4. The difference was unexpected and may be related to the higher density of WSi (9.3g/cm^3) with respect to that of NbN (8.4g/cm^3). Moreover, as shown in chapter 3, several detectors were patterned from NbN/SiO$_2$/Si to be compared with those patterned from NbN/GaAs. In this case, where the SiO$_2$/Si substrate has lower density (2.6g/cm^3) than GaAs (5.3g/cm^3), the dose was noticeably increased with respect to that used for the NbN/GaAs samples.
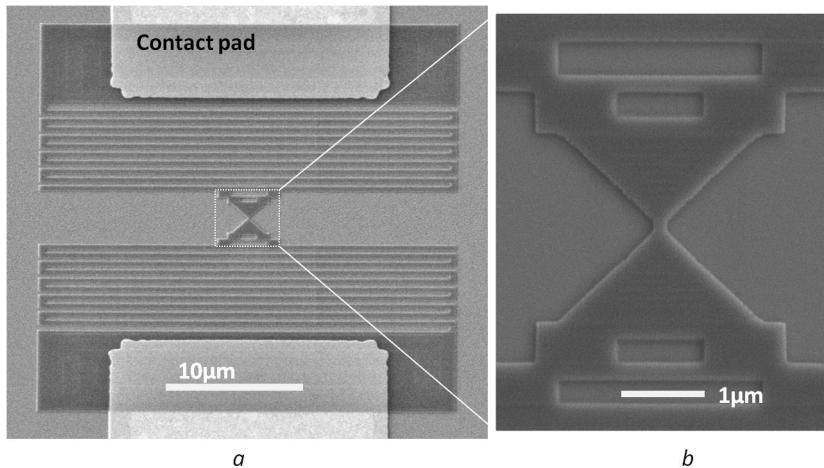
Figure 2.4 SEM micrographs of a nanodetector at the end of the fabrication process. Panel *a*: The detector active area, at the center of the image, is connected to the contact pads through the additional meanders which provide extra inductance. Panel *b*: Magnification of the active area, still at the center of the image, and the tapering.

Finally, the dose value is fine tuned via a dose test and with a correction for the proximity effect provided by the Raith software. Once the EBL exposure of the design is completed the sample is developed. In the case of the NbN thin film, the sample is developed for 1 minute and 15 seconds in a solution of ultra-pure water and the inorganic developer AZ 400 K (4:1). For the WSi film, instead, the development is performed with the developer

MaD 531-s at 60°C and lasts for 2 minutes.In the last fabrication step the NbN or WSi not covered by the exposed HSQ is etched down via reactive-ion etching. This step is performed in Ar/SF$_6$ plasma for 15 seconds (figure 2.3 panel *e*). The device, which is now ready for tests and experiments, appears as shown in figure 2.4. The nanoscopic active area of the nanodetector, which is shown in the center of figure 2.4 (panel *b*), is defined together with tapering structures to connect the active area with the extra meander while minimizing the current crowding effect [44].

2.2   Characterization techniques

The tests and experiments reported in this thesis were performed mainly with three experimental setups: a cryogenic dipstick, a micro-manipulated cryogenic probe station and a closed-cycle VeriCold cryocooler. The description of these setups together with the standard measurements performed through them are described in the following paragraphs.

2.2.1   NbN film characterization

The NbN film characterization consists of the measurement of the film thickness, the film roughness and the film critical temperature T_c. The film thickness is measured right after the NbN film deposition with a spectroscopic ellipsometer (SE) and the typical thickness achieved is ∼5nm. The film surface is inspected with an atomic force microscope (AFM) and an optimal roughness value is ∼0.3-0.4nm.

The critical temperature of the film is measured with a dipstick through a four point method. The dipstick consists of a long stick carrying the sample at one of its ends and allows to cool the NbN film down to 4.2K by inserting it directly into a LHe dewar. The dipstick head, which carries the sample, is sketched in figure 2.5. As shown in the top view of figure 2.5, the sample, which is mounted on the dipstick head with the VGE-7031 LakeShore varnish, is connected to four copper pads via four copper wires. The side view indicates that these copper wires are substituted by other wires along the length of the dipstick and until the room temperature connections (coaxial cables) are reached. At room temperature, the coaxial cables are connected to the Keithley 2010 multimeter and the Yokogawa 7651 current source. The side view of the dipstick head shows also that immediately under the sample a Si diode and a resistor are allocated. Both the Si diode (Lakeshore DT-670) and the heating resistor are connected to the LakeShore 330 temperature controller to monitor the sample temperature and maintain it stable during the measurement with a PID feedback system.

Once the NbN film is inside the dewar and it reaches a temperature lower than its T_c, a fixed current is supplied to it and a temperature scan starts. During this scan the temperature is increased by a desired fixed amount and, when it is stable at the given value, the voltage drop across the NbN film is recorded through two separate contacts. The film resistance is then calculated and plotted as a function of the film temperature. By the end of the temperature scan, a graph similar to that reported in figure 2.6 is obtained. From this graph and following the procedure reported in reference [59] we estimate the value of T_c and the width of the transition ΔT_c. Typical values for a NbN film of thickness ∼5nm deposited at a base temperature of 400^oC are $T_c \sim 10K$ and $\Delta T_c \sim 0.3K$.
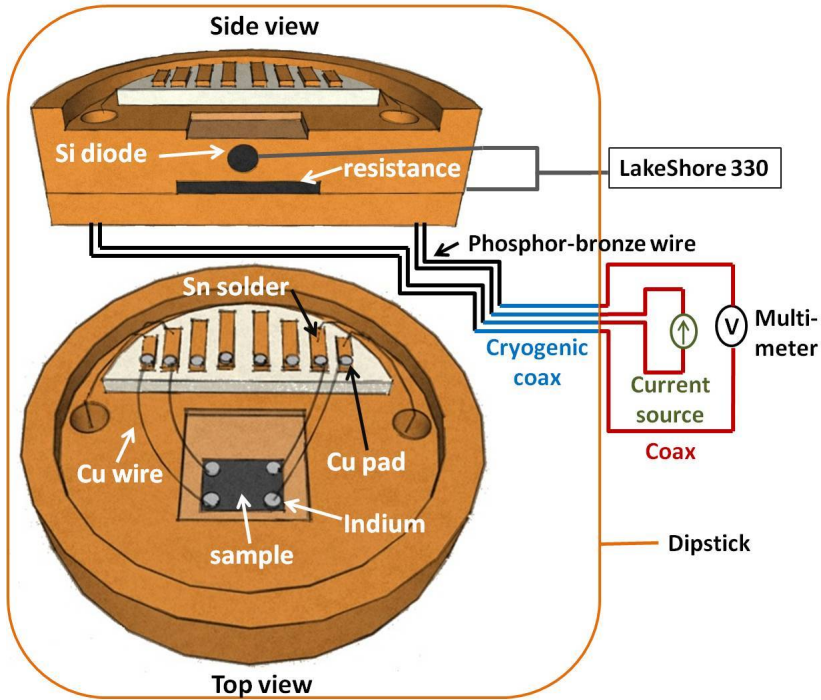
Figure 2.5 Schematics of the dipstick setup. The sample is connected to a multimeter and a current source through copper wires (black lines in the top view), phosphor-bronze wires (black lines in the side view), cryogenic coaxial cables (blue lines) and coaxial cables at room temperature (red lines). The sample is located on the holder and immediately above a Si diode and a sheet resistance (side view). Those are connected to a temperature controller.
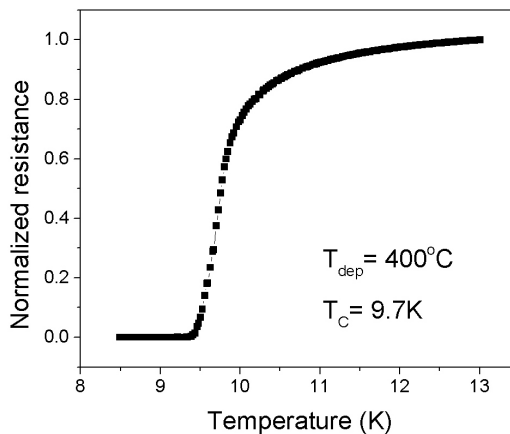
Figure 2.6 Typical R(T) curve obtained with the dipstick setup from a $\sim$5nm thick NbN film.

2.2.2   Micro-manipulated probe station

The micro-manipulated probe station consists mainly of a continuous flow cryostat that allows the characterization of a large number of devices in the same cooling run. Because of its convenience and stability, this setup was employed for the systematic study of nanowire SSPDs reported in chapter 3.

The cryostat consists of a vacuum chamber (see figure 2.7) with an optical window at 300K. Such vacuum chamber hosts an inner shield with a cold filter, a copper rod and a copper sample holder, heat exchangers and connections for the LHe flow. Before cooling down, the chamber is evacuated overnight with a turbomolecular pump until a pressure level of $\sim 10^{-5}$ mbar. Then, through the connection with a He pump, the liquid Helium is forced to flow from a LHe vessel, across the heat exchangers of the cryostat. The continuous flow allows the copper rod and the sample holder to cool down. A diode and a resistance are placed close to the sample holder in order to monitor the temperature and warm up the cryostat. In order to enhance the thermal contact, the sample is mounted on the sample holder with LakeShore VGE-7031 varnish. However, a good thermal contact is often difficult to achieve and for this reason special care should be taken during mounting. In addition, the thermal contact can be improved by the employment of copper clamps.

The electrical contact between the sample and the external circuit is performed through a 50Ω, 40GHz radio frequency (RF) micro probe in the ground-signal-ground (GSG) configuration. The probe is connected to the electrical circuit at room temperature via an SMA cable (see figure 2.7) and can be translated through a XYZ movable stage. In this way, the three fingers (GSG) of the probe can be placed in contact with the contact pads of the desired device.

The optical access is realized through the cryostat window. The input light (λ=1310nm) is coupled into free space and collimated by a lens. The parallel beam encounters an iris (1.5mm diameter) and a beam splitter (45% reflection, 55% transmission) and it is then directed toward a microscope objective (NA=0.03) which focuses the beam onto the sample. The choice of the iris was dictated by the need for a uniform device illumination. The presence of the iris, indeed, reduces the numerical aperture and increases the spot diameter on the sample to $\sim$20μm. Finally, the light reflected back from the sample, reaches the CCD camera placed above the beam splitter which, thus, provides the image of the sample in real time.
The position of the optical system can be adjusted to illuminate the specific device or to improve the focus via a Thorlabs motorized servo actuator.
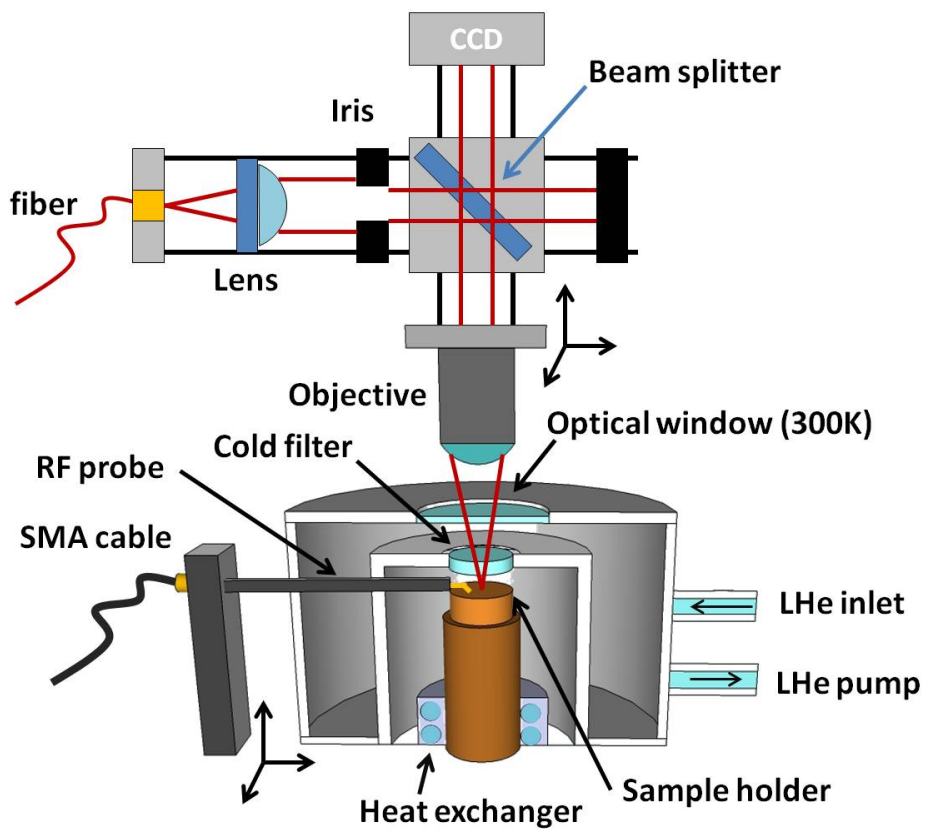
Figure 2.7 Schematics of the micro-manipulated probe station. At the bottom, the cryostat hosting the sample and the probe is sketched. The upper part of the image describes the optical path.

The electrical characterization of the nanowires consists of acquiring the current flowing through the device as a function of the voltage across it. Such a measurement is performed by connecting the circuit reported in figure 2.8 (panel a) to the probe and, thus, to the SSPD. The voltage source Yokogawa 7651 supplies the bias voltage V_b to the SSPD through a 10Ω resistor (R_b) and the DC port of a bias-T (Mini-Circuits ZBNT-60-1W). As shown in panel a of figure 2.8, the RF port of the bias-T is not used and terminated with a 50Ω-matched cap. During the acquisition, the voltage V_b is swept and, simultaneously, the voltage drop across the resistor R_b is measured by the multimeter Agilent 34970A. The current flowing through the SSPD is then calculated and plotted as a function of V_b. The typical IV curve is reported in panel b of figure 2.8. The IV curve reported in panel b of figure 2.8 was acquired at the nominal temperature of 4.2K from a NbN based nanowire SSPD 100nm wide and 100nm long. The IV curve in the graph reveals three main regions: the superconducting region (red oval), the relaxation-oscillation region (blue oval) and the ohmic region (green oval) [60].
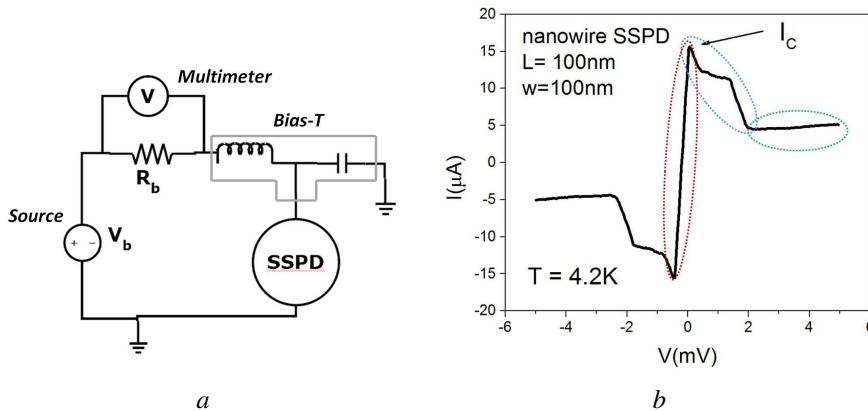
Figure 2.8 Panel a: Scheme of the external circuit used for the electrical characterization of nanowire SSPDs. Panel b: Typical IV graph of a nanowire SSPD. The dotted ovals highlight the voltage interval for which the device is in the superconducting state (red oval), the relaxation-oscillation region (blue oval) and the ohmic region (green oval). The highest current value before the relaxation-oscillation region corresponds to the nanowire critical current I_c.

In the first region, the nanowire is in the superconducting state as confirmed by the curve slope. Indeed, for this voltage interval, the slope of the curve, which is inversely proportional to the wire resistance, is ideally infinite. The non-zero resistance that can be noted from panel a of figure 2.8 is due to the resistance of the external circuit ($\sim 18\Omega$). As far as the nanowire SSPD is in the superconducting region, it can detect photons.

When the voltage bias is increased up to the point that the critical current I_c is reached, the nanowire leaves the superconducting region. At this point, a section of the wire becomes resistive and the current flowing through the device drops. The detector is in an unstable regime, the oscillation-relaxation region, where the normal section oscillates between the superconducting and normal state, causing an oscillation in the current. Since the current oscillations are faster than the readout circuit, the recorder current appearing in the graph is the average value of the current in the relaxation-oscillation regime.

When the voltage bias in increased further, the nanowire is in the ohmic region. In this phase, the ohmic region becomes stable and it starts expanding. As the graph suggests (green oval), the growth of the resistive area increases in such a way to keep the current nearly constant for increasing bias voltage.

The optical characterization is performed in the same probe station, with the addition of several instruments. As sketched in figure 2.9, a chain of four 15dB amplifiers (Mini-Circuits ZX60-6013E-S+) is connected to the RF port of the bias-T. The amplified voltage signal coming from the amplifiers is then directed to the oscilloscope (LeCroy Waveace 234) or to a frequency counter (Agilent 53230a). In order to avoid electrical reflections, a 4dB attenuator (Mini-Circuits 15542) can be inserted between the bias-T and the amplifier chain. The SSPD is illuminated via the optical window of the cryostat mainly with two continuous wave diode lasers. The laser that emits at 635nm is used to align the laser beam to the device active area and adjust its focus.
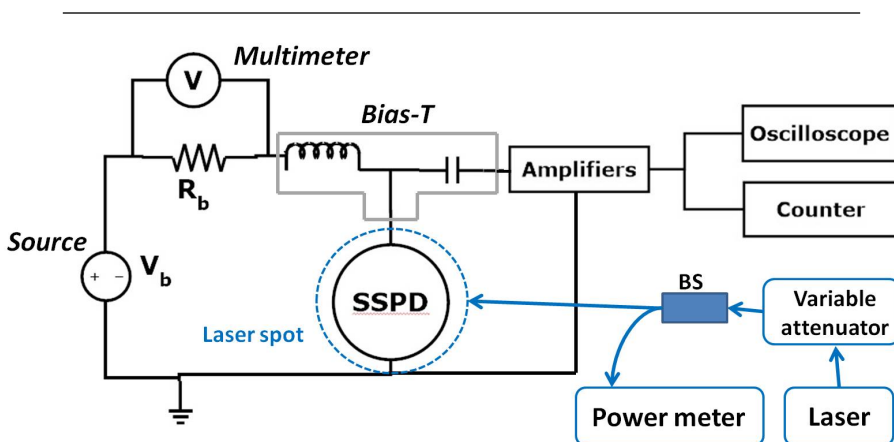

Figure 2.9 Schematics of the circuit and optical components used to optically characterize the nanowire SSPD.

The second laser emits at 1300nm and it is employed to perform the device optical characterization. Before reaching the sample surface, the laser light is fed through a PC controllable variable attenuator (OZ Optics DA-100) and a 50:50 fibre-coupled beam spitter. One branch of the beam splitter is fed to the SSPD, while the second one is connected to a power meter (Ophir Nova II) to monitor in real time the light power sent to the device. Once the previous configuration is established, the optical characterization is performed through the acquisition of the photon counts (PC) and the dark counts (DC) which are the number of detector clicks in presence and in absence of laser light, respectively. The counts acquisition is performed while varying the bias voltage and, for the PC case, at a fixed light power. Thus, while the bias voltage is swept, the counts and the current I_b flowing through the device are recorded. The typical PC and DC curves provided by a nanowire SSPD (100nm long and 100nm wide) at 4.2K are reported in panel a of figure 2.10. The device detection efficiency (DDE) is calculated dividing the counts triggered by impinging photons by the number of photons falling within the device active area. The counts triggered by impinging photons are obtained by subtracting the DC to the PC, while the number of photons reaching the active area per unit time is estimated from the light power and the dimension of both the beam spot and the device active area. The typical DDE curve provided by a nanowire SSPD is reported in panel b of figure 2.10. The maximum DDE is reached for I_b values just below I_c and, for this detector, is equal to 0.066.
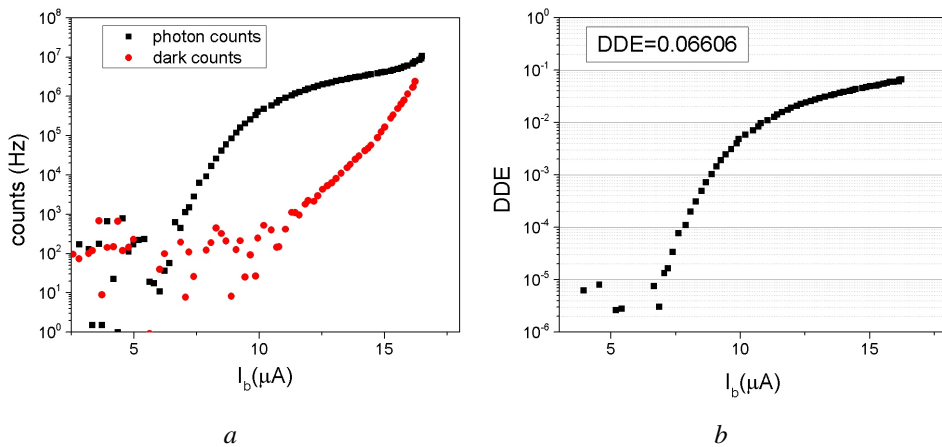

a

b

Figure 2.10 Panel *a*: Typical PC and DC curves for a nanowire detector of width and length equal to 100nm. Panel *b*: Typical device detection efficiency curve for the same nanodetector. The maximum DDE is reached with an I_b immediately below I_c and is equal to 0.066.

2.2.3 VeriCold cryocooler

The closed-cycle VeriCold cryocooler (VeriCold V04, panel *a* of figure 2.11) reaches 1.5K and permits the characterization of maximum two nanodetectors per cooling cycle. Compared to the micro-manipulated probe station, this setup offers lower cryogenic temperatures and is shielded against thermal radiation, but it does not allow a convenient systematic study of a large number of devices. The VeriCold system consists of a pulse tube cooler and a Joule-Thomson (JT) closed cycle unit. The dewar is composed of three shields and each of them surrounds a different temperature stage. From the outer (the red one in panel *a* of figure 2.11) to the inner one, the shields surround the 70K, 40K and 1.5K stages respectively (panel *b* of figure 2.11).
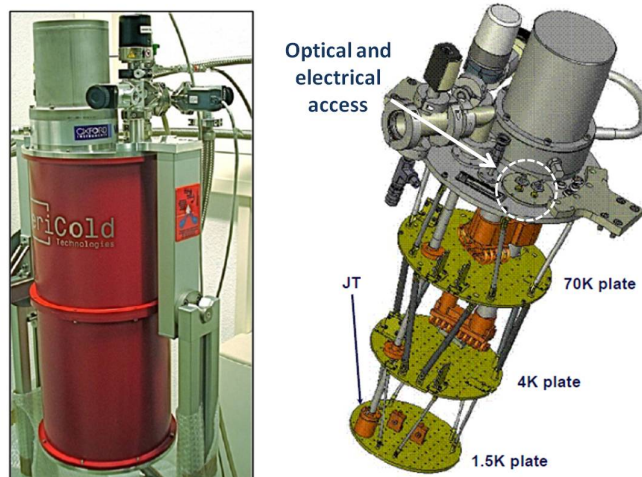
Figure 2.11 Panel *a*: Picture of the VeriCold cryocooler. The red dewar is the outer shield. Panel *b*: Schematics of the three stages as they appear once the three shields are removed. During the cooling cycle, the three stages reach, from top to bottom, 70K, 4K and 1.5K. The JT refrigerator is located in the last stage. The dashed white circle highlights the optical and electrical connections.

The inner shield mainly hosts the JT refrigerator (panel *b* of figure 2.11), the fibre used to illuminate the sample and the sample itself. More details are given by the figure 2.12, where a front and side view illustrate the components of the 1.5K stage. The sample is glued on a sample holder (panel *a* and *b*) via the LakeShore VGE varnish. The signal and ground pads of the device are connected, through wire bonding, to two pads (panel *b*) covered by Sn and In. These two pads are then connected to an SMA connector (via the blue cable

visible in panel *b*). The SMA cable, then, crosses the two upper stages to reach the top part of the VeriCold, thus providing an electronic connection with the external room temperature circuitry (dashed white circle in panel *b* of figure 2.11).
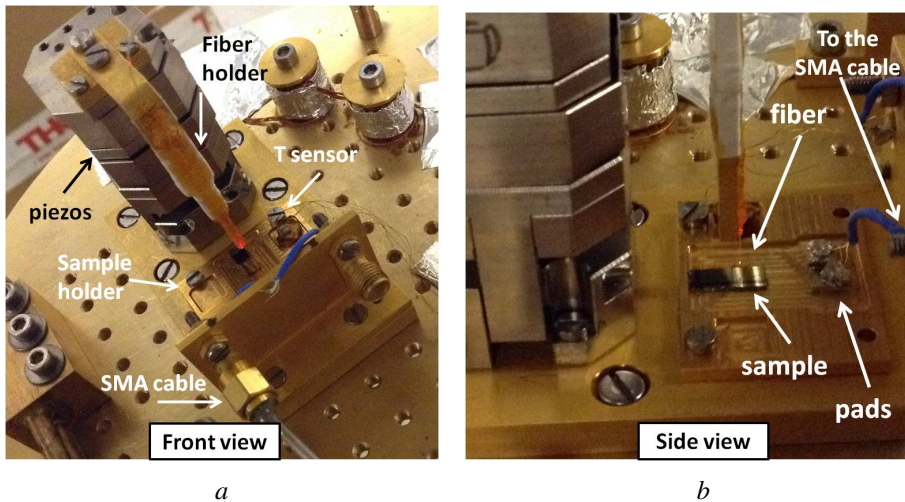
Figure 2.12 Front and side view of the 1.5K plate. Panel *a*: In the front view the fibre holder, positioned on top of a Attocube XYZ-piezo stage, is visible. Immediately under the holder, there is the sample electrically connected to an SMA connector. The temperature is measured by a temperature sensor located next to the sample and on the same sample holder. Panel *b*: Magnified side view of the fibre and sample holder. The sample, at the centre of the picture, is connected to the two pads on the right. On the left there is the piezo stage supporting the fibre holder which is right above the device to be measured.

Next to the electrical connections, there are fibre couplers to connect an external fibre with those mounted inside the VeriCold dewar. A first polarization maintaining internal fibre goes from the top of the dewar down to the 4K stage, here it is fixed to the plate and connected to another polarization maintaining fibre (WT&T designed for λ=1550nm.) that ends with a lensed tip. Before being connected to the first fibre, the lensed fibre is mounted on a removable fibre holder (panel *a* of figure 2.12) through the LakeShore VGE 7031 varnish. The fibre holder is then placed and fixed on top of a XYZ-piezo stage (Attocube) (panel *a*) so that the lensed fibre can be approached to the sample. Finally, the 1.5K stage is provided with a temperature sensor (panel *a*), which is glued on the sample holder to perform a precise temperature measurement for temperatures below 2K.

Before each cooling down, the fibre position is adjusted in order to bring the lensed fibre right above the device to be measured. Once the three shields are closed and the cooling down is launched, the only optical access to the sample is provided by the fibre. Therefore, a specific procedure is carried out to precisely adjust the lensed fibre focus and align it above the device active area. To that aim, the light reflected by the sample is exploited. The sketch in figure 2.13 shows the external components of the setup. The electrical circuit is similar to that used for the micro-manipulated probe station (see figure 2.9) except for a low noise amplifier (MITEQ), a higher precision voltage source (Yokogawa GS200) and the resistor R_b=10kΩ. The optical components are instead different with respect to the micro-manipulated probe station. The VeriCold setup is provided with a fibre optic circulator (figure 2.13) that guides the laser or LED light from the attenuator (OZ Optics polarization maintaining variable attenuator DA-100) to the lensed fibre. The choice for a circulator is dictated by the need to acquire the spectrum of the back-reflected light and monitor its power. The circulator gathers the back-reflected light from the sample and directs it toward a power meter or an Optical Spectrum Analyzer (OSA) (figure 2.13). Once the base temperature (1.5K) is reached, the fibre is lowered through the Attocube piezo stage in order to bring its focus at the sample surface. While the fibre height is reduced, a broadband LED source (WT&T LE-4, center wavelength λ_c=1525nm) is fed to the sample and the back-reflected light from the circulator is monitored with the powermeter.
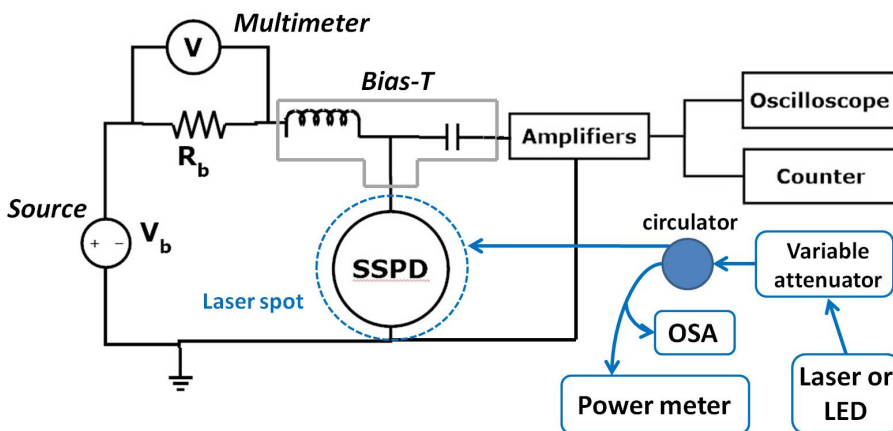

Figure 2.13 Schematics of the VeriCold setup. The setup is similar to that used for the optical characterization in the probe station. It differs only for some more precise instruments, like a low noise amplifier, and the introduction of a circulator and an optical spectrum analyzer.

During this phase the distance between the fibre and the sample surface (D_{fs}) decreases and the back-reflected power increases as shown in panel *a* of figure 2.14. After several steps downward, the descent is stopped and the circulator is connected to the OSA to record the reflected power as a function of wavelength. The distance D_{fs} determines the interference pattern between the light reflected by the sample surface and that reflected by the fibre. The distance $\Delta\lambda$ between the fringes of the spectrum is related to D_{fs} through:

$$D_{fs} = \frac{\lambda_c^2}{2\Delta\lambda} \tag{2.1}$$

Through equation 2.1 the distance D_{fs} is estimated from $\Delta\lambda$.

In panel *b* of figure 2.14, I reported the spectra recorded with the OSA after each descent. In order to highlight the fringes, the spectra are normalized by the spectrum of the light source and they are vertically translated. From bottom to top, the spectra were obtained after each subsequent descent of the fibre. Thus, the bottom black curve is acquired with the fibre far away from the sample surface and, indeed is characterized by a small $\Delta\lambda$ with respect to the top spectrum that was acquired at the focus.
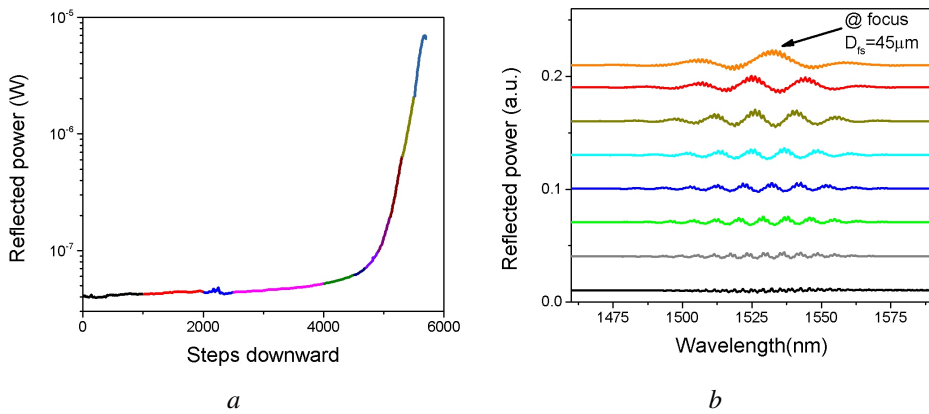
Figure 2.14 Typical graphs obtained during the descent of the fibre. Panel *a*: The reflected power collected by the powermeter is plotted as a function of steps travelled downward. The increase of reflected power and the immediate decrease after the maximum, indicates that the focal point of the fibre is on the sample surface. Different line colors corresponds to separate descents. Panel *b*: The spectra of the reflected power acquired by the OSA are normalized by the source spectrum and translated by an offset. From bottom to top, the spectra are acquired with the fibre approaching the sample. The increasing separation between the fringes provides an estimation of the distance D_{fs}.

Therefore, by monitoring the reflected power and its spectrum, a controlled descent of the fibre is performed. Since maximum reflected power is obtained in correspondence of the focus, the fibre is lowered until the highest reflected power is recorded (panel *a* of figure 2.14). This corresponds to a fringe spacing of $\sim$26nm and, therefore, to a distance $D_{fs} \sim$45μm.

Once the surface of the sample is at the fibre focus, it is necessary to find the device active area before any experiment can start. Since the alternation of gold pads (high reflectivity) and GaAs (low reflectivity) corresponds to an alternation of high and low reflected power, the fibre tip is scanned along the sample surface and, simultaneously, the reflected power is monitored via the powermeter to get an indication of the fibre position.

After the alignment is successfully completed, the circuit sketched in figure 2.13 is modified. The experiments reported in chapter 5 were performed with a broadband Fianium supercontinuum laser as a light source and a polarization maintaining beam splitter (designed for λ=1550nm) in place of the circulator. The optical fibres employed in this experiment were all polarization maintaining.

Chapter 3

Inhomogeneous critical current in nanowire SSPDs

3.1 Introduction

Superconducting single-photon detectors [3, 14] based on NbN nanowires present high speed, low dark counts and low jitter [15, 40]. Compared to more efficient SSPDs recently obtained from amorphous superconducting materials [22, 34, 36, 37, 61], NbN SSPDs allow operation at more accessible temperatures and with simpler read-out circuitry. Due to such favourable combination, SSPDs have brought a breakthrough in fields such as quantum key distribution (QKD) [62, 63], nanoscale imaging [64] and quantum optics [65]. However, the number of possible applications is still limited by the low fabrication yield. Indeed, realizing arrays of SSPDs with the same performance is challenging. Understanding and solving this issue could enable free-space single-photon imaging [66], spatial and photon-number resolution [67–69] as well as circumventing dead time limitations in interplanetary optical communication [9].

The physical reason for the poor reproducibility must be sought in the SSPD operating principle: for efficient operation, NbN SSPDs must be biased with a bias current (I_b) slightly lower than the critical current (I_c). In this condition, the diffusion of photocreated quasi-particles, together with the vortex unbinding, results in a voltage pulse in the readout circuit [70]. This requires the nanowire to be extremely homogeneous, so that the critical current is

uniform along its entire length. Recent studies [50, 51] on meander SSPDs showed a variation in detection efficiency among nominally identical devices. The variation has been ascribed to highly localized areas of the nanowire, named constrictions [50], characterized by a reduced cross section. The large active area of the meander SSPD used in those studies, though, does not allow a straightforward investigation of such defects. Indeed as mentioned in Chapter 1, the dimensions, density and physical origin of these constrictions are still unknown. In order to address this question, we realized and investigated simpler detectors whose active areas consist of short wires with different lengths (L) and fixed width (w=100nm).

3.2   Experiment

The nanowire SSPDs are patterned from a 5nm-thick NbN film, named NbN20, which is deposited on GaAs(001) substrate at a nominal ambient temperature of 400 ^{o}C. These deposition conditions, similar to those previously used to fabricate high-performance meander- and waveguide-SSPDs [28, 29], allowed the realization of a film with critical temperature $T_c = 9.7K$ and transition width $\Delta T_c = 0.34K$[1].
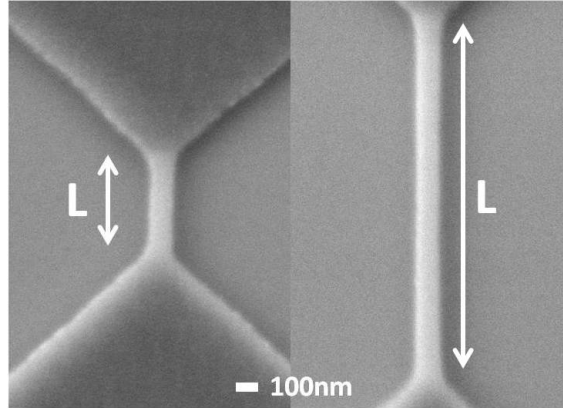
Figure 3.1 SEM micrograph of 100nm wide nanowires with lengths
L=400nm (left) and L=1600nm (right).

The nanowire patterning process was optimized in order to fabricate 100nm wide nanowires with lengths L ranging from 100nm to 15μm. In order to prevent latching [15] an additional meander (500nm wide and 573μm long) is defined together with the nanowire to

---

[1]The values of T_c and ΔT_c are calculated according to the procedure reported in reference [59].

provide an estimated series inductance of 100nH [58]. Figure 3.1 shows the scanning electron microscope (SEM) image of two nanowires with different lengths. A chip containing 16 nominally identical nanowires for each length L, with L=100nm, 400nm, 1.6µm and 15µm, is electrically and optically characterized at an estimated temperature of 5K. The measurements are performed in a single cooling run in the cryogenic probe station described in Chapter 2. While it limits the statistics, this procedure ensures that all the devices are characterized at the same effective temperature.

3.3   Electrical response

The measured critical currents (I_c) are displayed in figure 3.2 as a function of nanowire length. The data, covering more than two orders of magnitude in wire length, shows a clear trend.
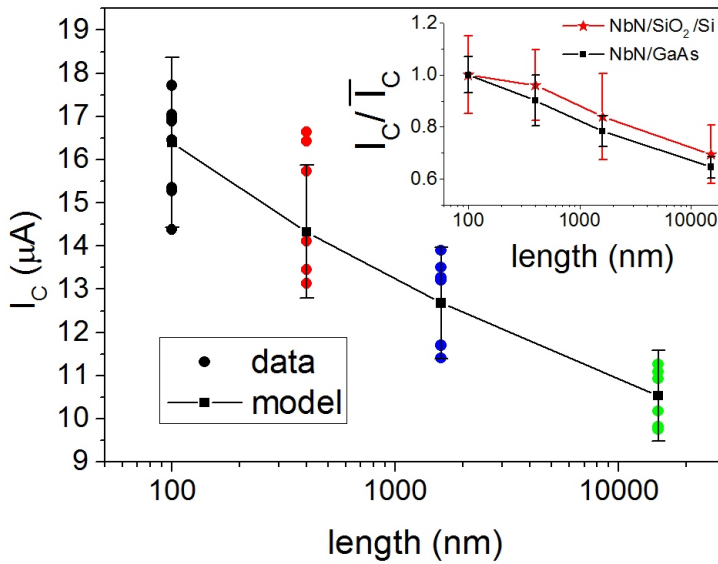
Figure 3.2 The I_c experimental values are displayed as a function of nanowire length (filled circles) and are superimposed to the $\bar{I}_c$ (black squares) and the standard deviation (error bars) calculated with the microscopic model. *Inset*: The data of the main panel is reported together with the data obtained from a commercially available NbN film deposited on a different substrate. For a clear comparison, both sets of data are normalized to their mean I_c ($\bar{I}_c$) and the standard deviation ΔI_c is calculated (error bars). In both the inset and in the main panel the lines are guides to the eyes.

The critical current, ideally independent of wire length, decreases with increasing length. In addition, the I_c values present a large spread, as measured by the standard deviation ΔI_c, even for the shortest wires, for which the spread is maximum. To highlight the previous observations, we reported the same set of data in the histogram of figure 3.3 (panel a).
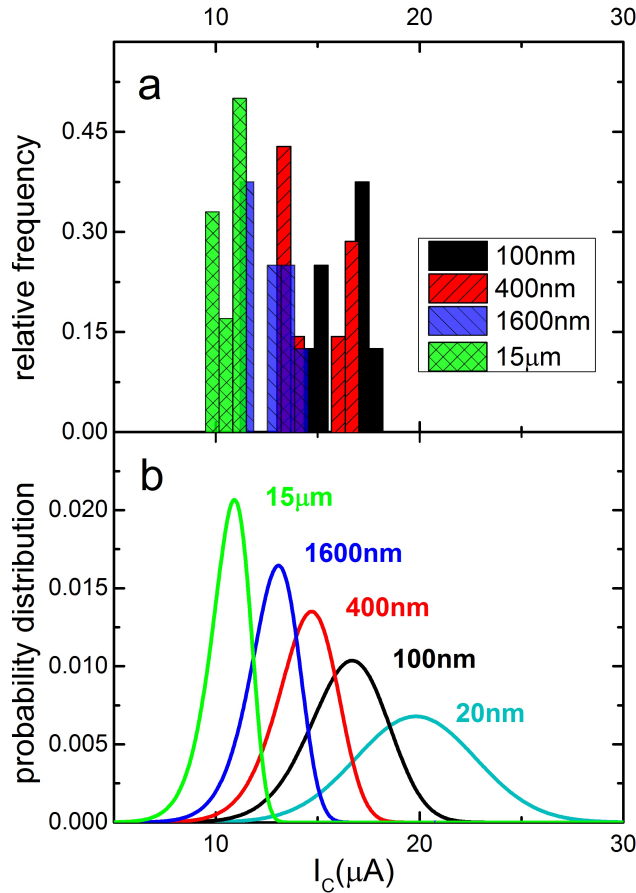
Figure 3.3 The experimental I_c histograms in panel a are compared to the I_c probability distributions calculated from the model (panel b). The light blue curve in panel b is the calculated probability distribution for a 20nm long section.

The variation of I_c values among nominally identical devices constitutes a direct proof for the inhomogeneous nature of the wire. A more intriguing feature is the decrease in the $(\bar{I}_c)$ encountered already between 100nm and 400nm long nanowires. These observations

reveal that each nanowire presents a continuously inhomogeneous distribution of I_c with correlation length shorter than or equal to 100nm. Indeed, if the nanowire was homogeneous on a 400nm length scale, for example, we would not observe any decrease in the average I_c between these and the 100nm long wires.
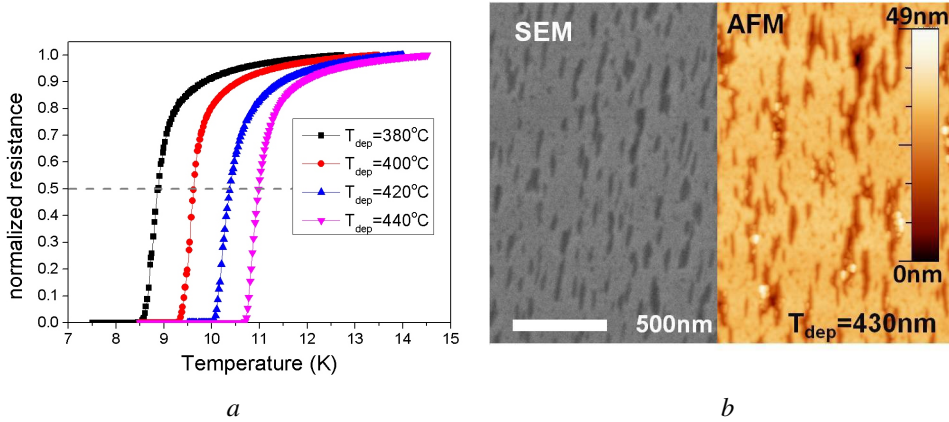
Figure 3.4 Panel *a*. The normalized resistance of four films deposited at different T_{dep} is plotted as a function of temperature. The temperature value corresponding to 50% of the normalized resistance (horizontal dashed line) is an indication of the film T_c. Panel *b*. SEM and AFM micrographs of a NbN film deposited at T_{dep}=430 ^{o}C.

Since the quality of NbN thin film depends on substrate temperature [28, 71, 72], it is interesting to extend the investigation of the film homogeneity to NbN films deposited at different temperatures T_{dep}. Several NbN films with similar thickness are deposited at T_{dep} ranging from 380 ^{o}C to 440 ^{o}C. The normalized film resistance reported in figure 3.4 (panel *a*) as a function of temperature reveals that films deposited at $T_{dep} \leq 380$ ^{o}C are characterized by $T_c < 9$K while those deposited at $T_{dep} \geq 415$ ^{o}C show $T_c \sim 10.5$K. Although the latter films could appear better candidates for SSPD fabrication, they show higher surface roughness which leads to detectors with low I_c and poor optical response. The SEM and AFM images in panel *b* of figure 3.4 indicate the presence of *craters* in the NbN films deposited at T_{dep}=430 ^{o}C. Indeed, while the high T_{dep} could favour the deposition of NbN film with larger crystal grains and therefore higher T_c [71] it can also cause desorption of As from the GaAs substrate [28, 72], which makes the surface rough. In this case the NbN film which grows following the morphology of the underlying substrate, would have a rough surface due to its reduced thickness. The low T_c values obtained with $T_{dep} < 380$ ^{o}C and the

high film roughness encountered for $T_{dep} \geq 420\ ^oC$ suggest that the interesting temperature range can be restricted to the interval $380\ ^oC \leq T_{dep} \leq 415\ ^oC$. In addition to NbN20 grown at $T_{dep}=400\ ^oC$, two other NbN films, named NbN30 and NbN33, were deposited at $385\ ^oC$ and $415\ ^oC$ respectively. The main differences among the three films are reported in table 3.1.

	$T_{dep}(\ ^oC)$	$T_c(K)$	thickness (nm)
NbN30	385	9.2	5.05±0.03
NbN20	400	9.7	4.86±0.03
NbN33	415	10.3	4.86±0.03

Table 3.1 The deposition temperature, the film thickness and the critical temperature T_c are reported for the three NbN films taken in consideration in this appendix.

The same fabrication process was performed on the three NbN films and identical nanowires with lengths L=100nm, 400nm, 1600nm, 15µm and width w=100nm were realized on each chip. In figure 3.5 the critical current values of the nanowires obtained from the films NbN30 and NbN33 are reported as a function of nanowire length L. Both graphs show a behaviour similar to that reported in figure 3.2.

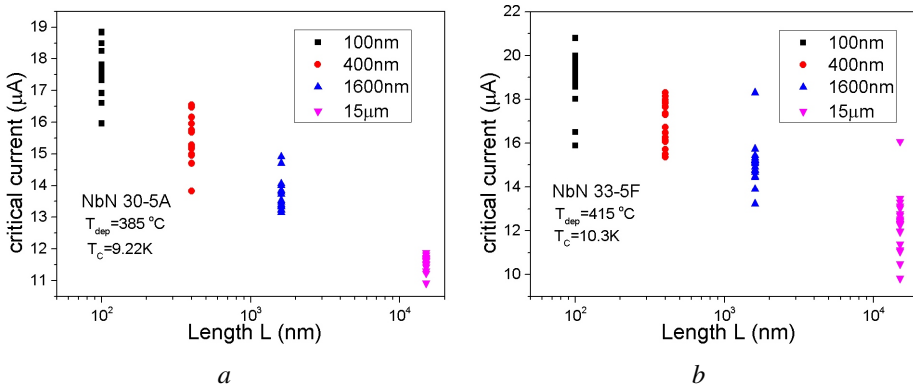*a*   *b*

Figure 3.5 Experimental critical current values acquired from the film NbN30 deposited at $385\ ^oC$ (panel *a*) and NbN33 deposited at $415\ ^oC$ (panel *b*) are displayed as a function of nanowire length L.

Therefore, the trends in figure 3.5 confirm the inhomogeneous nature of NbN film obtained with a deposition temperature $385\ ^oC \leq T_{dep} \leq 415\ ^oC$. The possible dependence of the film inhomogeneity on the deposition temperature could be observed by comparing the experimental data of the three films. Since the three different chips were characterized in three separate cooling runs and the average $I_c(L)$ is determined by the film T_c and the experimental temperature, it is convenient to compare the values of I_c normalized to the $\bar{I}_c$ of the shortest wires. The graph in figure 3.6 (panel a) reveals an overlap between the three data sets. This result suggests that, within the examined temperature range, the dependence of film inhomogeneity on T_{dep} is negligible. In addition to the three NbN films considered so far, another film, named C177, was processed. The film C177 was deposited at T_{dep}=400 ^oC and is characterized by T_c=10.3K and thickness $\sim$5nm, therefore it is similar to the three films examined previously and can be considered for comparison. In order to probe the inhomogeneity on a shorter length, the film was processed to obtain nanowires with width w=150nm and lengths L=0nm (the bow-tie constriction), 100nm, 200nm and 400nm. The critical current values and the mean value $\bar{I}_c$ are reported in figure 3.6 (panel b) as a function of nanowire length. Indeed, the decrease of $\bar{I}_c$ occurring already between the 0nm constriction and the 100nm long nanowire confirms the non uniformity of the NbN film and suggests that the typical inhomogeneity length scale is shorter than 100nm.

a

b
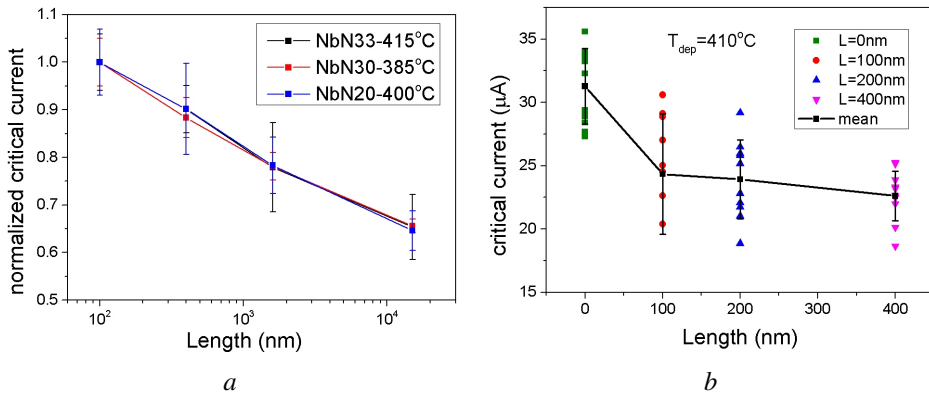
Figure 3.6 Panel a: The normalized critical currents (squares) and the standard deviation (error bars) for the three deposition temperatures are plotted as a function of the wire length. Panel b: The I_c values of 150nm wide nanowires obtained from a different NbN film are plotted as a function of wire length. The mean values and the standard deviation are also reported (black squares and error bars). In both panels the lines are guides to the eyes.

In this case, the $\bar{I}_c$ decrease from 100nm to 400nm long wires is somewhat smaller, which could be a statistical deviation due to the limited number of data points.

Moreover, since the NbN film quality can vary with the substrate [73], it is important to understand whether the trend reported in figure 3.2 is only typical of our NbN films on GaAs. To this aim, we realized and characterized the same detectors on a commercial NbN film deposited by SCONTEL Superconducting Nanotechnology [57] on a (250nm)SiO_2/Si(001) substrate. The NbN film had a critical temperature $T_c = 10.0K$. Since the silicon dioxide layer has much lower thermal conductivity than Si and GaAs [74–76], the devices could not reach an operational temperature lower than T_c in the cryogenic probe station. For this reason the characterization of those devices is performed at ∼2K in another cryogenic probe station provided of a smaller optical window giving a lower thermal load. In order to compare the characterization results with the experimental data of figure 3.2 (main panel), data normalization is necessary. In the inset of figure 3.2 we compare the $\bar{I}_c$ and ΔI_c values obtained from the two samples where both sets of data are normalized to the $\bar{I}_c$ of their 100nm long wires. The graph clearly shows that the reported behaviour is not unique to our NbN films. In fact, also detectors patterned from the NbN/SiO_2 film are characterized by the decrease of $\bar{I}_c$ with increasing length, and they have a large spread in critical current ΔI_c for each length. It is worth noticing that in both samples the ratio between the normalized $\bar{I}_c$ of the longest and shortest wires is almost 0.6. While we cannot exclude that more homogeneous films may be obtained by varying the deposition conditions, as the results in reference [50] suggest, the observed inhomogeneity is likely typical of NbN films used for SSPD fabrication.

To gain more insight, we calculated the theoretical depairing current (I_c^{dep}) and compared it with the I_c values resulted from our measurements. The depairing current is estimated according to the Ginzburg-Landau model and the temperature dependence proposed by Bardeen [45, 77]. In the I_c^{dep} estimation we considered the following quantities: the measured sheet resistance in the normal state R_s=870Ω/sq, the diffusivity D≈0.5 cm^2/s of NbN films [78], the measured critical temperature T_c=9.7K and the energy gap at zero temperature $\Delta(0)$=2.07$k_B T_c$ [78]. For a 100nm wide nanowire operating at 5K, I_c^{dep} ∼21μA. We note that the I_c of the long wires is almost half of the calculated I_c^{dep} as previously observed [32, 45]. Our results therefore suggest that the inhomogeneity is the main reason for the low observed critical currents in long meanders.

We developed a simple microscopic model (see Appendix 3.ii) to endorse our experimental observations. The nanowire is modelled as a chain of identical sections (width 100nm and length s) each of which has a different critical current I_{ci}. We assume that the probability for a section to have a certain I_{ci} is given by a Gaussian probability distribution with mean

value μ and standard deviation σ. For a wire of N sections (N=L/s) the critical current $I_{c,wire}$ will be given by the minimum I_{ci} among the N different values. For each wire length and for a given (μ, σ), we calculate the probability that the entire chain of sections has the critical current $I_{c,wire}=i_c$, where $0< i_c < 50\mu A$. The model starts with an initial guess for (μ, σ) and proceeds by iterating the probability calculation for different (μ, σ). The model stops when the pair (μ, σ) that minimizes the χ^2 between the modelled and experimental $\bar{I}_c$ is found. Since the only requirement for the section length is not to exceed 100nm, such procedure was applied to the cases s=20nm, 50nm and 100nm and the obtained pairs (μ, σ) were (19.82μA, 2.94μA), (17.88μA, 2.54μA) and (16.49μA, 2.23μA) respectively. A comparable agreement between the experimental and modelled $\bar{I}_c$ can be found with any section length s$\leq$100nm. In the following we will focus on the case s=20nm. The calculated I_c probability distributions (for I_c intervals of 0.2μA) are reported in figure 3.3 (panel b) together with the Gaussian distribution for the I_c of the 20nm section. This graph, when compared to the histograms of panel a, clearly shows that the decrease in both $\bar{I}_c$ and σ is reproduced quantitatively by this simple model. In addition, in figure 3.2 the average I_c values and the standard deviations predicted by the model are superimposed to the experimental results. The agreement further proves that with simple assumptions we can quantitatively describe the electrical behaviour of our devices. Furthermore, it is important to notice that the best estimate of the average critical current for the 20nm section is very close to the theoretical depairing current, which further supports our interpretation.

3.4   Optical response

The previous experimental results, which show that a long wire can only be biased at almost half of the $\bar{I}_c$ of the shortest wire, suggest that the internal detection efficiency ($\eta_{internal}$) of SSPDs can be strongly limited. To extract more information about the effect of inhomogeneities on the efficiency, we studied the optical response of selected wires. For each wire length, we selected 5-6 devices and measured them during two consecutive cooling runs. To ensure temperature reproducibility, we made sure that the measured I_c values were the same within 1.2% in both cooling runs. During the optical characterization, a laser beam at λ=1300nm is focused onto a spot with full-width-half-maximum of 20 μm to illuminate one detector at a time. For each nanowire length, the light power is chosen in order to avoid multi-photon response and device heating. For this last purpose, the ratio between the device critical current measured with and without laser spot is always kept above 0.96. In these conditions, we recorded detector counts with (photon counts, PC) and without (dark counts, DC) laser spot while varying the bias current, I_b. The DDE is calculated by normalizing the

difference between PC and DC by the number of photons impinging on the detector active area (100nm×L). We note that this definition of DDE slightly differs from that used for meander detectors where the entire area of the device is considered.

The DDE curves in figure 3.7 (main panel) show that a detector responds to incoming light with its highest efficiency only when it is biased very close to its I_c. As a consequence of the I_c decrease with increasing detector length, the DDE curves of short nanowires always extend to higher I_b and DDE values with respect to the long nanowire case. The previous observation is made explicit by the inset of figure 3.7 where the maximum detection efficiency values are plotted as a function of the I_c.
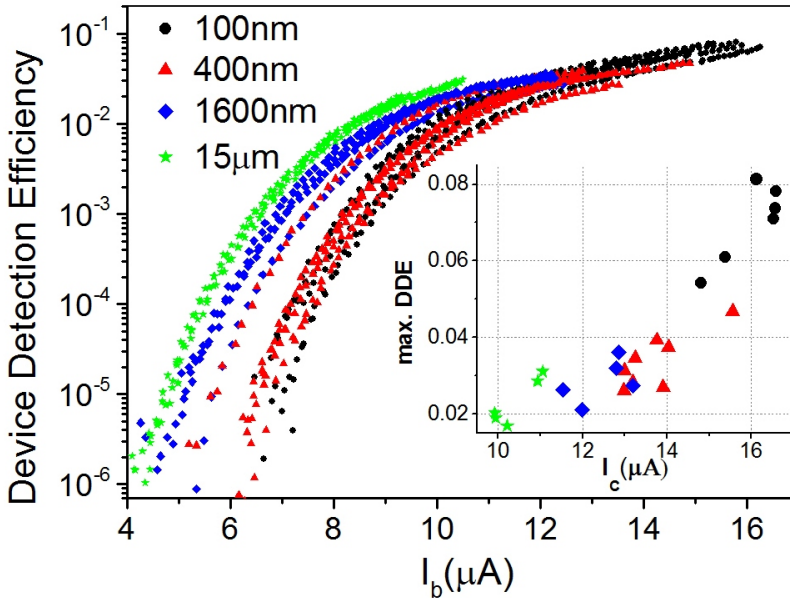
Figure 3.7 Device detection efficiency curves for nanowires of different lengths are plotted as function of I_b. *Inset*: Maximum detection efficiency data is plotted as a function of device I_c.

The inset clearly shows how a lower I_c corresponds to a lower DDE. In addition, the curves of the main panel show that at fixed and low I_b the long wires appear to be more efficient than the short ones. This trend is surprising, since at fixed bias current we would expect the same average efficiency in short and long wires (where the long wires effectively average over many short sections). This effect could result from the limited statistics available,

whereby short wires with low I_c, and therefore much more efficient at low I_b, are not likely to be measured. In order to deepen our understanding of the device optical response, we modelled it by assuming that each wire section contributes to the efficiency according to an universal efficiency curve (see Appendix 3.i.2).
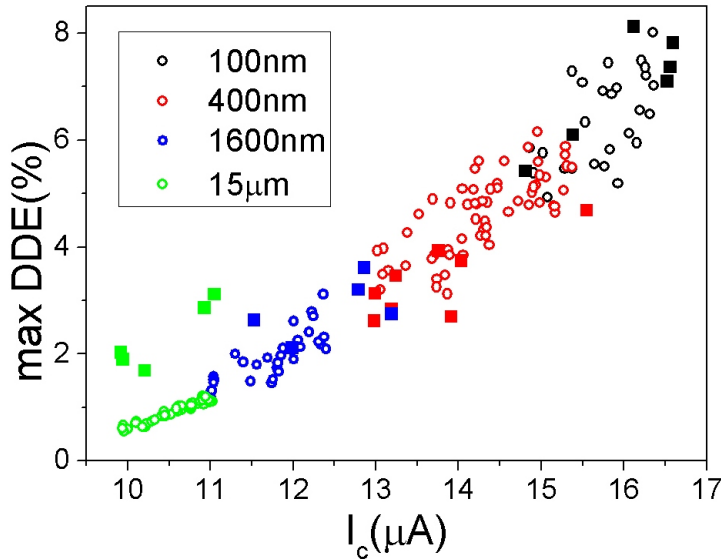
Figure 3.8 The experimental (filled squares) and calculated (open circles) maximum values of DDE are reported for each nanowire length as a function of the nanowire I_c.

In figure 3.8 the experimental and modelled maximum values of DDE are plotted as a function of the wire I_c. This comparison reveals that the model, although simple, qualitatively describes the optical behaviour of nanowire SSPDs. However, the poor agreement between the experimental and calculated maximum DDE for the longest wires (green circles and squares) encouraged us to take a closer look at the DDE curves. In figure 3.9 each panel shows the experimental data points and calculated DDE curves for each wire length L. The good agreement in panel *a* (case L=100nm) is not surprising since the universal curve was chosen to resemble the experimental DDE curve of a 100nm long wire. While panels *b* and *c* show that the optical response of wires with lengths L=400nm and L=1600nm is well described by the model, panel *d* reveals that the model is underestimating the detection efficiency of the longest wires. In order to investigate the possible reasons for such a discrepancy we explored the issue from different perspectives.
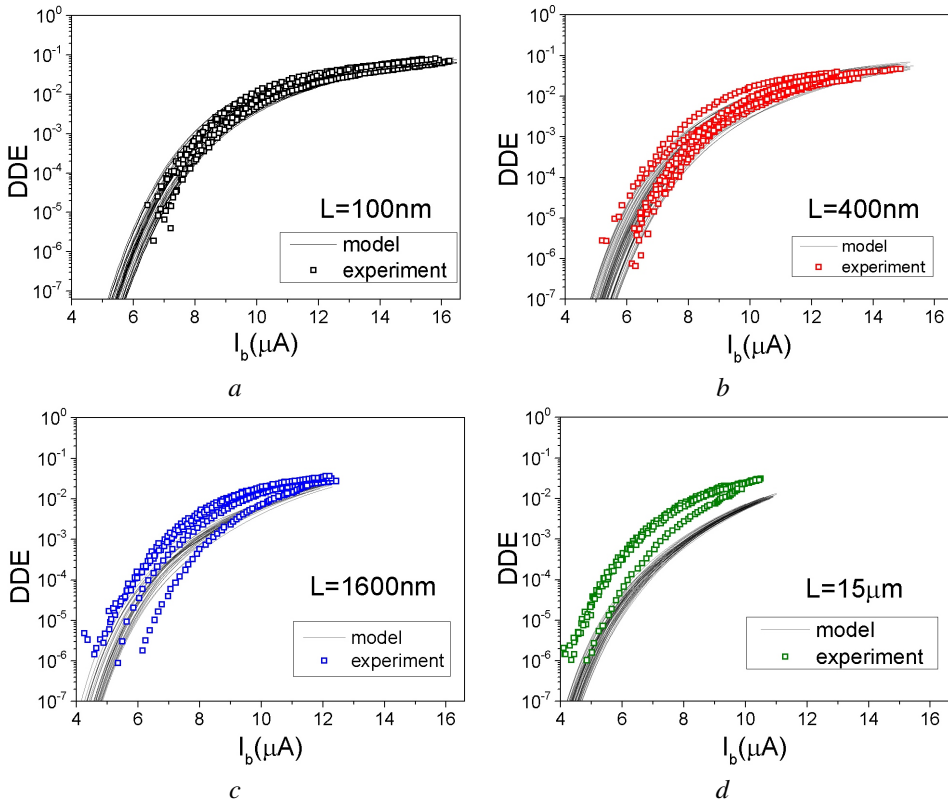
Figure 3.9 For each wire length *L*, the measured device detection efficiency (open squares) and the model prediction (solid lines) are reported as a function of bias current.

A first question is whether the wires are working as single-photon detectors in the entire current range and for the input power employed in these experiments. Let us assume that, at low bias currents, the shortest nanowires detect only two or more photons. Since the 100nm long wires are taken as reference to choose the universal curve, the calculated detection efficiency at low I_b could be underestimated. Therefore the presence of multiphoton detection could explain the discrepancy in panel d of figure 3.9. In order to probe how many photons are needed to trigger a detection, we recorded the optical response of the detectors while varying the input power. By repeating this procedure for different I_b values, we obtain the curves reported in figure 3.10. The slope of the measured curves reveals the number of absorbed photons necessary to trigger a detection event. The panels of figure 3.10 indicate that for both nanowires of length L=100nm (panel a) and L=15µm (panel b) the slope of the curves is ∼0.9 at the experimental input power of ∼200µW and ∼6µW respectively. Since the curves slope does not exceed 1, it is possible to conclude that, at the examined input powers, the detection events are mainly triggered by single photons. Therefore, such result excludes that the discrepancy reported in panel d of figure 3.9 could be related to a wrong estimation of the universal curve due to multiphoton detection.

Figure 3.10 The measured photon counts obtained at five different I_b are plotted as a function of impinging light power for a 100nm long wire (panel a) and a 15µm long wire (panel b). In each graph, the vertical line indicates the light power during the experiment. The slope of the curves, highlighted by the black arrow, shows that the devices mainly detect single photons.

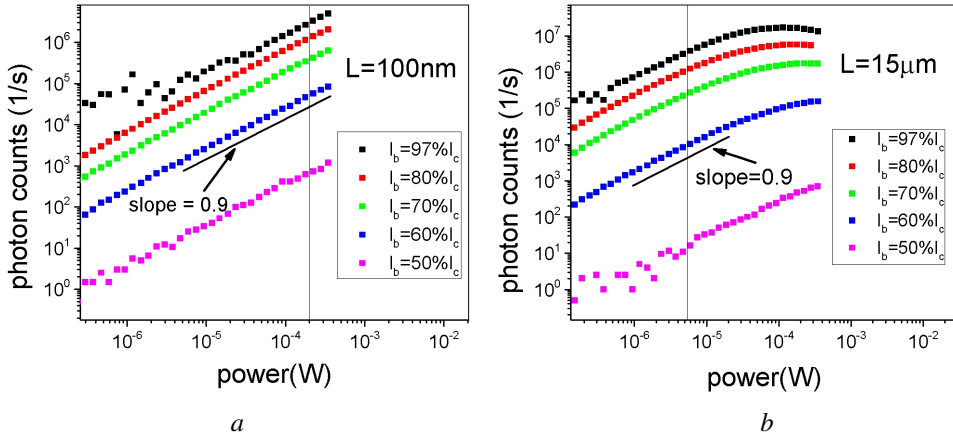The underestimation of the DDE curves observed in figure 3.9 (panel *d*) could be due to the underestimation of the number of sections with low I_c. Let us consider the extreme case in which only one section in the chain has the lowest critical current, I_c', and all the others have the same high value of I_c. In this case the highest contribution to the efficiency is given only by that section with the I_c' because it is the only one to be biased close to the $I_{c,wire}=I_c'$. For this reason, the choice of the probability distribution in equation 3.1 and, more specifically, the decay of its tails can be crucial. In order to improve the description of the detector optical response, we explored probability distributions alternative to the Gaussian one involved in equation 3.1. Among the examined alternatives, we considered the left half Gaussian distribution and the Lorentzian distribution which has slowly decaying tails. Despite the numerous attempts, all the probability distributions considered did not lead to a successful description of the device electrical behaviour. An example is provided in the figure 3.11 where the calculated values of $\bar{I}_c$ were obtained by assuming that the I_{ci} values follow a Lorentzian probability distribution. The disagreement with the experimental data reveals how crucial the choice of the probability distribution is.
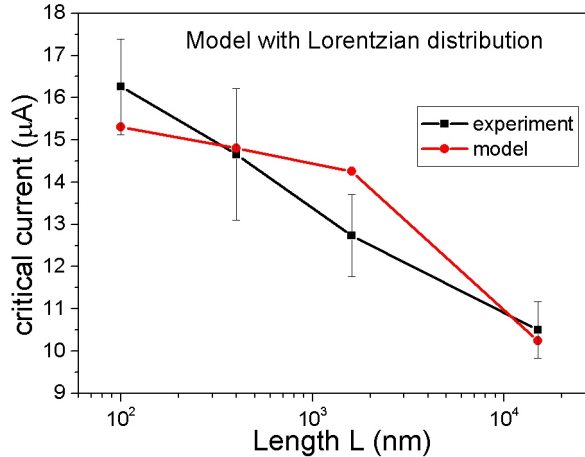
Figure 3.11 The experimental values of $\bar{I}_c$ (black squares and line) are compared with the calculated ones (red dots and line) obtained assuming a Lorentzian probability distribution for the I_{ci}. The lines are guides to the eye.

The reason for the disagreement between calculated and experimental optical response could be related to the simplicity of our model. We know from our recent understanding [79] that the photon detection in nanowire SSPD is position-dependent. Therefore, considering

the wire as composed of sections of width 100nm and length 20nm and assuming that the efficiency of the section is constant along its width could constitute a too simple picture that falls short in describing the efficiency of a nanowire SSPD.

3.5   Origin of inhomogeneity

In our search for the origin of inhomogeneity, we extensively investigated the SEM micrographs of our nanowires. Figure 3.12, where an SEM micrograph for each wire length is reported, shows the uniformity of the wire width and the absence of patterning defects. In order to quantify the quality of the patterning, the wire widths were measured with the image processing software WSxM [80] revealing a relative standard deviation of 2.7%. Since such value is smaller than the relative variation in the I_c: $\Delta I_c / \bar{I}_c \sim 6.1\%$, we can exclude that the small variations in the measured wire width constitute the sole origin of the inhomogeneous I_c.
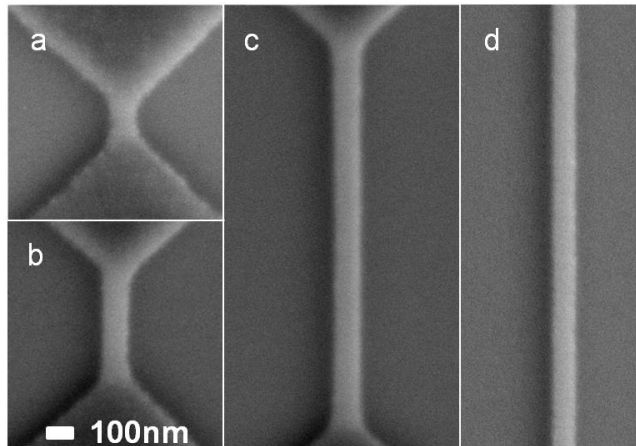
Figure 3.12 High resolution SEM micrographs of wires with length L=100nm (panel *a*), L=400nm (panel *b*), L=1600nm (panel *c*) and L=15µm (panel *d*).

In a recent work [81] the presence of electronic inhomogeneities in a NbTiN thin film is proposed on the basis of a step-like feature in the so-called re-trapping current. The authors observe that when the NbTiN nanowire is driven from the conducting to the superconducting state by reduction of the applied voltage, the current flowing in the wire decreases in a step-like pattern regardless of the wire geometry. The authors analyse the system behaviour in

the framework of the theory presented in [82] and suggest that the step-like feature could be due to electronic inhomogeneities. However, these inhomogeneities are typical of a strongly disordered (non-granular) amorphous superconductor and, thus, the theoretical framework presented in [82] does not apply to our NbN thin film, which is polycrystalline.
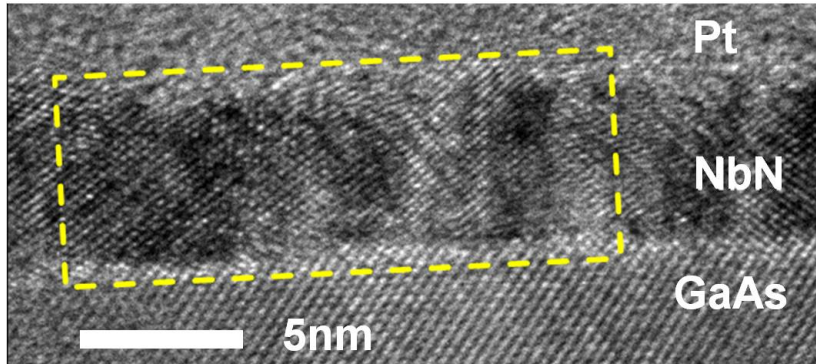
Figure 3.13 High resolution TEM micrograph of a NbN film deposited at 410 ^{o}C [2].

The origin of the inhomogeneous I_c observed in our samples can be tentatively attributed to the variation of film thickness and/or crystal properties. The high resolution TEM image in figure 3.13 reveals that a NbN thin film is characterized by thickness variations and a polycrystalline structure. While the polycrystalline structure could imply the presence of voids between the nano-crystals [71, 83], the thickness fluctuations could lead to a local variation of the I_c.

3.6   Conclusion

We have investigated the inhomogeneous nature of NbN nanowires by systematically studying the critical current and efficiency of wires with different lengths. The observed trends strongly indicate that the wires are inhomogeneous at a length scale shorter than or equal to 100nm. Such trends in the electrical and optical response cannot be explained with the presence of isolated constrictions as suggested in references [50] and [51]. In the case of a point-like constriction, for example, the wire would not respond efficiently to light except for an isolated

---

2 The TEM image is taken from the PhD thesis of Dr. Dondu Sahin. "Waveguide single-photon and photon number-resolving detectors", Chapter 3.

point. As a consequence, the DDE curves of wires with different length would overlap and differ only in the ending point since only the DDE curves of short wires would extend until high I_c values. Moreover, the continuous decrease in $\overline{I_c}$ observed with increasing L is an indication of the short inhomogeneity length scale and allows us to exclude the isolated nature of the constriction.

While more investigations are needed to determine the physical origin of the I_c non-uniformity, the SEM and the TEM images of paragraph 3.5 already suggest that the polycrystalline structure and the small thickness fluctuations in the NbN film are likely candidates.

We note that the proposed experimental method, based on the measurement of the critical current for a number of short wires, enables a simple and reproducible assessment of the film homogeneity and thereby provides more information than extensive DDE measurements on long meanders.

3.i Appendix: The microscopic model

3.i.1 Description of the electrical behaviour

The nanowire of length L can be seen as a chain of N identical sections, each of which has its own critical current I_{ci} (figure 3.14). The sections have the same width as the nanowire but length $s=L/N$.
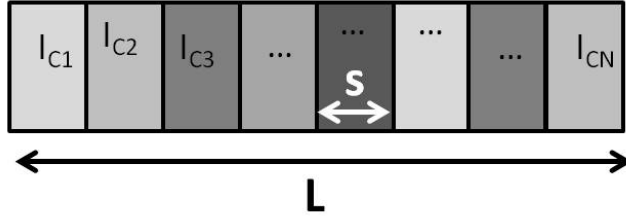
Figure 3.14 Sketch representing the chain of sections considered in the model. Each section has length s and critical current I_{ci}.

In order to estimate the probability that the nanowire has a critical current $I_{c,wire}=i_c$, we suppose that the probability that a section has $I_{ci}=i_c$ is given by the Gaussian probability distribution $G(i_c)$ characterized by the mean value μ and the standard deviation σ. Since $I_{c,wire}$ will coincide with the lowest value of I_{ci}, the probability that the wire has critical current i_c is given by the probability that at least j sections ($j \geq 1$) have $I_{ci}=i_c$ times the probability that the remaining (N-j) sections have a critical current higher than i_c. Since there is no restriction on how the j sections should be distributed along the wire, the probability that the nanowire has critical current i_c can be written as:

$$P(I_{c,wire} = i_c) = \sum_{j=1}^{N} \binom{N}{j} G(i_c)^j (1 - G_{CDF}(i_c))^{N-j} \qquad (3.1)$$

where $G_{CDF}(i_c)$ is the Gaussian cumulative distribution function. The probability distribution is obtained by evaluating P from equation 3.1 over a range of i_c values.

Once the probability distribution $G(i_c)$ is defined by an initial guess of the parameters μ and σ, the probability in 3.1 is calculated for each wire length L in the range 0μA$\leq i_c \leq$50μA.

This section deals with the model developed by Koen M.P. op 't Hoog and reported in chapter 4 of his Master thesis: "The role of inhomogeneities in nanowire superconducting single photon detectors", Eindhoven University of Technology, Applied Physics Department, 2014.

This procedure is then iterated and the parameters μ and σ are changed until the best agreement with the experimental data is reached. As mentioned in this chapter, the experimental data is described best by a chain of sections long s=20nm whose critical current values are distributed according to $G(i_c)$ with μ=19.82μA and σ=2.94μA.

3.i.2 Description of the optical response

The graph in figure 3.7 (main panel) reveals that the device detection efficiency (DDE) reaches the highest I_c value only for the short wires. This behaviour can be explained by the non uniformity of the wires which affects the long wires maximally. When a section, characterized by I_c, is biased close to its critical current, another section, which has a higher $I'_c > I_c$, will be biased far away from its critical current. Therefore the latter section will contribute less to the detection efficiency with respect to the former one. In order to model such optical behaviour, we assume that each section contributes to the total DDE according to a universal efficiency curve that is a function of $I_b/I_{c,section}$. This seems reasonable since we know that the dimension of photo-excited quasi-particle cloud is of few tens of nm (as it will be discussed in chapter 4).

Since the optical response of the shortest wires is the closest to that of a single section, it is possible to consider the DDE curve of those wires as an approximation of the universal efficiency curve. Such curve was determined by adapting the generalized logistic function [84] to the experimental DDE curve of the shortest wires. Once the universal efficiency curve is defined, an I_{ci} value is assigned to each of the N sections according to the same Gaussian probability distribution used in the previous paragraph to describe the device electrical behaviour. Then, for each I_b value between 0μA and $I_{c,wire}$, the efficiency of each section is read from its universal curve. The sum of these contributions gives the calculated DDE curve of the entire wire as a function of I_b. This procedure is iterated 100 times for each wire length L. Finally, a selection is performed on the calculated curves: only those having $I_{c,wire}$ similar to the experimental I_c are considered.

Chapter 4

Detection mechanism in NbN nanowire superconducting single photon detectors

4.1 Modified quantum detector tomography

Quantum detector tomography (QDT) [85] provides the complete characterization of the detector multi-photon response without need for any assumption on the detection mechanism. The purpose of this technique is to derive the probability of a detection event when i photons are incident on the detector. Such characterization is achieved by measuring the detector response when illuminated with coherent quantum states of different input power. The probability to observe a detection event R_{click} is given by the sum of the products of the probability p_i that i photons trigger a detection event and the probability $c_i(N)$ that i photons impinge on the detector. For coherent states the photon number distribution is completely determined by the mean photon number N since $c_i(N) = e^{-N} \frac{N^i}{i!}$. For a detector with only two possible outcomes (click and no click), reasoning in terms of the no click probability $R_{noclick}$ is more convenient. We write the probability of observing a detection as a function of mean photon number N as

$$R_{click}(N) = 1 - R_{noclick}(N) = 1 - e^{-N} \sum_{i=0}^{\infty} (1 - p_i) \frac{N^i}{i!} \qquad (4.1)$$

Once the optical response is measured as a function of input power, by fitting R_{click} using the calculated $c_i(N)$ and p_i as fitting parameters, it is possible to achieve the complete description of the detector. However, the implementation of QDT is non trivial for the detectors examined in this thesis. For these devices, characterized by a low detection efficiency, there is a low probability (η) that an impinging photon participates to the detection event and therefore the tomography outcome can be influenced by the linear losses. A modified quantum detector tomography [86] was introduced to address this issue. A detector with large linear loss can be thought of as an ideal detector which is illuminated by an attenuated set of coherent states. Since a coherent state remains such under attenuation, we are allowed to separate the linear efficiency η from the non-linear response p_i.

$$R_{click}(N) = 1 - e^{-\eta N} \sum_{i=0} (1 - p_i) \frac{(\eta N)^i}{i!} \tag{4.2}$$

To obtain the values of η and p_i, we can fit equation 4.2 with the following set of parameters $\{\eta, p_0, p_1, ..., p_\infty\}$. By isolating the linear loss, we introduced the extra parameter η to strongly reduce the number of fitting parameters p_i in the tomography.
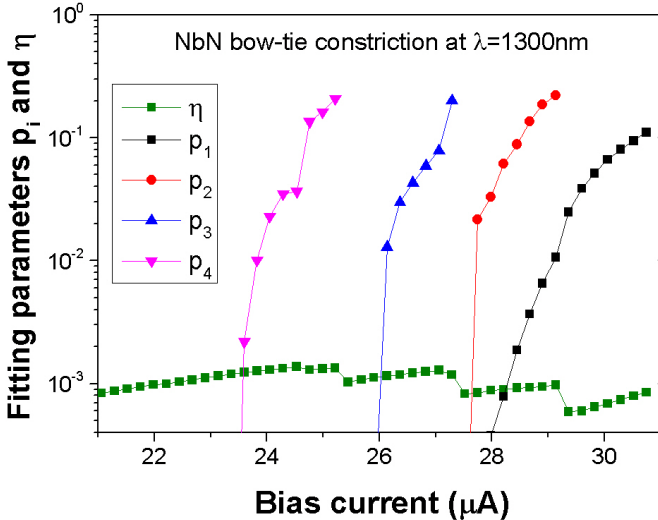

Figure 4.1 The fitting parameters p_i and η calculated for the NbN detector of figure 4.2 are plotted as a function of the bias current I_b for the case of impinging light with wavelength λ=1300nm.

Since the optical response saturates above a certain number of impinging photons i_{max}, we consider the probability $p_j=1$ when j>i_{max}. Therefore we restrict the set of parameters to $\{\eta, p_0, p_1, ..., p_{imax}\}$. By following the previous protocol for different bias currents and impinging powers we can achieve the values of p_i as a function of I_b. The result of modified detector tomography is shown in the figure 4.1 [86] where the p_i parameters and η are plotted as a function of bias current for a NbN bow-tie SSPD. The complete description of the detector is achieved: we know, as a function of I_b, the probability that the detection is triggered by one photon (p_1), two photons (p_2), three photons (p_3) and so on until i_{max} number of photons. In addition, the tomography protocol provides the value of the linear efficiency η and proves its independence from the bias current. The assumption-free feature makes this method a powerful tool to shed light on topics that are still subject of debate, such as the nature of the detection mechanism and the dimension of the hot spot in SSPDs.

4.2 Detection mechanism in NbN nanowire SSPDs

4.2.1 Introduction

After the first demonstration of NbN superconducting single photon detectors in 2001 [14] these devices found a broad range of applications due to the improved understanding of the working principle and the development of their performance[1, 3, 4]. However, despite the theoretical and technological efforts, numerous open questions are still waiting for an answer.

In this section[1] we deal with two major open issues. The first regards the nanoscale mechanisms which lead to a detection event after a photon absorption. It is still subject of debate whether or not the detection event is caused by a resistive area, as suggested by the normal-core hot spot model [54]. Indeed, it could be the weakening of superconductivity alone to trigger a detection event as predicted by the diffusion-based hot spot model [55]. Moreover, although theoretical studies suggest the possibility that vortices could have a role in the detection process [41, 42, 56], no unambiguous experimental proof of their contribution was reported so far. The second issue to be addressed regards the dependence of the SSPD optical response on the measurement temperature. Since the superconducting gap decreases for increasing temperature, one would expect that, for a given photon energy, the device would behave more efficiently at temperatures slightly lower than the critical value, T_c. Instead, experimental observations prove that an SSPD detects more efficiently at low

---

[1]This section is based on J.J.Renema, R.Gaudio *et al*. *Phys.Rev.Lett*. **112** 117604 (2014). The devices were fabricated by the author of this thesis, while the QDT measurements were performed mainly by Dr. Jelmer J. Renema at Leiden University [87].

temperatures [32] rather than at temperatures close to T_c. These experimental results reveal the need for a deeper understanding of the SSPDs detection mechanism.

In order to address the first open question is convenient to recall from chapter 1 that the functional relation between the total energy E_t impinging on the detector and the bias current I_b^{th} needed to trigger a detection with a given probability is different in the two detection models. Indeed if the detection event is caused by the formation of a resistive area, I_b^{th} will vary as the square root of E_t, while, if the resistive area formation is not necessary to trigger a detection, I_b^{th} will be proportional to E_t. Therefore, expressing the relation between E_t and I_b^{th} over a sufficiently large range of impinging energies, corresponds to identifying the mechanism dominating the detection process.

Modified quantum detector tomography, which provides an assumption-free description of the detector and separates the linear loss from the non-linear optical response, is the proper tool to investigate the detection mechanisms in nanowire SSPDs. Indeed it allows to explore the detector behaviour for a broad range of impinging energies by exploiting the multiphoton detection. In this way, it is possible to explore the detector response without varying λ over a large range of wavelengths and, thus, avoiding variations in the transmission of the experimental set-up.

4.2.2 Experiment

The pattern of an SSPD usually follows a meandering geometry [14]. Although such design improves the device coupling with the illuminating light spot, it reduces the chance for a multiphoton detection event. If, for example, the SSPD is biased with a I_b low enough to allow a detection only when two or more photons are absorbed, the probability for such an event is reduced drastically due to the large active area of the meander SSPD. In this case, indeed, the simultaneous absorption is not enough to ensure a detection: the two photons should also be absorbed close to each other. In order to enhance the multiphoton detector behaviour, we decided to carry on the experiment on a simple detector: a bow-tie constriction [64]. In this case, the small and well defined active area of the bow-tie constriction ensures that if three photons are absorbed simultaneously, they will also be absorbed close to each other. The bow-tie detector (Figure 4.2) was patterned from a 5nm thick NbN film characterized by the critical temperature T_c=9.7K. The patterning process has been optimized to obtain an active area consisting of a short wire of nominal length L=0nm and width w=220nm.

The detector, kept at a constant temperature of 3.2K during the experiment, showed a critical current I_c=44µA. The active area was illuminated with a Fianium broadband supercontinuum laser with a specified pulse duration of 7ps and repetition rate of 20MHz.
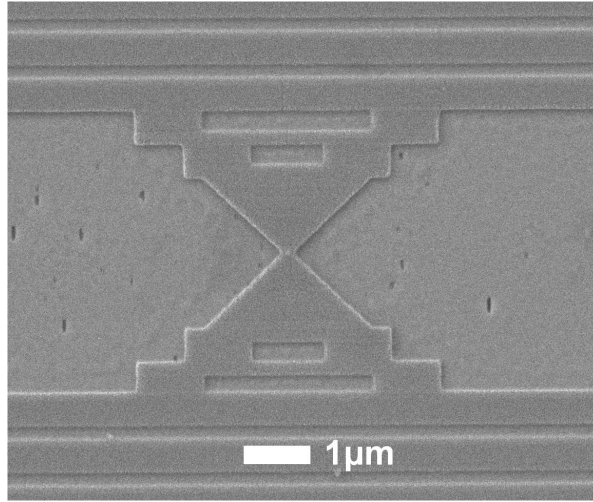
Figure 4.2 SEM micrograph of a bow-tie SSPD similar to that investigated in this section. The active area, nominally 0nm long and 220nm wide, is the constriction appearing at the centre of the image.

During the tomography experiment the laser beam was spectrally filtered to select 12 different wavelengths ranging from 460nm to 1650nm. For each wavelength λ, the laser power P was varied and for each step of the sweep the counts C were recorded while varying the bias current. Thus, the data set acquired during the entire experiment was $C(\lambda, I_b, P)$.

4.2.3 Results and discussion

The implementation of the tomography protocol to the data acquired for 12 different wavelengths provides us with the values of η and p_i plotted as a function of I_b (as in figure 4.1). From each of these 12 graphs, we record the value of I_b for which the value of p_i is equal to 0.01. This is the bias current needed to have a detection event with 0.01 probability when i photons with wavelength λ and, thus, with total energy $E_t = ihc/\lambda$ impinge on the detector. Plotting these I_b values (normalized to the I_c) as a function of the impinging energy E_t, leads us to the graph in figure 4.3. This graph reveals the detector optical response for impinging energies that span over almost 8eV. Such broad exploration of the detector behaviour is made possible by the multiphoton response. For example, resolving the contribution of 4 impinging photons of λ=600nm via the tomography protocol means gaining information on how the detector behaves when 8eV are absorbed in the active area.
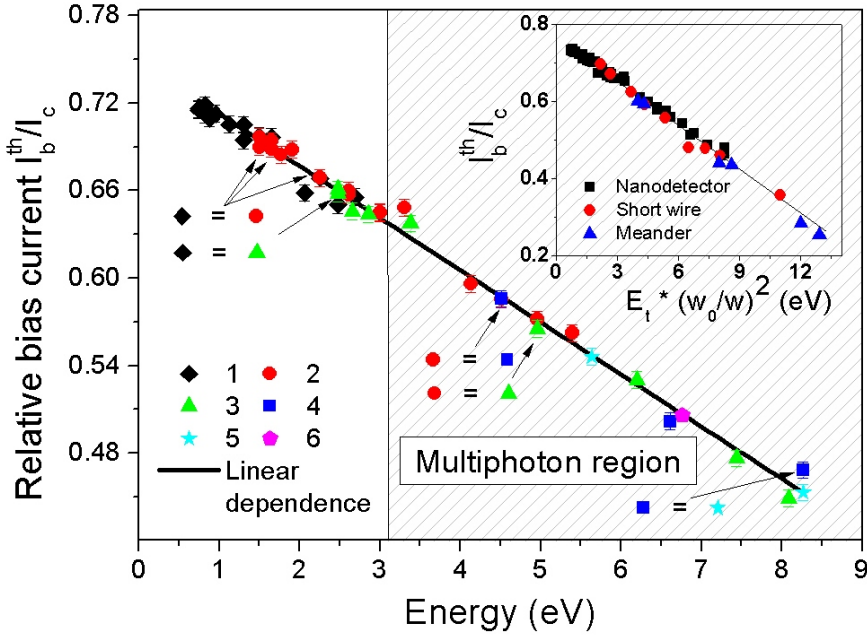
Figure 4.3 The normalized bias currents needed to trigger a detection with probability of 0.01 are reported as a function of impinging energy. The different colours and symbols correspond to detection events triggered by different number of photons. The arrows indicate overlapping experimental data points and the black line, whose slope is γ, shows the interchange between I_b^{th} and E_t. *Inset*: The tomography procedure is applied to two extra detectors: a nanowire SSPD (l=200nm) and a meander SSPD. The results are compared to the data in the main figure. The different width of the three detectors was taken in account by normalizing to the width w_0 of the bow-tie detector.

The data points that in figure 4.3 are evidenced by black arrows, belong to data sets acquired for wavelengths multiple of a certain wavelength, like for example 500nm, 1000nm and 1500nm. Points given by 2 photons at 1000nm and 3 photons at 1500nm overlap with the point corresponding to 1 photon at 500nm. The superposition of such data points, which recurs over the entire range of E_t, proves that the detector response does not depend on the photon wavelength but only on a combination of I_b^{th} and E_t [88]. The data points reported in figure 4.3 show that the bias current needed to trigger a detection event with probability equal to 0.01 depends linearly on the total impinging energy E_t. The linear dependence suggests that the detection is triggered by the weakening of superconductivity due to the depletion of Cooper pairs. Therefore, since the normal-core hot spot model would lead to a quadratic dependence of I_b^{th} on E_t, we can exclude that the detection event is triggered by the appearance of a resistive area. It is important to mention that the dependence showed in figure 4.3 remains linear also for different threshold criterion: the I_b^{th} values needed to trigger a detection with probabilities 0.1 or 0.001, for example, still depend linearly on E_t.

In order to prove that the previous result applies also to the meander SSPD, we performed the tomography experiment on two additional detectors: a NbN short wire SSPD (width w=150nm and length l=200nm) and on a NbN meander SSPD (w=100nm and l=105μm). The difference in wire width was taken in account through the normalization of the energy scale by the width w_0 of the bow-tie constriction[53]. The results are reported in the inset of figure 4.3 and reveal that the behaviour of the three different detectors superimpose. Therefore, the bow-tie detector can be considered as a model to investigate the behaviour of the conventional meander SSPD.

To strengthen our experimental result, we implemented the tomography protocol with more accuracy by focusing only on the wavelength λ=600nm. The experimental results are reported in figure 4.4 and show the detector response to i=1,..,4 impinging photons with an accuracy of 50nA.

The data points were fitted by the following curve $I_b = I_o - \gamma E_t^{\alpha}$, where γ is the curve slope and describes the interchange between I_b^{th} and E_t and the parameter α determines which detection model describes best the behaviour of the NbN bow-tie detector. As mentioned in chapter 1, the normal-core hot spot model predicts α=0.5 while the diffusion-based hot spot model leads to α=1 [53–55]. The χ^2 per degree of freedom, which is reported in the inset of figure 4.4, reveals that the best fit is obtained with α=1.00 ±0.06 and confirms that the diffusion of quasi-particles dominates the detection mechanism in NbN SSPDs.
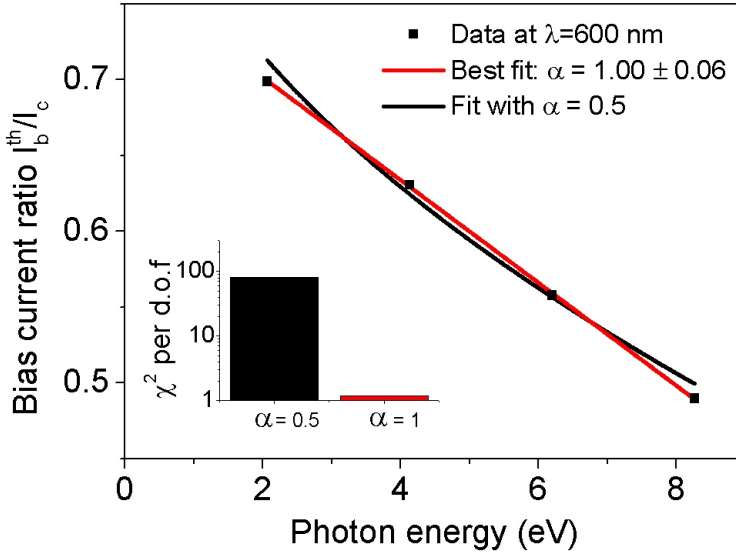
Figure 4.4 The experimental tomography results for λ=600nm and the two fitting curves, which differ for the parameter α, are shown. *Inset*: The computed χ^2 per degree of freedom reveals that the best fit is obtained with α=1.00±0.06.

In both figures 4.3 and 4.4, the extrapolation of the linear fitting to E_t=0eV leads to a value of current, I_0, for which there should be a detection event with 0.01 probability due to an impinging energy equal to zero. The fact that this "reference current" $I_0 \sim 0.78 I_c$ is different from I_c is surprising. Since no detection event is registered in absence of light when the detector is biased with the current I_0, the extrapolated detection probability of 0.01 at I_b^{th}=I_o cannot be related to dark counts. We conclude that the linear current-energy relation does not hold for energies $\ll$2eV. To gain more insight in our experimental results we implemented the tomographic protocol at temperatures ranging from 3.2K to 6.5K. At each temperature we determine the values of I_0, I_c and γ. The lower inset of figure 4.5 shows how I_0 and I_c vary with increasing temperature. The value of I_0 exceeds the critical current for temperatures higher than 5.5K. This means that at these temperatures there will be a range of impinging energies for which it is not possible to achieve the maximum efficiency. This observation explains why the performance of a NbN SSPD degrades at temperatures higher than 5.5K [32].

In addition, since γ is independent of temperature, as the upper inset of figure 4.5 reveals, the variation of NbN SSPD performance with temperature should be related to how I_0 varies with T. The lower inset in figure 4.5 shows that while I_c follows the behaviour predicted

by the Ginzburg Landau theory, the I_0 has a different behaviour. Since magnetic vortices play a major role in the physics of type-II superconductors like NbN, it is legitimate to wonder whether the I_0 temperature dependence is related to vortices. Theoretical studies [33, 41, 42, 56] suggest that the vortices assist or induce a detection. Indeed, if a vortex enters the wire it will be dragged from one edge to the other under the action of the Lorentz force. During such wire crossing, the vortex dissipates energy, contributing to the detection event. Vortices can appear in the superconducting wire because of vortex-antivortex pair (VAP) unbinding or because the barrier for vortex entry is lowered.
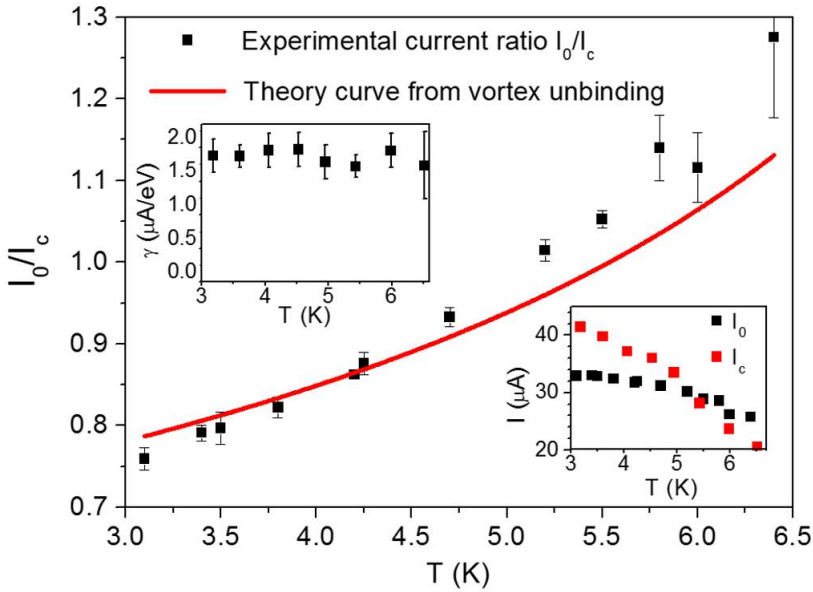
Figure 4.5 The ratio I_0/I_c is plotted as a function of experimental temperature T. The red curve shows the theoretical trend from the vortex unbinding model. *Top inset*: The conversion factor γ is plotted as a function of temperature. *Bottom inset*: The experimental values of I_0 and I_c, which are displayed as a function of temperature, reveal that when T>5.5K the reference current I_0 is higher than I_c.

According to the recent works [41, 42] the vortex entry, which is proven to be more favourable compared to the VAP unbinding, takes place when the bias current reaches a threshold value $\tilde{I}_0$. Therefore, for $I_b^{th} > \tilde{I}_0$, vortices can enter and, thus, cross the superconducting wire. In order to test whether the vortices are related to the behaviour of I_0, we compare the temperature dependence of I_0 to that of $\tilde{I}_0$. The figure 4.5 shows the experimental

values of I_0/I_c plotted as a function of temperature and the ratio between $\tilde{I}_0$ and the critical current calculated according to the Ginzburg Landau theory. The agreement between the experimental and theoretical temperature dependence suggests that the vortices play a role in the detection mechanism and therefore the scenario that best describes detection mechanism in NbN SSPDs is that depicted in panel d of figure 1.5.

4.3   Hot spot dimension in NbN nanowire SSPDs

4.3.1   Introduction

A fundamental and interesting question that still waits for an answer regards the dimensions of the hot spot [2]. Answering to such question could allow the design of detectors with enhanced single and multiphoton detection. Already several works [89, 90] estimated the dimension of the hot spot in NbN SSPDs assuming that a resistive cylinder appears upon photon absorption. As proved in the previous section 4.2, the possibility that a normal-core hot spot is formed after absorption is to be excluded. Therefore, previous estimations do not provide answer to the question.

In order to address this issue, we pursued a different approach [3]. Let us consider a meander SSPD that is biased with such a low I_b that only the energy carried by two photons is enough to trigger a detection. In this condition there are two necessary requirements for the detection to take place. The two photons should be absorbed simultaneously, or more precisely, within the hot spot relaxation time, i.e. tens of ps [91]. The second requirement pertains to the distance between the two absorption sites. Indeed, the two photons will jointly produce a detection event only if the absorption sites fall within a certain distance d_{max}. If we assume that the two-photon detection is triggered when the two hot spots overlap as shown in panel a of figure 4.6, we expect d_{max} to be of the order of the hot spot dimension. The measurement of d_{max} therefore provides information about the hot spot dimension.

---

2 We refere here to the hot spot as the superconducting area perturbed by the absorption of a photon and not to a resistive cylinder. We retain the terminology "hot spot" for consistency with previous work.

3 Regarding the results presented in the section 4.3, the devices were fabricated by the author of this thesis and the experiments were performed jointly by the author and by Dr. J.J. Renema [87].
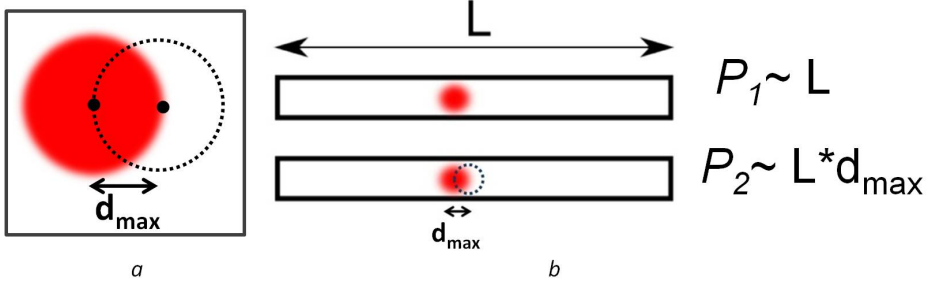
Figure 4.6 Panel *a* sketches the spatial requirement for the two-photon detection event. The second photon, whose hot spot is depicted by a dashed circle, should absorbed within d_{max} from the first hot spot (red disc). Panel *b* depicts the absorption of two photons in a nanowire of length *L*.

Let us consider a nanowire SSPD with length *L* and call P_1 the absorption probability for an impinging photon. If the illumination spot covers the entire wire, P_1 will be proportional to the wire length *L* (see figure 4.6). In order to trigger a detection, the second photon should be absorbed within a distance d_{max} from the absorption site of the first photon. The probability that a second photon is absorbed and contributes to the two-photon detection event is proportional to d_{max}. Therefore the probability P_2 of absorbing two useful photons is proportional to the product of *L* and d_{max}. Thus, we can write

$$\frac{P_1^2}{P_2} = \frac{L}{d_{max}} \tag{4.3}$$

Since the length *L* of the nanowire is known, the value of d_{max} can be estimated by comparing the absorption probability for one and two photons, P_1 and P_2. In this section we use detector tomography to extract the values of P_1 and P_2 and therefore d_{max}.

4.3.2 Experiment

The absorption probability P_1 in equation 4.3 corresponds to the parameter η (section 4.1) for the case in which the detector responds mainly to one photon. We will refer to this probability as η_1. The probability P_2, instead, is the probability for two photons to be absorbed and jointly contribute to a two-photon detection event. Hence, $\sqrt{P_2}$ coincides with η_2, the probability for one photon to contribute in a two-photon detection event. Therefore, the implementation of the tomographic protocol on a wire of length *L* allows us to estimate the dimension of the hot spot. To strengthen the experimental results we implemented the tomography protocol on four nanowire SSPDs characterized by different lengths *L*. Since it

is important for the validity of the experiment that the only difference between the nanowire detectors is their length, we took special care in the fabrication process. The nanowires were patterned from a NbN 5nm thick film. The NbN film was deposited on a GaAs(001) substrate at the ambient temperature of $400\,^{o}$C and showed a critical temperature of 9.6K. The electron-beam lithographic step was optimized to produce 64 nanowire SSPDs with identical width w=150nm and lengths L= 0, 100, 200 and 400nm. The extensive observation of the device through scanning electron microscopy ensured a defect-free fabrication. The identical width, however, does not exclude that nanowires of different length could be affected by inhomogeneities [92] as discussed in chapter 3 of this thesis. Since the critical current of a perfect nanowire does not depend on its length L, the I_c values of homogeneous wires with different L should be the same. For this reason, before implementing the tomography, we performed an extensive pre-characterization of the 64 devices with the aim of locating 4 nanowires showing similar critical currents. The pre-characterization was carried out at 4.2K in a probe station that allowed a fast electrical testing. The tomography experiment was performed at 3.2K on four nanowires whose critical current was between 27.4μA and 27.9μA. This is sufficiently close to the maximum I_c observed in the batch (27.9μA) that the effect of inhomogeneity is expected to be negligible.

The experiment consisted in acquiring the optical response of the detectors while varying I_b and impinging light power. In order to ensure the simultaneous absorption of two photons the detectors were illuminated with a Coherent Vitesse laser (λ=800nm) whose pulse duration is specified to be 100fs, much shorter than the hot spot relaxation time [91]. To ensure that the absorption efficiency η is uniform in the whole nanowire active area, the beam spot dimension was chosen to be 200μm, much bigger than the active area. In addition, the laser beam was polarized and the polarization axis, which was kept constant during the entire experiment, was chosen to maximize the detector optical response.

4.3.3   Results and discussion

In figure 4.7 we report the result of the tomography protocol applied to the nanowire of length L=100nm. The graph shows the detection probabilities for one and two-photon detection, p_1 and p_2. These two curves indicate in which range of bias current the nanowire behaves fully as single-photon detector and two-photon detector. For example, for 19μA$<I_b<$24μA the detector mostly responds to one photon while for 16μA$<I_b<$19μA it mainly responds to two photons absorbed together. Moreover, the graph shows the absorption efficiencies η_1 (or P_1) and η_2 (or $\sqrt{P_2}$) for one and two-photon detection respectively. It is important to notice that these latter vary with the bias current. Indeed, the pink and blue curves in figure 4.7

are lower for low I_b when the detector responds to two or more photons and this feature is evidence for the finite hot spot dimension.
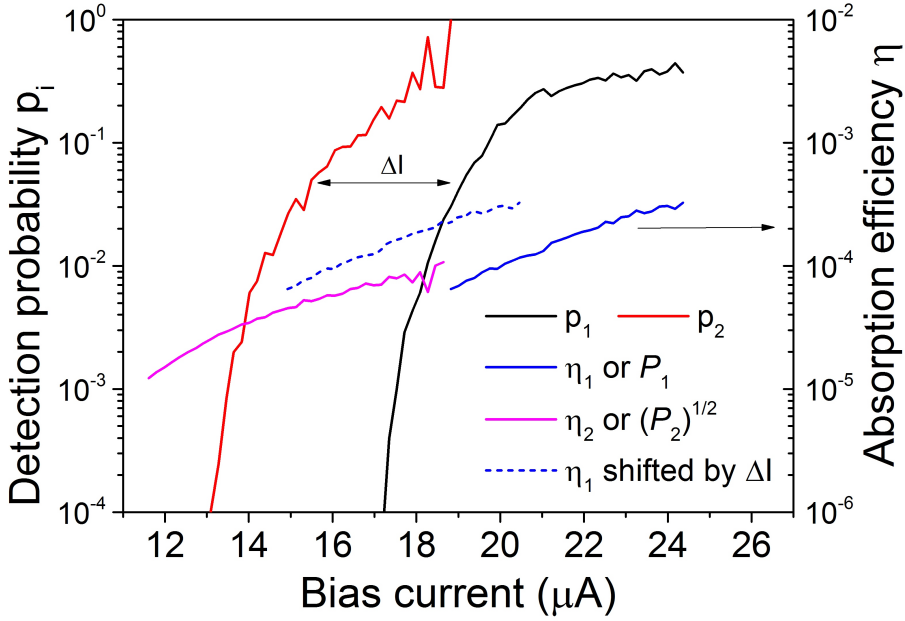

Figure 4.7 The detection probabilities p_i and the absorption efficiencies for one photon (η_1) and two-photon (η_2) detection are plotted as a function of bias current. The blue dashed lines corresponds to η_1 shifted by ΔI.

For each wire length L, the ratio in the left-hand-side of equation 4.3 is estimated by comparing values of η_1 and η_2 at bias currents that correspond to similar detection probabilities or, in other words, we compare $\eta_1(I_{b1})$ to $\eta_2(I_{b2})$ for which $p_1(I_{b1}) = p_2(I_{b2})$. An equivalent way to perform the comparison is noticing that the one and two photon regimes are separated by the quantity ΔI. Therefore, the comparison between the squared values of P_1 shifted by the same ΔI (blue dashed curve) and the values of P_2 provides an estimation of the left-hand-side of equation 4.3. By applying such procedure to the four different lengths L, we obtain the graph in figure 4.8 where the ratio P_2/P_1^2 for the four nanowires is plotted as a function of the detection probability p. The first feature to notice is that the four curves differ from each other for low detection probabilities, while for high values of detection probabilities the four curves converge and the value of P_2/P_1^2 is independent from p. We explain this feature of the data by noticing that for low detection probabilities, when the bias

current is lower, the device is not working fully in one-photon regime or in the two-photon regime and, therefore, the reasoning expressed in figure 4.6 is not applicable.
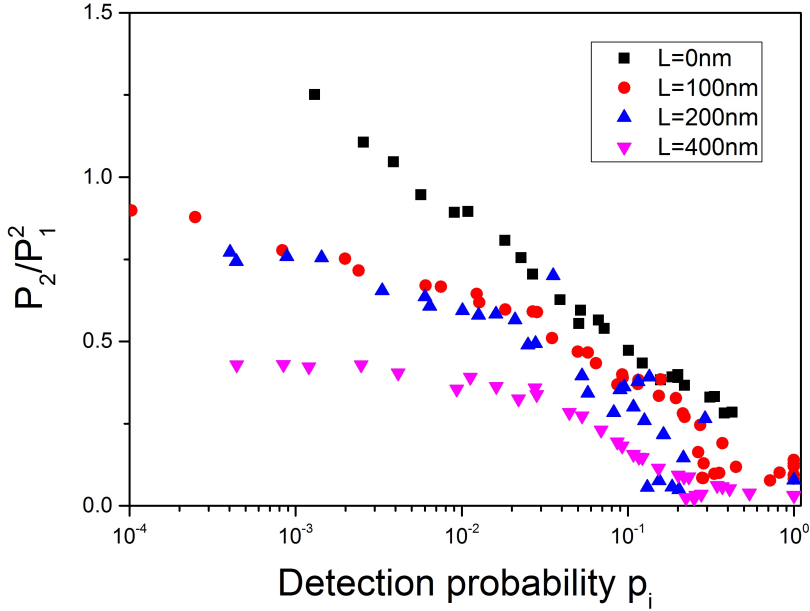

Figure 4.8 The values of P_2/P_1^2, which were estimated for the four nanowires, are plotted as a function of detection probability p. For $0.4 < p < 1$ the value of P_2/P_1^2, proportional to d_{max}, appears to be independent of p.

The observations drawn from figure 4.8 encourage us to consider the values of P_1^2/P_2 obtained at high p as characteristic of the nanowire. In figure 4.9 we plot, as a function of the nanowire length L, the average value of P_1^2/P_2 obtained from the interval of detection probabilities $0.1 < p < 1$.

As expected, the experimental values of P_1^2/P_2 reported in figure 4.9 increase with increasing L. This trend is explained by the equation 4.3, where the ratio P_1^2/P_2 is shown to be proportional to L. The experimental data is fitted according to equation 4.3 and the result of the fit is the red curve displayed in the graph of figure 4.9. From the slope of this curve we estimate d_{max}=14±5nm. It is important to notice that such fit does not describe the behaviour of our system when the nominal length of the nanowire is 0nm. The small dimension of the detectors under investigation encouraged us to consider the contribution that the tapers could give to the detection process. As mentioned in chapter 2, the active area of the detector

is connected to a meander that provides an additional kinetic inductance. The connection consists of a 45° tapering that, by gradually funnelling the supercurrent into the narrow wire, reduces current crowding.
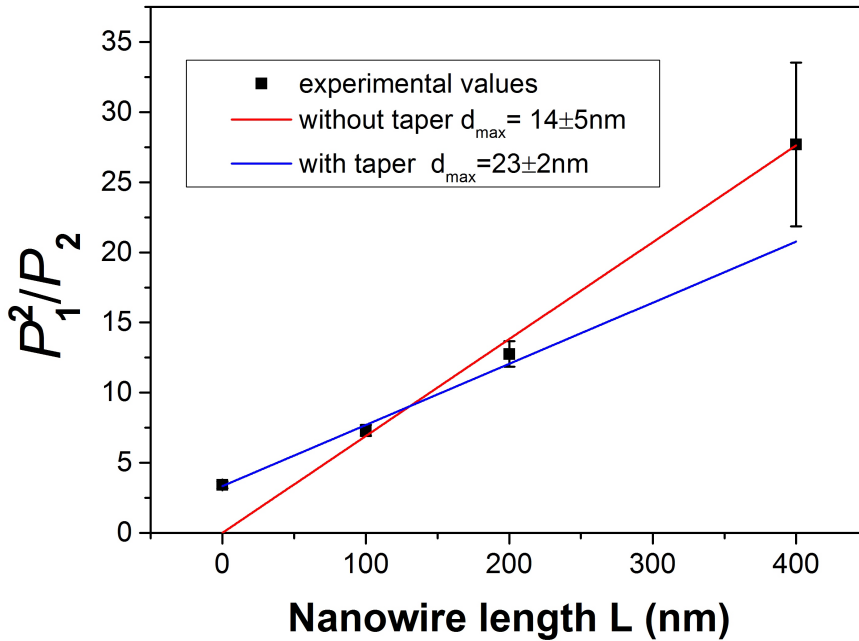
Figure 4.9 The experimental average values of P_1^2/P_2 obtained for $0.1 < p < 1$ are reported as a function of nanowire length L. The red and blue curves result from fitting the data with the equation 4.3. A better fit is achieved by assuming that an extra length, l_{taper}, contributes to the detection process.

When the detector is biased close to its I_c (and thus $0.1<p<1$) also the narrowest part of the tapering, which is the closest to the active area, is biased close to its I_c. Therefore, it is legitimate to assume that part of the tapering behaves as active area. For this reason we fitted the experimental data considering the length of the active area as $L+l_{taper}$. The blue curve in figure 4.9 is the best fit obtained considering $\sim$73nm of the tapered section as active ($\sim$36nm on each side of the active area). This last fit provides a value of $d_{max}=23\pm2$nm. According to our present understanding of the two-photon detection process, as resulting from the physical overlap between two hot-spots, this also provides an estimate of the hot spot dimension at the time when the detection probability is maximum.

4.4   Conclusion

In conclusion, we found an answer to two important open questions. The implementation of modified quantum detector tomography on a bow-tie constriction revealed that the detection mechanism in NbN SSPDs is based on vortices and quasi-particle diffusion. This result allows us to consider the scenario presented in panel d of figure 1.5 as the most probable detection mechanism in NbN based SSPDs. In addition, studying the detector behaviour as a function of temperature it was possible to explain why the detector performance degrades for temperatures higher than 5.5K.

The second answer provided in this chapter is an estimation of the hot spot dimension in NbN SSPDs. Such result has been achieved by focusing the attention on the maximum distance, d_{max}, between two hot spots for a two-photon detection event. We experimentally determined the value of d_{max} by comparing the absorption efficiencies for one and two-photon detection. These latter probabilities were estimated through the implementation of modified detector tomography. To strengthen our results, we repeated the tomography protocol on four nanowire SSPDs differing only for their length L. By taking in account that the tapered sections partially contribute the detection process, the experiment revealed that the typical hot spot dimension in NbN SSPDs is of the order of 20nm.

Chapter 5

Detection mechanism in WSi nanowire SSPDs

5.1 Introduction

Superconducting single photon detectors (SSPDs) [14] constitute a key technology for the development of quantum communication and computation [93]. The fast response time, combined with the low dark count rate, small jitter and single and multiphoton counting capability [3] favoured the use of this technology in applications of Quantum Key Distribution (QKD) [62], quantum optics [65], nanoscale imaging [64] and interplanetary optical communications [9]. Since the first SSPD demonstration, different polycrystalline superconducting films, such as NbN, NbTiN, TaN were employed and different techniques were developed in order to improve the photon absorption [1, 3, 4]. However, despite the technological efforts to improve the device performance, these detectors are still affected by low fabrication yield [50, 51, 92] and the highest system detection efficiency (SDE) reported for λ=1550nm is not higher than 60% [27]. Since 2013 [34, 36, 61], SSPD patterned from thin amorphous superconducting films caught the attention of the SSPD community. Although operating at much lower temperatures, SSPDs based on amorphous WSi, MoSi [38] and MoGe [37] revealed to be promising not only for their robustness with respect to fabrication defects and inhomogenenities, but also for the system detection efficiency that saturates close to unity [22] already for bias currents well below I_c, which makes them less sensitive to fabrication defects and inhomogeneities. The physical reason for such difference between the performance of amorphous and polycrystalline SSPDs can be sought in the material

characteristics and in the nanoscale detection mechanisms. With respect to NbN, WSi is characterized by a higher normal state diffusion coefficient, a larger coherence length and a much lower superconducting gap [33, 35]. Recent theoretical results [33] suggest that the detection mechanism in WSi SSPDs is different from that taking place in NbN SSPDs. While in NbN SSPDs photon absorption creates a region with a non-equilibrium concentration of quasi-particles (but not completely resistive), as shown in Chapter 4, in WSi the theoretical simulations suggest that the photon absorption creates a resistive hotspot area [33, 54].

The lack of experimental evidence that unequivocally describes the detection process in amorphous SSPDs, motivated our experimental research. To experimentally determine which is the dominant detection mechanism in WSi based SSPDs, we rely on the relation between the total energy (E_t) impinging on the detector and the bias current (I_b^{th}) needed to obtain a detection event with a constant probability. As discussed in chapter 1 and 4, in the original hot spot model [54], a resistive hot spot forms and the detection is triggered when the supercurrent density in the remaining superconducting walkways reaches the critical current density. The width of the walkway is determined by the diameter of the hotspot and, since the area of the latter depends directly on E_t, for a given detection probability I_b^{th} is proportional to the square root of E_t. In other models, which take into account quasi-particle diffusion [33, 55], the superconductivity is weakened by the reduction of superconducting carriers and a linear current-energy relation is predicted. The linear current-energy relation was indeed experimentally verified in our previous study of NbN nanowires (see Chapter 4).
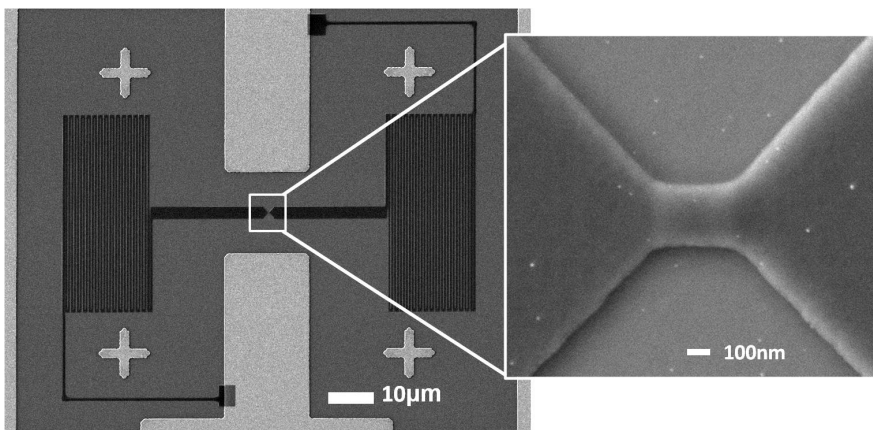

Figure 5.1 SEM micrograph of a WSi nanowire SSPD similar to that examined in this chapter. The inset shows the magnification of the active area.

In order to obtain the relation between I_b^{th} and E_t for different detection probabilities, the response of the WSi nanowire SSPD is characterized via modified quantum detector tomography (QDT) described in Chapter 4 [86]. The QDT technique not only separates the linear response (photon absorption probability) from the non linear contributions, but also distinguishes the different contributions allowing us to derive, for given E_t and I_b^{th}, the probability that the detector responds to one or more photons.

In addition, to plot I_b^{th} as a function of E_t over a broad range of impinging energies we maximize the probability of multiphoton detection by realizing a WSi nanowire SSPD with a small active area. The SEM micrograph of a WSi nanowire similar to that examined in this chapter is reported in figure 5.1.

5.2   Experiment

The WSi 5nm-thick film was deposited at NIST (Boulder CO, USA) by V.B. Verma, A.E. Lita, J. Shainline, M. J. Stevens, R.P. Mirin and S.W. Nam. The deposition was performed at room temperature, on a commercial GaAs(001) wafer by co-sputtering of W and Si targets [34, 61]. The thin film, characterized by a critical temperature (T_c) of $\sim$3.2K, is then protected against oxidation by a $\sim$1nm thick a-Si capping layer. The electrical contacts, made of 14nm Ti and 140nm Au layers, are defined by optical lithography and lift off. In the last phase of fabrication, the nanowire is defined via electron-beam lithography (EBL) and patterned via reactive-ion etching in Ar/SF$_6$ plasma. The device design and the EBL exposure were optimized to obtain a nanowire of 250nm width and 250nm length. The nanowire width was chosen to be larger than the typical width used for NbN nanodetectors because of the lower current density in WSi. With a larger nanowire width (250nm) it is indeed possible to achieve a higher critical current ($\sim$9µA) and make the experiment more feasible. In order to avoid latching, the nanowire is defined together with an additional meander which provides an extra series inductance [15] of approximately 720nH (figure 5.1). The sample is mounted in a VeriCold cryocooler (see Chapter 2) equipped with a final Joule-Thomson stage where it is kept at a temperature of 1.6K. At this base temperature the WSi nanowire SSPD showed a critical current I_c=9.4µA. During the experiment, the device is biased by a voltage source connected in series with a 10kΩ resistor and the voltage drop across it is measured by a multimeter. The DC port of a bias-T (Minicircuits) connects the source and the resistor to the device, while the RF port is connected to a 50Ω matched counter. Before reaching the counter, the pulses are amplified by a low noise amplifier (MITEQ-AU1263). To avoid signal reflections, a 4dB attenuator is placed between the bias-T and the amplifier. The device is illuminated with a Fianium supercontinuum pulse laser that provides a broadband continuous

spectrum from 600nm to 1800nm with repetition rate 20MHz. For our experiment, the laser beam filtered to select the desired wavelength and is linearly polarized with the aid of a polarizer. To keep the polarization axis constant during the experiment, the polarized light is fed to the device through polarization maintaining components such as single mode optical fibres, a computer controllable digital attenuator and a lensed fibre. This latter is mounted inside the VeriCold cryostat and produces a beam spot with nominal size of 2.9μm at 1550nm. The polarization axis of the light impinging on the detector is perpendicular to the nanowire longitudinal axis. The choice for a linearly polarized beam and for the polarization maintaining components is dictated by the dependence of the internal detection efficiency (IDE) on the polarization axis [79]. Therefore, it is crucial that the polarization axis is kept constant during the experiment.

5.3   Results and discussion

The tomography experiment consists of 11 experimental runs. For each run, a wavelength from the interval 900nm-1650nm is selected with a bandpass dielectric filter (bandwidth of 12nm) and it is sent through the fibre to illuminate the nanowire. Once the wavelength is filtered, we ensure that only the desired wavelength is reaching the detector by spectrally analysing the beam with an optical spectrum analyser (OSA).
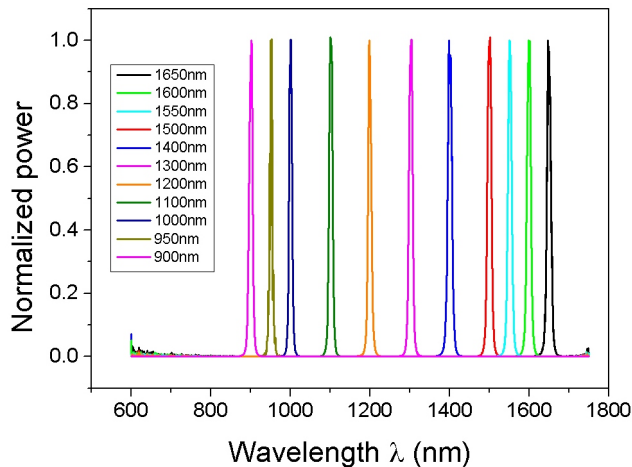

Figure 5.2 The normalized spectrum of the laser beam in the range 600nm-1750nm is reported for each of the 11 filtered wavelengths.

In figure 5.2 we report the normalized spectrum of the laser beam in the spectral range
600nm-1750nm for the 11 filtered wavelengths. During the experimental run, we record the
counts of the detector while varying the light power P and the bias current I_b. In order to
record the power at each attenuation step, we perform a power calibration after each data
acquisition. The 11 data sets are analysed by means of quantum detector tomography. For
each wavelength, the linear absorption efficiency, η, is separated from the non linear response
of the detector and this latter is resolved in such a way that for each pair (I_b, P) we know the
probability that 1 photon triggers a detection (p_1), 2 photons trigger a detection (p_2) and so
on (see paragraph 4.1). As an example, figure 5.3 shows the absorption efficiency η and the
detection probabilities p_1, p_2 and p_3 as a function of I_b for the data set with λ=1650nm.
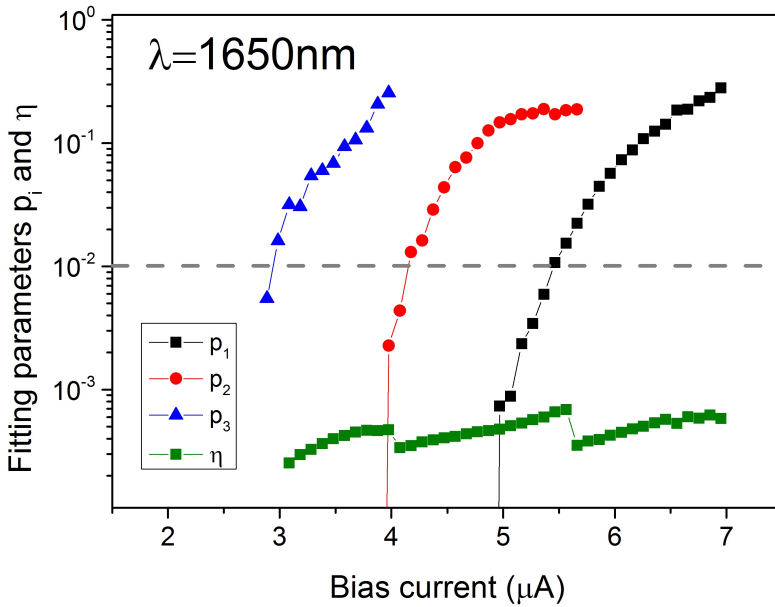
Figure 5.3 The fitting parameters p_i and η computed for the data set acquired at λ=1650nm are
plotted as a function of bias current I_b. The horizontal dashed line corresponds to the detection
probability 0.01.

The graph shows that the probability for i photons to trigger a detection is dependent on
I_b and there is an I_b interval within which i-photon detection is dominant. So, for example,
for $I_b \gtrsim 5.5\mu A$ the device mostly detects single photons, while for $4\mu A \lesssim I_b \lesssim 5.5\mu A$ it
detects mainly pairs of photons and for $I_b \lesssim 4\mu A$ it mainly responds to three photons. In

addition, it is important to notice that η only weakly depends on the bias current. This is in contrast with the findings on NbN nanowires with comparable length (see paragraph 4.3.3) and suggests a larger hot spot dimension in WSi, as expected from the lower energy gap [33].

Once the p_i curves for all the wavelengths are obtained, we can build the graph revealing the relation between I_b and E_t over a wide range of impinging energies. For each wavelength and for each photon regime we record the values of I_b for which the detection probability is equal to 0.01 and we plot it as a function of the total energy impinging on the detector. The total energy, E_t corresponds to the product $i * E_\varphi$, where i is the photon regime and E_φ is the energy carried by one photon. In figure 5.4 we report the data points collected according to this procedure. The data points in figure 5.4 reveal a linear relation between the total impinging energy E_t and the bias current I_b^{th} needed to trigger a detection with 0.01 probability. Such linear relation analogous to that found in NbN nanowires [70] indicates that, for impinging energies in the range 0.75eV - 2.25eV, the normal-core hot spot model [54] cannot describe the detection process in WSi nanowires. In addition, the previous statement does not only refer to the nanowire detector, but it can be also extended to WSi meander SSPDs. Indeed, as proven in the reference [70], the bow-tie constriction as well as the nanowire constitute good representative devices for the meander SSPD. The linear energy dependence that we find experimentally is strengthened by the overlap of two data points highlighted by the red dotted circle in figure 5.4. These two data points pertain to the detection of three photons with wavelength λ=1650nm and two photons with λ=1100nm.

The overlap indicates that the detector response only depends on the total impinging energy E_t or, in other words, it depends on the total amount of photo-created quasi-particles. WSi nanowires therefore respond to the total impinging energy similarly to NbN nanowires. The data points in figure 5.4 can be fitted with the expression $I_b^{th}=I_o$-γE_t [70, 88], where the slope γ (γ=1.66μA/eV) takes in account the interchange between photon energy and bias current and I_o is the intercept of the linear dependence with the y axis (black dashed line in figure 5.4). Similarly to the NbN SSPD case for which I_o=0.75I_c [70], the value of I_o is lower than the critical current value I_c and is equal to 0.70I_c. This would suggest that for impinging energies E_t $\sim$0eV it would be possible to record a detection event with probability 0.01 if the detector was biased with $I_b^{th}=I_o$. Since such detection events are not observed in absence of impinging light, we must conclude that the linear dependence between E_t and I_b^{th} does not remain such for impinging energies E_t <0.75eV.
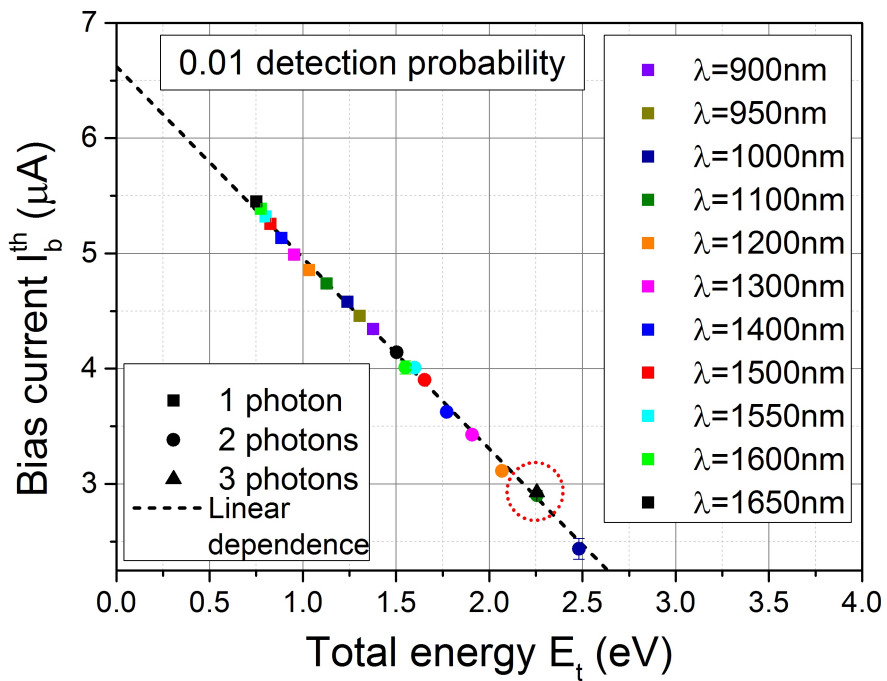
Figure 5.4 The bias current required to trigger a detection with 0.01 probability is plotted as a function of total energy E_t for the 11 wavelengths. The different symbols belong to different detection regimes while each colour corresponds to a wavelength. The red dotted circle highlights the overlap between 2-photon data point for $\lambda=1100$nm and the 3-photon data point for $\lambda=1650$nm. The black dashed line results from a linear fit to the expression $I_b^{th}=I_o-\gamma E_t$.

In order to further validate our experimental results, we focus our attention on one data set to better distinguish between the normal-core and diffusion based hot spot model. In figure 5.5 we report the tomography results for the experimental run acquired at $\lambda=1650$nm. As in the previous figure, here the I_b^{th} values required to obtain a detection event with 0.01 probability are plotted together with the error bars as a function of E_t. The data points are fitted with the expressions $I_b^{th}=I_o-\gamma E_t$ (for the diffusion based hot spot model) and $I_b^{th}=I_o-\gamma E_t^{1/2}$ (for the normal-core hot spot model), where γ and I_o are the free fitting parameters. The two fitting curves are reported in figure 5.5 together with the data. The inset, where we reported the χ^2 per degree of freedom for the two fits, shows that, even though the fit to the diffusion based hot spot model is not excellent ($\chi_{dof}^2 > 1$), it provides a better description of the detection mechanism in WSi SSPDs compared to that offered by the normal-core hot spot model.

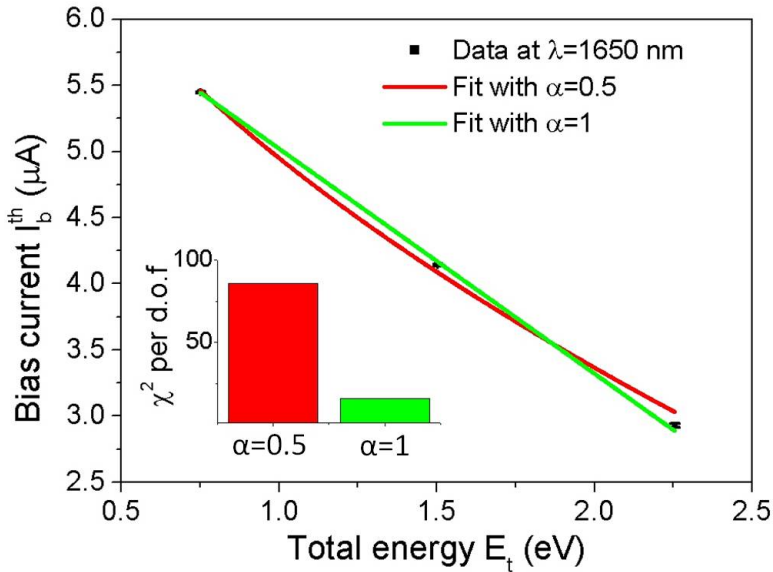**Figure 5.5** The data points and their error bars obtained for the experimental run performed at $\lambda=1650$nm are plotted as a function of total energy E_t. The data are fitted according to the normal-core (red curve) and diffusion based hot spot model (green curve). *Inset*: The computed χ^2 per degree of freedom shows the better agreement between experimental data and the diffusion based model.

An additional fitting of the experimental data in figure 5.4 was carried out with the expression $I_b^{th}=I_o-\gamma E_t^{\alpha}$ with I_o, γ and α free parameters. The best fit is obtained with $\alpha=0.83\pm0.10$, $I_o=7.02\pm0.3\mu A$, $\gamma=2.0\pm0.3\mu A/eV$. Again, we observe that the fitted curve is closer to a linear solution than to a quadratic one.

5.4   Conclusion

We investigated the detection mechanism in WSi based SSPDs by means of modified quantum detector tomography [86]. For this study a short nanowire SSPD was patterned from a WSi thin film and its optical response was recorded for different bias currents, light powers and light wavelengths. By applying the tomographic procedure it was possible to express the functional relation between the bias current needed to trigger a detection with 0.01 probability and the total impinging energy E_t. The functional relation for the impinging energies $0.75eV\leq E_t \leq2.25eV$, revealed to be better described by a linear dependence than by a quadratic one.

According to a recent work [33], the photon absorption in WSi-based SSPDs leads to the formation of a resistive core in the superconducting wire. Such prediction, however, does not imply that the detection in WSi-based SSPDs is described by the normal-core hot spot model. A recent model [94], which assumes the formation of a resistive hot spot in WSi and considers that only quasiparticle recombination play a crucial role in the detection mechanism, predicts a linear relation between energy and bias current.

To conclude, our experimental result does not allow to identify which of the formulated models apply to WSi-based SSPDs, but it constitutes an important experimental test for future theories and models.

Chapter 6

Conclusions and outlook

6.1 Conclusions

Within this thesis work, two main issues, which for a long time were object of debate in the SSPD field, are addressed. The first issue is related to the inhomogeneous critical current of NbN-based SSPDs. The second issue concerns the microscopic processes that lead to a detection event in SSPDs and the comparison between this mechanism in NbN and WSi SSPDs.

The strategy we used to address these two open questions owes its success mainly to two key choices. The first is the choice to investigate nanoscale inhomogeneities and the detection mechanism through a nanodetector [64], i.e. a short wire or a bow-tie constriction. Compared to the standard meander SSPD, such nanodetectors allow a more straightforward data interpretation. The second choice that made our investigation successful consists of the implementation of a technique for the characterization of the detector: the quantum detector tomography (QDT) [86]. This technique allows the exploration of the non-linear detector response over a large range of energies of the impinging photons.

In the following I summarize the main conclusions that can be drawn from the results obtained within this thesis work.

- For the first time, a direct proof of the inhomogeneous nature of the critical current in NbN based SSPDs was achieved. This result was obtained through a systematic study carried out NbN nanowires of equal width but different lengths ranging from 100nm to 15μm. The observation of a systematic decrease of the average critical current with increasing wire length combined with the analysis of the detector optical response, proves the existence of inhomogeneities and reveals that those are not just

isolated constrictions as suggested by previous works [50, 51], but rather that the critical current is continuously varying along the length of the wire. Moreover, the development of a simple microscopic model, allowed us to estimate the upper limit for the length scale of the inhomogeneity. The typical length scale for NbN SSPDs appeared to be $\leq$100nm. The same study, performed on a commercial NbN film deposited on a different substrate, ensured us that the inhomogeneous behavior of I_c is not related to our NbN films only.

- The investigation of the detection mechanism in NbN based SSPDs was made possible by the use of bow-tie constrictions, characterized by a well defined active area, and the implementation of quantum detector tomography. The QDT allowed separating the device linear loss from its non-linear response and resolving the multi-photon response. This investigation resulted in the relation between the total photon energy E_t of the photons impinging on the detector and the bias current I_b^{th} needed for a detection event to happen with a given probability. The relation between I_b^{th} and E_t is found to be linear over almost one order of magnitude in photon energy. Such result proved that the quasi-particle diffusion is involved in the detection process. Moreover, the study of the linear relation between I_b^{th} and E_t as a function of temperature strongly suggests that magnetic vortices play an important role in the detection mechanism.

- Applying QDT on a series of four detectors with different length but similar I_c resulted in the investigation of the hot spot dimension in NbN SSPDs. The estimation of the hot-spot dimension has been achieved through the investigation of a related quantity: the maximum distance between two absorption spots that ensures a two-photon detection. Indeed, when the nanodetector is in the two-photon regime, the detection takes place only if two photons are absorbed simultaneously and close enough to each other. The maximum distance within which the two absorbed photons jointly cause a detection is related to the hot-spot dimension. By comparing the absorption efficiency (η) in the one-photon and two-photon regime for each wire length it is possible to estimate the maximum distance between two absorbed photons that still leads to a two-photon event. This maximum distance is estimated to be $\sim$20nm, which in our interpretation also provides an indication of the dimension of the hot spot.

- The promising performance of WSi based SSPDs [22] raised interesting questions about the mechanisms governing the detection in devices based on amorphous super-conductors with lower energy gap. Theoretical studies [33] predict that the detection mechanism in WSi SSPDs is better described by the normal-core hot spot model [54]. The lack of a direct experimental proof encouraged us to apply QDT technique to

WSi nanowires. The fabrication process was, thus, optimized to successfully realize a nanodetector on such amorphous thin film and the QDT experiment was performed with wavelengths ranging from 900nm to 1650nm. Contrary to theoretical predictions, the experiment reveals that, in the examined energy range, the detection mechanism in WSi SSPDs is similar to that of NbN SSPDs.

6.2 Outlook

The conclusions drawn from this thesis work, as well as latest developments in the field, triggered new interesting questions. Some of those new issues are listed below.

- The results reported in chapter 3 provide direct evidence of the inhomogeneous critical current in NbN SSPDs, offer an estimation of their typical length scale, but can only suggest their origin. Among the possible cause of such inhomogeneities the variation of film thickness was mentioned. I believe that a systematic study of the electro-optical response of nanowires patterned from NbN film of different thickness can contribute to address the question on the origin of inhomogeneities.

- The simple microscopic model reported in chapter 3, which quantitatively describes the detectors electrical behaviour, only qualitatively describes the optical response. The cause of such issue could be related to the choice of the section. It was shown that the typical length scale of the inhomogeneities is ∼20nm and the wire section considered was ∼20nm long and 100nm large. This equals to assume that the critical current density is uniform across the width, which is not justified. The choice for a smaller, maybe squared (20nm×20nm), section could improve the description of the nanodetector optical response.

- In the graph of figure 4.3, which expresses the relation between I_b^{th} and E_t in NbN SSPDs, a linear extrapolation to the zero energy E_t was performed. The discrepancy between the intercept with the y-axis, I_o, and the device critical current may suggest that more caution should be taken in the extrapolation. I think that performing a QDT experiment on a similar device using wavelengths longer than 1700nm would allow us to understand the detection process at lower energies and the connection to the dark count rate. However long wavelengths do not allow the use of fibres, so the experiment should be performed through a free-space optical coupling. This proposal is valid for the WSi SSPD as well. In this case, though, the use of a cryostat with an optical window for the free-space coupling appears challenging since the device operation requires a temperature at least lower than 2.5K [36].

If such experiment is carried out, it would be interesting to study the variation of this I_b^{th}-E_t relation with temperature and compare it with that for higher energies already reported in chapter 4 of this thesis.

- The results of chapter 5, which regard the detection mechanism in WSi based SSPDs, are opposite to the theoretical expectations. Therefore, a refined theoretical description of the system able to predict our experimental results is needed.

Bibliography

[1] R. H. Hadfield. Single-photon detectors for optical quantum information applications. *Nature photonics*, vol. 3, pp. 696, 2009.

[2] M. D. Eisaman, J. Fan, A. Migdall, and S. V. Polyakov. Invited review article: Single-photon sources and detectors. *Review of Scientific Instruments*, vol. 82, pp 071101, 2011.

[3] C. M. Natarajan, M. G. Tanner, and R. H. Hadfield. Superconducting nanowire single-photon detectors: physics and applications. *Superconductor Science and Technology*, vol. 25, pp. 063001, 2012.

[4] E. A. Dauler, M. E. Grein, A. J. Kerman, F. Marsili, S. Miki, S. W. Nam, M. D. Shaw, H. Terai, V. B. Verma, and T. Yamashita. Review of superconducting nanowire single-photon detector system design options and demonstrated performance. *Optical Engineering*, vol. 53, pp. 081907, 2014.

[5] C.H. Bennett and G. Brassard. Quantum cryptography: Public key distribution and coin tossing". In , *Proceedings of IEEE International Conference on Computers, Systems and Signal Processing, Bangalore, India*, page 175, 1984.

[6] N. Gisin, G. Ribordy, W. Tittel, and H. Zbinden. Quantum cryptography. *Rev. Mod. Phys.*, vol. 74, pp. 145, 2002.

[7] C. Zinoni, B. Alloing, L.H. Li, F. Marsili, A. Fiore, L. Lunghi, A. Gerardino, Y. B. Vakhtomin, K.V. Smirnov, and G.N. Gol'tsman. Single-photon experiments at telecommunication wavelengths using nanowire superconducting detectors. *Applied physics letters*, vol. 91, pp. 031106, 2007.

[8] M.D. Shaw, F. Marsili, A. Beyer, J. Stern, G. Resta, P. Ravindran, S. W. Chang, J. Bardin, F. Patawaran, V. Verma, R.P. Mirin, S.W. Nam, and W. Farr. Arrays of WSi superconducting nanowire single photon detectors for deep space optical communications. In *CLEO: Science and Innovations*, pages JTh2A–68. Optical Society of America, 2015.

[9] M.D. Shaw, K. Birnbaum, M. Cheng, M. Srinivasan, K. Quirk, J. Kovalik, A. Biswas, A. D. Beyer, F. Marsili, V. Verma, R.P. Mirin, S.W. Nam, J.A. Stern, and W.H. Farr. A

receiver for the lunar laser communication demonstration using the optical communications telescope laboratory. In *CLEO: Science and Innovations*, pages SM4J–2. Optical Society of America, 2014.

[10] M. Entwistle, M.A. Itzler, J. Chen, M. Owens, K. Patel, X. Jiang, K. Slomkowski, and S. Rangwala. Geiger-mode APD camera system for single-photon 3D LADAR imaging. In *SPIE Defense, Security, and Sensing*, pages 83750D–83750D. International Society for Optics and Photonics, 2012.

[11] S. Somani, S. Kasapi, K. Wilsher, W. Lo, R. Sobolewski, and G.N. Gol'tsman. New photon detector for device analysis: Superconducting single-photon detector based on a hot electron effect. *Journal of Vacuum Science and Technology B*, vol. 19, pp. 2766, 2001.

[12] D. Rosenberg, A. E. Lita, A. J. Miller, and S. W. Nam. Noise-free high-efficiency photon-number-resolving detectors. *Phys. Rev. A*, vol. 71, pp. 061803, 2005.

[13] MIT-Experimental Cosmology and Astrophysics Laboratory website. http://web.mit.edu/figueroagroup/ucal/ucal_tes/. Accessed: 28 Sep 2015.

[14] G.N. Goltsman, O. Okunev, G. Chulkova, A. Lipatov, A. Semenov, K. Smirnov, B. Voronov, A. Dzardanov, C. Williams, and R. Sobolewski. Picosecond superconducting single-photon optical detector. *Applied Physics Letters*, vol. 79, pp.705, 2001.

[15] A. J. Kerman, E. A. Dauler, W. E. Keicher, J. K.W. Yang, K. K. Berggren, G. Goltsman, and B. Voronov. Kinetic-inductance-limited reset time of superconducting nanowire photon counters. *Applied physics letters*, vol. 88, pp. 111116, 2006.

[16] A. J. Kerman, J. K. W. Yang, R. J. Molnar, E. A. Dauler, and K. K. Berggren. Electrothermal feedback in superconducting nanowire single-photon detectors. *Phys. Rev. B*, vol. 79, pp.100509, 2009.

[17] F. Mattioli, Z. Zhou, A. Gaggero, R. Gaudio, S. Jahanmirinejad, D. Sahin, F. Marsili, R. Leoni, and A. Fiore. Photon-number-resolving superconducting nanowire detectors. *Supercond. Sci. Technol.*, vol. 28, pp. 104001, 2015.

[18] Hamamatsu website. http://www.hamamatsu.com. Accessed: 4 Aug 2015.

[19] MPD website. http://www.micro-photon-devices.com/Docs/Datasheet/PDM.pdf. Accessed: 4 Aug 2015.

[20] MPD website. http://www.micro-photon-devices.com/Products/SPAD-by-Wavelength/900nm-1700nm/InGaAs-InP. Accessed: 4 Aug 2015.

[21] A.E. Lita, A.J. Miller, and S.W. Nam. Counting near-infrared single-photons with 95% efficiency. *Opt. Express*, vol. 16, 3032, 2008.

[22] F. Marsili, V.B. Verma, J.A. Stern, S. Harrington, A.E. Lita, T. Gerrits, I. Vayshenker, B. Baek, M.D. Shaw, R.P. Mirin, and S.W. Nam. Detecting single infrared photons with 93% system efficiency. *Nature Photonics*, vol. 7, pp. 210, 2013.

[23] N. Namekata, S. Adachi, and S. Inoue. 1.5 GHz single-photon detection at telecommunication wavelengths using sinusoidally gated InGaAs/InP avalanche photodiode. *Opt. Express*, vol. 17, pp. 6275, 2009.

[24] A. Verevkin, J. Zhang, Roman Sobolewski, A. Lipatov, O. Okunev, G. Chulkova, A. Korneev, K. Smirnov, G. N. Gol'tsman, and A. Semenov. Detection efficiency of large-active-area NbN single-photon superconducting detectors in the ultraviolet to near-infrared range. *Applied Physics Letters*, vol. 80, pp. 4687, 2002.

[25] G.N. Goltsman, K. Smirnov, P. Kouminov, B. Voronov, N. Kaurova, V. Drakinsky, J. Zhang, A. Verevkin, and R. Sobolewski. Fabrication of nanostructured superconducting single-photon detectors. *IEEE Transactions on Applied Superconductivity,*, vol. 13, pp. 192, 2003.

[26] S. Miki, M. Fujiwara, M. Sasaki, W. Zhen, B. Baek, S. W. Nam, A. J. Miller, and R. H. Hadfield. Large sensitive-area nbn nanowire superconducting single-photon detectors fabricated on single-crystal mgo substrates. *Applied Physics Letters*, vol. 92, pp. 061116, 2008.

[27] K. M. Rosfjord, J.K.W. Yang, E.A. Dauler, A. J. Kerman, V. Anant, B. M. Voronov, G. N. Goltsman, and K. K. Berggren. Nanowire single-photon detector with an integrated optical cavity and anti-reflection coating. *Optics Express*, vol. 14, pp. 527, 2006.

[28] A. Gaggero, S Jahanmiri Nejad, F. Marsili, F. Mattioli, R. Leoni, D. Bitauld, D. Sahin, G.J. Hamhuis, R. Nötzel, R. Sanjines, and A. Fiore. Nanowire superconducting single-photon detectors on GaAs for integrated quantum photonic applications. *Applied Physics Letters*, vol. 97, pp. 151108, 2010.

[29] J.P. Sprengers, A. Gaggero, D. Sahin, S. Jahanmirinejad, G. Frucci, F. Mattioli, R. Leoni, J. Beetz, M. Lermer, M. Kamp, S. Höfling, R. Sanjines, and A. Fiore. Waveguide superconducting single-photon detectors for integrated quantum photonic circuits. *Applied Physics Letters*, vol. 99, pp. 181110, 2011.

[30] H. Li, L. Zhang, L. You, X. Yang, W. Zhang, X. Liu, S. Chen, Z. Wang, and X. Xie. Large-sensitive-area superconducting nanowire single-photon detector at 850 nm with high detection efficiency. *Opt. Express*, vol. 23, pp. 17301, 2015.

[31] F. Marsili, F. Najafi, E. Dauler, F. Bellei, X. Hu, M. Csete, R. J. Molnar, and K. K. Berggren. Single-photon detectors based on ultranarrow superconducting nanowires. *Nano letters*, vol. 11, pp. 2048, 2011.

[32] M. Hofherr, D. Rall, K. Ilin, M. Siegel, A. Semenov, H.-W. Hübers, and N. A. Gippius. Intrinsic detection efficiency of superconducting nanowire single-photon detectors with different thicknesses. *J. Appl. Phys.*, vol. 108, pp. 014507, 2010.

[33] A. Engel, J. Lonsky, X. Zhang, and A. Schilling. Detection mechanism in SNSPD: Numerical results of a conceptually simple, yet powerful detection model. *Applied Superconductivity, IEEE Transactions on*, vol. 25, pp. 1-7, 2015.

[34] B. Baek, A. E. Lita, V. Verma, and S. W. Nam. Superconducting aWSi nanowire single-photon detector with saturated internal quantum efficiency from visible to 1850 nm. *Applied Physics Letters*, vol. 98, pp. 251105, 2011.

[35] S. Kondo. Superconducting characteristics and the thermal stability of tungsten-based amorphous thin films. *Journal of Materials Research*, vol. 7, pp.853, 1992.

[36] V.B. Verma, B. Korzh, F. Bussières, R.D. Horansky, A.E. Lita, F. Marsili, M.D. Shaw, H. Zbinden, R.P. Mirin, and S.W. Nam. High-efficiency WSi superconducting nanowire single-photon detectors operating at 2.5 K. *Applied Physics Letters*, vol. 105, pp.122601, 2014.

[37] V.B. Verma, A.E. Lita, M.R. Vissers, F. Marsili, D.P. Pappas, R.P. Mirin, and S. W. Nam. Superconducting nanowire single photon detectors fabricated from an amorphous $Mo_{0.75}Ge_{0.25}$ thin film. *Applied Physics Letters*, vol. 105, pp. 022602, 2014.

[38] Y.P. Korneeva, Y.P. Mikhailov, M.Y.and Pershin, N.N. Manova, A.V. Divochiy, Y.B. Vakhtomin, A.A. Korneev, K.V. Smirnov, A.Y. Sivakov, A.G.and Devizenko, and G.N. Goltsman. Superconducting single-photon detector made of MoSi film. *Supercond. Sci. Technol.*, vol. 27, pp. 095012, 2014.

[39] D. Yu. Vodolazov. Current dependence of the red boundary of superconducting single-photon detectors in the modified hot-spot model. *Phys. Rev. B*, vol. 90, 054515, 2014.

[40] T. Yamashita, S. Miki, K. Makise, W. Qiu, H. Terai, M. Fujiwara, M. Sasaki, and Z. Wang. Origin of intrinsic dark count in superconducting nanowire single-photon detectors. *Applied Physics Letters*, vol. 99, pp. 161105, 2011.

[41] L. N. Bulaevskii, M. J. Graf, C. D. Batista, and V. G. Kogan. Vortex-induced dissipation in narrow current-biased thin-film superconducting strips. *Physical Review B*, vol. 83, pp.144526, 2011.

[42] L. N. Bulaevskii, M. J. Graf, and V. G. Kogan. Vortex-assisted photon counts and their magnetic field dependence in single-photon superconducting detectors. *Physical Review B*, vol. 85, pp.014505, 2012.

[43] H. Bartolf, A. Engel, A. Schilling, K. Il'in, M. Siegel, H.-W. Hübers, and A. Semenov. Current-assisted thermally activated flux liberation in ultrathin nanopatterned nbn superconducting meander structures. *Physical Review B*, vol 81, pp. 024502, 2010.

[44] J. R. Clem and K. K. Berggren. Geometry-dependent critical currents in superconducting nanocircuits. *Phys. Rev. B*, vol. 84, pp. 174510, 2011.

[45] D. Henrich, P. Reichensperger, M. Hofherr, J. M. Meckbach, K. Il'in, M. Siegel, A. Semenov, A. Zotova, and D. Yu. Vodolazov. Geometry-induced reduction of the critical current in superconducting nanowires. *Phys. Rev. B*, vol. 86, pp. 144504, 2012.

[46] M.K. Akhlaghi, H. Atikian, A. Eftekharian, M. Loncar, and A.H. Majedi. Reduced dark counts in optimized geometries for superconducting nanowire single photon detectors. *Opt. Express*, vol. 20, p.23610, 2012.

[47] H. Shibata, K. Shimizu, H.i Takesue, and Y. Tokura. Ultimate low system dark count rate for superconducting nanowire single-photon detector. *arXiv preprint arXiv:1507.01743*, 2015.

[48] D. Henrich, S. Dörner, M. Hofherr, K. Ilin, A. Semenov, E. Heintze, M. Scheffler, M. Dressel, and M. Siegel. Broadening of hot-spot response spectrum of superconducting NbN nanowire single-photon detector with reduced nitrogen content. *Journal of Applied Physics*, vol. 112, pp. 074511, 2012.

[49] J. K.W. Yang, A. J. Kerman, E. Dauler, B. Cord, V. Anant, R. J. Molnar, and K. K. Berggren. Suppressed critical current in superconducting nanowire single-photon detectors with high fill-factors. *IEEE Transactions on Applied Superconductivity*, vol. 19, pp. 318, 2009.

[50] A.J. Kerman, E. A. Dauler, J. K.W. Yang, K. M. Rosfjord, V. Anant, K. K. Berggren, G. N. Goltsman, and B. M. Voronov. Constriction-limited detection efficiency of superconducting nanowire single-photon detectors. *Applied Physics Letters*, vol. 90, pp. 101110, 2007.

[51] R.H. Hadfield, P. A. Dalgarno, J. A. O'Connor, E. Ramsay, R. J. Warburton, E. J. Gansen, B. Baek, M. J. Stevens, R. P. Mirin, and S. W. Nam. Submicrometer photoresponse mapping of nanowire superconducting single-photon detectors. *Applied Physics Letters*, vol. 91, pp. 241108, 2007.

[52] M.S. Allman, V.B. Verma, M. Stevens, T. Gerrits, R.D. Horansky, A.E. Lita, F. Marsili, A Beyer, M.D. Shaw, D. Kumor, et al. A near-infrared 64-pixel superconducting nanowire single photon detector array with integrated multiplexed readout. *Applied Physics Letters*, 106(19):192601, 2015.

[53] R. Lusche, A. Semenov, K. Ilin, M. Siegel, Y. Korneeva, A. Trifonov, A. Korneev, G. Goltsman, D. Vodolazov, and H.-W. Hübers. Effect of the wire width on the intrinsic detection efficiency of superconducting-nanowire single-photon detectors. *Journal of Applied Physics*, vol. 116, pp. 043906, 2014.

[54] A. D. Semenov, G.N. Goltsman, and A. A. Korneev. Quantum detection by current carrying superconducting film. *Physica C: Superconductivity*, vol. 351, pp.349, 2001.

[55] A. Semenov, A. Engel, H.-W. Hübers, K. Il'in, and M. Siegel. Spectral cut-off in the efficiency of the resistive state formation caused by absorption of a single-photon in current-carrying superconducting nano-strips. *The European Physical Journal B-Condensed Matter and Complex Systems*, vol. 47, pp.495, 2005.

[56] A. D. Semenov, P. Haas, H.-W. Hübers, K. Ilin, M. Siegel, A. Kirste, T. Schurig, and A. Engel. Vortex-based single-photon response in nanostructured superconducting detectors. *Physica C: Superconductivity*, vol. 468, pp. 627, 2008.

[57] Superconducting nanotechnology SCONTEL. URL http://www.scontel.ru/.

[58] F. Marsili, D. Bitauld, A. Gaggero, S. Jahanmirinejad, R. Leoni, F. Mattioli, and
      A. Fiore. Physics and application of photon number resolving detectors based on
      superconducting parallel nanowires. *New Journal of Physics*, vol. 11, pp. 045022,
      2009.

[59] F. Marsili. *Single-photon and photon-number-resolving detectors based on supercon-
      ducting nanowires- Chapter 2*. PhD thesis, Ecole Polytechnique Federale de Lausanne,
      2009.

[60] F. Mattioli, R. Leoni, A. Gaggero, M.G. Castellano, P. Carelli, F. Marsili, and A. Fiore.
      Electrical characterization of superconducting single-photon detectors. *Journal of
      Applied Physics*, vol. 101, pp. 054302, 2007.

[61] V.B. Verma, F. Marsili, S. Harrington, A. E. Lita, R.P. Mirin, and S. W. Nam. A
      three-dimensional, polarization-insensitive superconducting nanowire avalanche pho-
      todetector. *Applied Physics Letters*, vol. 101, pp. 251114, 2012.

[62] H. Takesue, S. W. Nam, Q. Zhang, R. H. Hadfield, T. Honjo, K. Tamaki, and Y. Ya-
      mamoto. Quantum key distribution over a 40-dB channel loss using superconducting
      single-photon detectors. *Nature photonics*, vol. 1, pp. 343, 2007.

[63] D. Stucki, C. Barreiro, S. Fasel, J. Gautier, O. Gay, N. Gisin, R. Thew, Y. Thoma,
      P. Trinkler, F. Vannel, and H. Zbinden. Continuous high speed coherent one-way
      quantum key distribution. *Optics Express*, vol. 17, pp. 13326, 2009.

[64] D. Bitauld, F. Marsili, F. Gaggero, A.and Mattioli, R. Leoni, S. Jahanmiri Nejad,
      F. Lévy, and A. Fiore. Nanoscale optical detector with single-photon and multiphoton
      sensitivity. *Nano Letters*, vol. 10, pp.2977, 2010.

[65] C. Zinoni, B. Alloing, C. Monat, V. Zwiller, L.H. Li, A. Fiore, L. Lunghi, A. Gerardino,
      H. De Riedmatten, H. Zbinden, and N. Gisin. Time-resolved and antibunching experi-
      ments on single quantum dots at 1300nm. *Applied Physics Letters*, vol. 88, pp. 131102,
      2006.

[66] M.S. Allman, V. B. Verma, R. Horansky, F. Marsili, J. A. Stern, M. D. Shaw, A. D.
      Beyer, R. P. Mirin, and S. W. Nam. Progress towards a near ir single-photon supercon-
      ducting nanowire camera for free-space imaging of light. In *CLEO: Applications and
      Technology*, pages AW3P–3, 2014.

[67] A. Divochiy, F. Marsili, D. Bitauld, A. Gaggero, R. Leoni, F. Mattioli, A. Korneev,
      V. Seleznev, N. Kaurova, O. Minaeva, G. Gol'Tsman, K.G. Lagoudakis, M. Benkhaoul,
      F. Levy, and A. Fiore. Superconducting nanowire photon-number-resolving detector at
      telecommunication wavelengths. *Nature Photonics*, vol. 2, pp.302, 2008.

[68] Z. Zhou, S. Jahanmirinejad, F. Mattioli, D. Sahin, G. Frucci, A. Gaggero, R. Leoni,
      and A. Fiore. Superconducting series nanowire detector counting up to twelve photons.
      Optics express, vol. 22, pp. 3475, 2014.

[69] V.B. Verma, R. Horansky, F. Marsili, J.A. Stern, M.D. Shaw, A.E. Lita, R.P. Mirin, and S.W. Nam. A four-pixel single-photon pulse-position array fabricated from WSi superconducting nanowire single-photon detectors. *Applied Physics Letters*, vol. 104, pp. 051115, 2014.

[70] J.J. Renema, R. Gaudio, Q. Wang, Z. Zhou, A. Gaggero, F. Mattioli, R. Leoni, D. Sahin, M.J.A. de Dood, A. Fiore, and M. P. van Exter. Experimental test of theories of the detection mechanism in a nanowire superconducting single photon detector. *Physical Review Letters*, vol. 112, pp.117604, 2014.

[71] K.S. Keskar, T. Yamashita, and Y. Onodera. Superconducting transition temperatures of rf sputtered nbn films. *Japanese Journal of Applied Physics*, vol. 10, pp. 370, 1971.

[72] F. Marsili, A. Gaggero, L. H. Li, A. Surrente, R. Leoni, F. Lévy, and A. Fiore. High quality superconducting NbN thin films on GaAs. *Superconductor Science and Technology*, vol. 22, pp. 095013, 2009.

[73] D. Bitauld, F. Marsili, A. Fiore, A. Gaggero, F. Mattioli, R. Leoni, M. Benkahoul, and F. Lévy. Nbn nanowire superconducting single photon detectors fabricated on MgO substrates. *Journal of Modern Optics*, vol. 56, pp. 395, 2009.

[74] M. B. Kleiner, S. Kühn, and W. Weber. Thermal conductivity measurements of thin silicon dioxide films in integrated circuits. *IEEE Transactions on Electron Devices*, vol. 43, pp. 1602, 1996.

[75] R. O. Carlson, G. A. Slack, and S. J. Silverman. Thermal conductivity of GaAs and $GaAs_{1-x}P_x$ laser semiconductors. *Journal of Applied Physics*, vol. 36, pp. 505, 1965.

[76] C. J. Glassbrenner and G. A. Slack. Thermal conductivity of silicon and germanium from 3K to the melting point. *Phys. Rev.*, vol. 134, pp.A1058, 1964.

[77] J. Bardeen. Critical fields and currents in superconductors. *Rev. Mod. Phys.*, vol. 34, pp. 667, 1962.

[78] A. Semenov, B. Günther, U. Böttger, H.-W. Hübers, H. Bartolf, A. Engel, A. Schilling, K. Ilin, M. Siegel, R. Schneider, D. Gerthsen, and N. A. Gippius. Optical and transport properties of ultrathin NbN films and nanostructures. *Phys. Rev. B*, vol. 80, pp. 054510, 2009.

[79] J.J. Renema, Q. Wang, R. Gaudio, I. Komen, K.M.P op 't Hoog, D. Sahin, A. Schilling, M.P. van Exter, A. Fiore, A. Engel, and M.J.A. de Dood. Position-dependent local detection efficiency in a nanowire superconducting single-photon detector. *Nano Letters*, vol. 15, pp. 4541, 2015.

[80] I. Horcas, R. Fernández, J. M. Gómez-Rodríguez, J. Colchero, J. Gómez-Herrero, and A. M. Baro. WSxM: A software for scanning probe microscopy and a tool for nanotechnology. *Review of Scientific Instruments*, vol. 78, pp. 013705, 2007.

[81] H.L. Hortensius, E.F.C. Driessen, and T.M. Klapwijk. Possible indications of electronic inhomogeneities in superconducting nanowire detectors. *IEEE Transactions on Applied Superconductivity*, vol. 23, pp.2200705, 2013.

[82] M. V. Feigel'man and M. A. Skvortsov. Universal broadening of the Bardeen-Cooper-Schrieffer coherence peak of disordered superconducting films. *Phys. Rev. Lett.*, vol. 109, pp. 147002, 2012.

[83] R. Schneider, B. Freitag, D. Gerthsen, K. S. Ilin, and M. Siegel. Structural, microchemical and superconducting properties of ultrathin NbN films on silicon. *Crystal Research and Technology*, vol. 44, pp. 1115, 2009.

[84] F.J. Richards. A flexible growth function for empirical use. *Journal of experimental Botany*, vol. 10, pp. 290, 1959.

[85] J.S. Lundeen, A. Feito, H. Coldenstrodt-Ronge, K.L. Pregnell, C. Silberhorn, T.C. Ralph, J. Eisert, M.B. Plenio, and I.A. Walmsley. Tomography of quantum detectors. *Nature Physics*, vol. 5, pp. 27, 2008.

[86] J. J. Renema, G. Frucci, M. J. A. de Dood, R. Gill, A. Fiore, and M. P. van Exter. Tomography and state reconstruction with superconducting single-photon detectors. *Physical Review A*, vol. 86, pp. 062113, 2012.

[87] J. J. Renema. *The physics of nanowire superconducting single-photon detectors*. PhD thesis, Department of Quantum Matter & Optics, Leiden Institute of Physics (LION), Faculty of Science, Leiden University, 2015.

[88] J.J. Renema, G. Frucci, Z. Zhou, F. Mattioli, A. Gaggero, R. Leoni, M. J. A. de Dood, A. Fiore, and M. P. van Exter. Universal response curve for nanowire superconducting single-photon detectors. *Physical Review B*, vol. 87, pp. 174526, 2013.

[89] A. Verevkin, A. Pearlman, W. Slysz, J. Zhang, M. Currier, A. Korneev, G. Chulkova, O. Okunev, P. Kouminov, K. Smirnov, B. Voronov, G.N. Gol'Tsman, and R. Sobolewski. Ultrafast superconducting single-photon detectors for near-infrared-wavelength quantum communications. *Journal of Modern Optics*, vol. 51, pp. 1447, 2004.

[90] A. Jukna, J. Kitaygorsky, D. Pan, A. Cross, A. Perlman, I. Komissarov, O. Okunev, K. Smirnov, A. Korneev, I. Chulkova, G. and. Milostnaya, B. Voronov, G.N. Gol'tsman, and R. Sobolewski. Dynamics of hotspot formation in nanostructured superconducting stripes excited with single photons. *Acta Physica Polonica-Series A General Physics*, vol. 113, pp. 955, 2008.

[91] Z. Zhou, G. Frucci, F. Mattioli, A. Gaggero, R. Leoni, S. Jahanmirinejad, T. B. Hoang, and A. Fiore. Ultrasensitive n-photon interferometric autocorrelator. *Physical Review Letters*, vol. 110, pp.133605, 2013.

[92] R. Gaudio, K.M.P. op 't Hoog, Z. Zhou, D. Sahin, and A. Fiore. Inhomogeneous critical current in nanowire superconducting single-photon detectors. *Applied Physics Letters*, vol. 105, pp.222602, 2014.

[93] E. Knill, R. Laflamme, and G. J. Milburn. A scheme for efficient quantum computation with linear optics. *Nature*, vol. 409, pp. 46, 2001.

[94] A. G. Kozorezov, C. Lambert, F. Marsili, M. J. Stevens, V. B. Verma, J. A. Stern, R. Horansky, S. Dyer, S. Duff, D. P. Pappas, A. Lita, M. D. Shaw, R. P. Mirin, and Sae Woo Nam. Quasiparticle recombination in hotspots in superconducting current-carrying nanowires. *Phys. Rev. B*, vol. 92, pp. 064504, 2015.

Glossary of acronyms and symbols

Symbol	Description	Paragraph or Chapter
γ	Current-energy interchange	4 & 5
d_{max}	Maximum distance between two absorption sites for a two-photon detection	4.3
D_{fs}	Distance between fibre and sample	2.2.3
Δ	Superconducting energy gap	4 & 5
ΔI_c	Variation in critical current	3
$\Delta \lambda$	Distance between fringes in the OSA spectrum	2.2.3
ΔT_c	Width of superconducting-normal transition	2.2.1
E_φ	Energy of one photon	4 & 5
E_t	Total energy impinging on the detector	4 & 5
η	Linear optical efficiency	4 & 5
η_{ABS}	Absorption efficiency	1
$\eta_{coupling}$	Coupling efficiency	1
$\eta_{internal}$	Internal efficiency	1
I_b	Bias current	3, 4 & 5
I_b^{th}	Bias current needed to trigger a detection event with a given probability	4 &5
I_c	Critical current	3, 4 &5
I_{dep}	Theoretical depairing current	3
I_o	Reference current	4 &5
λ	Light wavelength	4 &5
λ_c	Central wavelength	2.2.3

Symbol	Description	Paragraph or Chapter
L	Nanowire length	2
L_k	Kinetic inductance	2
l_{taper}	Tapering length	4.3
p_i	Detection probability of i impinging photons	4 & 5
P	Absorption probability	4.3
R_{click}	Number of clicks per pulse	4 & 5
R_n	Normal resistance	1
R_s	Resistance per square	2 & 3
s	Dimension of the hot spot	4.3
T_c	Critical temperature	2
T_{dep}	Deposition temperature	2
τ_e	Time constant for the supercurrent recovery in SSPDs	1
τ_{fall}	Time constant for the supercurrent decay in SSPDs	1
w	Width of the nanowire	3, 4 & 5
ξ	Coherence length	1
χ^2	Goodness of fit	4 & 5

Acronym	Description
SSPD	Superconducting single photon detector
QDT	Quantum detector tomography
QI	Quantum information
SPD	Single photon detector
QKD	Quantum key distribution
LIDAR	Light detection and ranging
DCR or DC	Dark count rate
PCR or PC	Photon count rate
SDE	System detection efficiency
PNR	Photon number resolving
PMT	Photomultiplier tube
DE	Detection efficiency
SPAD	Single photon avalanche diode
APD	Avalanche photo diode
TES	Transition edge sensor
DDE	Device detection efficiency
AFM	Atomic force microscope
HSQ	Hydrogen Silsesquioxane
EBL	Electron beam lithography
OSA	Optical spectrum analyser

Summary

Investigation of the detection process in nanowire superconducting single photon detectors

Nanowire superconducting single-photon detectors (SSPDs) constitute a promising technology for enabling important applications of quantum communication such as quantum key distribution (QKD) and interplanetary optical communication. Since their first demonstration in 2001, several technological advances were achieved and contributed to improve the SSPDs performance. However, at the time of this thesis, numerous issues still needed to be addressed. Fore example, the origin of the inhomogeneous critical current (I_c) in NbN SSPDs as well as the nanoscale detection process in nanowire SSPDs were still open questions. In this thesis, the first question is addressed through the systematic characterization of simple detectors, short nanowire SSPDs. The implementation of quantum detector tomography (QDT) on short nanowires allowed us to address the second issue. The study of the detection mechanism was performed for NbN-based and WSi-based nanowire SSPDs and the dimension of the area perturbed by the photon absorption was investigated in NbN SSPDs.

Chapter 1 provides, in its first part, a brief overview on the existing single-photon detection technologies. The working principle and figure of merit of photomultipliers tube (PMT), photodiodes (APDs), transition edge sensors (TES) and SSPDs are presented and compared. The second part of the chapter introduces the theoretical models that, at the time of this thesis, have been proposed to describe the detection mechanism in SSPDs. The main traits of those models are highlighted and compared.

Chapter 2 deals with the experimental methods employed in this research work. This Chapter provides a description of the nanofabrication flow for the realization of the short

nanowire SSPDs and the experimental setups used for the electro-optical characterization of the devices.

Chapter 3 describes the investigation of the inhomogeneous nature of NbN nanowire SSPDs critical current and provides indication on its possible origins. The investigation is carried out on NbN short nanowires with lengths ranging from 100nm to 15μm and consists in a systematic study of their electro-optical properties. The experimental results prove that the NbN thin film is inhomogeneous and the typical inhomogeneity length scale is $\leq$100nm. Such results are consistent with a simple microscopic model that describes the short nanowire as a sequence of sections and provides the I_c distribution for each wire length.

The accurate inspection through scanning electron microscopy (SEM) allows us to exclude that patterning defects are the cause for such inhomogeneity. The polycrystalline nature of the NbN film as well as transmission electron microscopy (TEM) inspection suggests that the possible origin of I_c inhomogeneity in NbN nanowire SSPDs could be related to the variation of film thickness and/or crystal properties.

In Chapter 4, the detection mechanism and the dimension of the "hot spot" (the area of the nanowire where superconductivity is perturbed by the photon absorption) in NbN nanowire SSPDs are investigated.

The study of the detection mechanism in NbN SSPDs mainly consists in identifying the relation between the total energy of the impinging photons (E_t) and the bias current (I_b^{th}) needed to trigger a detection event with a given detection probability. The investigation was carried out with such approach because the theoretical models that describe the detection mechanism in NbN SSPDs differ for the predicted I_b^{th}-E_t relation. The functional relation I_b^{th}-E_t, which is obtained by means of quantum detector tomography, shows a linear dependence between I_b^{th} and E_t indicating that the detection mechanism is dominated by the diffusion of quasiparticles. Moreover, the investigation of the detector response as a function of temperature showed that vortices play a role in the detection mechanism of NbN nanowire SSPDs.

The estimation of the hot spot dimension is achieved by performing quantum detector tomography on four short nanowires with different lengths, identical width and very similar I_c. Our strategy is to consider the maximum distance between two absorption sites (d_{max}), for which two photons can both contribute to a detection event, as indicative of the hot spot dimension. The d_{max} is obtained by comparing the absorption probability for one absorbed photon with that for two absorbed photons that trigger a two-photon detection event. Once such procedure is applied to the four wire lengths, the estimation of d_{max} is achieved. The

experimental results show that the dimension of the hot spot in NbN nanowire SSPDs is of the order of 20nm.

Chapter 5 reports on the study of the detection mechanism in WSi nanowire SSPDs. The investigation is performed on a 250nm×250nm short nanowire by means of quantum detector tomography and aims at identifying the dominant detection process in WSi nanowire SSPDs. While the material properties such as, for example, the small superconducting gap would suggest the formation of a resistive hot spot, our experimental results show that, for the examined light wavelengths, the detection mechanism in WSi detectors is similar to that taking place in NbN SSPDs.

Finally, Chapter 6 summarizes the main results presented in this thesis and suggests future work prospects.

Acknowledgements

The scientific results of the past four years would not be achieved if I had not been surrounded by people willing to share their knowledge, happy to provide support and enthusiast for teamwork. Because of their crucial role in my PhD, I want to express all my gratitude.

My first appreciation goes to my promoter and daily supervisor, Prof. Dr. Andrea Fiore for offering me the opportunity of working on an interesting and challenging project. I am grateful for his scientific and professional guidance.

I express my gratitude for the committee members of my PhD defense: Dr. Michiel de Dood, Prof. Dr. Robert Hadfield, Dr. Rob van der Heijden, Prof. Dr. Hugo Zbinden and Prof. Dr. Ton van Leeuwen for reading this thesis and contributing with their feedbacks and comments to its improvement.

The past four years would have been more difficult without the support of FOM. I take advantage of this occasion to thank FOM and its employees for their constant availability and kindness.

When interaction and collaboration with other experts of the field is established, a PhD experience becomes more interesting and challenging. For this reason I appreciate the productive time spent at the Quantum Optics Group in Leiden University. I thank Dr. Martin van Exter and Dr. Michiel de Dood for their teachings and their guidance and Dr. Qiang Wang for the interesting and inspiring discussions we had. I am indebted to Dr. Jelmer Renema for sharing his knowledge and expertise in quantum detector tomography and for the tough time we spent inside and outside the laboratory. A substantial part of the work presented in this thesis wouldn't have been possible without such a fruitful collaboration. During the past four years I had the opportunity to interact with SSPDs experts of the Italian Council of Research (CNR) in Rome. I appreciate the support, the guidance I received from Dr. Roberto Leoni and Dr. Alessandro Gaggero, which helped me to improve my fabrication skills and the device understanding. I am grateful to Dr. Francesco Mattioli for the clarifying and interesting discussions we had and the fun time spent in the laboratory.

I am grateful to my family for their constant support and to those old friends that, despite the distance, were always close.

Finally, I want to express my gratitude toward my boyfriend Sartoon. The love, support and guidance he provided me during those challenging years were crucial for my success.

List of publications

Peer-reviewed journals

R. Gaudio, J.J. Renema, Z. Zhou, V.B. Verma, A.E. Lita, J. Shainline, M. J. Stevens, R.P. Mirin, S.W. Nam, M.J.A. de Dood, M.P. van Exter and A. Fiore, "Detection mechanism in WSi superconducting single photon detectors", *in preparation* (2015)

J.J. Renema, R. Gaudio, Q. Wang, K.P.M. op 't Hoog, Z.Zhou, D.Sahin, M.J.A. de Dood, M.P. van Exter and A. Fiore, "The hot spot interaction length in NbN nanowire superconducting single photon detectors", *in preparation* (2015)

R. Gaudio, K.M.P. op 't Hoog, Z. Zhou, D. Sahin, A. Fiore, "Inhomogeneous critical current in nanowire superconducting single-photon detectors", Applied Physics Letters **105**, 222602, (2014)

J.J. Renema, R. Gaudio, Q. Wang, Z. Zhou, A. Gaggero, F. Mattioli, R. Leoni, D. Sahin, M.J.A. de Dood, A. Fiore, M.P. van Exter, "Experimental Test of Theories of the Detection Mechanism in a Nanowire Superconducting Single Photon Detector", Physical Review Letters **112**, 117604 (2014)

Not discussed in this thesis

F. Mattioli, Z. Zhou, A. Gaggero, <u>R. Gaudio</u>, S. Jahanmirinejad, D. Sahin, F. Marsili, R. Leoni and A. Fiore, "Photon-number-resolving superconducting nanowire detectors" Supercond. Sci. Technol. **28**, 104001 (2015)

J.J. Renema, Q. Wang, <u>R. Gaudio</u>, I. Komen , K. op 't Hoog, D. Sahin, A. Schilling, M. P. van Exter, A. Fiore, A. Engel and M. J. A. de Dood, "Position-Dependent Local Detection Efficiency in a Nanowire Superconducting Single-Photon Detector", Nano Letters **15**, 4541 (2015)

J.J. Renema, R.J. Rengelink, I. Komen, Q. Wang, <u>R. Gaudio</u>, K.P.M. op't Hoog, Z. Zhou, D. Sahin, A. Fiore, P. Kes, J. Aarts, M.P. van Exter, M.J.A. de Dood, E.F.C. Driessen, Applied Physics Letters **106**, 092602 (2015)

Conference contributions

<u>R. Gaudio</u>, J.J. Renema, Q. Wang, K.P.M. op 't Hoog, Z.Zhou, D.Sahin, M.J.A. de Dood, M.P. van Exter and A. Fiore, "The hot spot length scale in NbN nanowire superconducting single photon detectors by detector tomography" at EUCAS 2015, Lyon, France (2015) (**oral contribution**)

<u>R. Gaudio</u>, J.J. Renema, Z. Zhou, Q. Wang, V.B. Verma, A.E. Lita, J. Shainline, M. J. Stevens, R.P. Mirin, S.W. Nam, M.J.A. de Dood, M.P. van Exter and A. Fiore, "Detector tomography of WSi nanowire superconducting single photon detectors" at EUCAS 2015, Lyon, France (2015) (**poster contribution**)

<u>R. Gaudio</u>, J.J. Renema, Z. Zhou, V.B. Verma, A.E. Lita, J. Shainline, M. J. Stevens, R.P. Mirin, S.W. Nam, M.J.A. de Dood, M.P. van Exter and A. Fiore, "Detection mechanism in WSi superconducting single photon detectors" at Single Photon Workshop 2015, Geneva, Switzerland (2015) (**poster contribution**)

<u>R.Gaudio</u>, J.J. Renema, Q.Wang, K.P.M. op 't Hoog, Z.Zhou, D.Sahin, M.J.A. de Dood, M.P. van Exter and A.Fiore, "Nanoscale detection processes in superconducting nanowires"

at FOM@Veldhoven, Veldhoven, The Netherlands (2015) (**oral contribution**)

R. Gaudio, K. op 't Hoog, Z. Zhou, D. Sahin and A. Fiore, "A new picture of inhomogeneities in nanowire superconducting single photon detectors" at CLEO:2014, San Jose CA, USA (2014) (**oral contribution**)

R. Gaudio, K. op 't Hoog, Z. Zhou, D. Sahin and A. Fiore, "The role of nanoscale inhomogeneities in nanowire superconducting single-photon detectors (SSPDs)" at Nanoscale Quantum Optics Lorents Workshop, Leiden, The Netherlands (2014) (**poster contribution**)

R. Gaudio, K. op 't Hoog, Z. Zhou, D. Sahin and A. Fiore, "The role of inhomogeneities in nanowire superconducting single-photon detectors" at FOM@Veldhoven, Veldhoven, The Netherlands (2014) (**poster contribution**)

R. Gaudio, K. op 't Hoog, Z. Zhou, D. Sahin and A. Fiore, "The role of inhomogeneities in nanowire superconducting single-photon detectors" at COBRA Research Institute Colloquia, Eindhoven, The Netherlands (2014) (**oral presentation**)

R. Gaudio, D. Sahin, Z. Zhou, J.J. Renema, M.J.A. de Dood, M.P. van Exter and A. Fiore, "Fabrication of Nanoscale Superconducting Single-photon Detectors" EUCAS, Genoa, Italy (2013) (**poster contribution**)

Curriculum vitae

Rosalinda Gaudio was born on the 16th of November 1986 in Telese Terme, Italy. In 2005 she obtained the high school diploma from "I. Newton" Scientific High School in Rome. She attended the University of Rome "Tor Vergata" where she studied Physics and received her Bachelor degree in 2009. In the same university, she continued her studies with the master program in Solid State Physics and in 2011 she graduated with honours. At the end of the same year she joined the group of Photonics and Semiconductor Nanophysics in Eindhoven University of Technology to work on superconducting single-photon detectors. The main scientific results achieved during her PhD studies are reported in this dissertation.

In 2005, she was awarded by *Regione Lazio* the prize for promising students undertaking scientific studies.